High modulation bandwidth optoelectronic devices with multi-Gb/s data transmission rates for visible light communications

Jack I.H. Haggar

A thesis submitted in partial fulfilment of the requirements for the degree of

Doctor of Philosophy

The University of Sheffield

Department of Electronic and Electrical Engineering

June 2022

Abstract

Large area semipolar (11$\bar{2}$2) III-nitride semiconductor based long wavelength light emitting diodes (LEDs) have been demonstrated with record breaking modulation bandwidths of 540 MHz, 350 MHz, and 140 MHz for our green (515 nm), yellow (550 nm) and amber (610 nm) LEDs, respectively. Differential carrier lifetimes of these long wavelength LEDs have been extracted from frequency response measurements, confirming that the significantly enhanced modulation bandwidth is due to the intrinsically reduced polarization of the (11$\bar{2}$2) growth orientation in comparison to currently used *c-plane* LEDs. Furthermore, the highest data transmission rates have been reported at their respective wavelengths of 4.42 Gb/s, 3.72 Gb/s, and 336 Mb/s for our green, yellow, and amber LEDs, respectively. Such high data transmission rates were achieved using adaptively bit loaded DC-optical orthogonal frequency division multiplexing (DCO-OFDM) with measured bit-error-ratios under the forward error correction (FEC) threshold standard for reliable communications.

A detailed comparison study between a similarly structured *c-plane* and semipolar LED using time-resolved electroluminescence (TREL) measurements has been performed to investigate the influence of polarisation on modulation bandwidth. The semipolar LED luminescence was found to follow closely to a tri-exponential decay, with differential carrier lifetimes $\tau_1 = 0.40$ ns and $\tau_2 = 1.2$ ns contributing towards radiative and non-radiative recombination and a third lifetime, $\tau_3 = 8.3$ ns encapsulating carrier transport effects. This was confirmed by capacitance measurements. The total carrier lifetime of a *c-plane* LED has been found to be mainly limited by RC effects due to a junction capacitance, while it is not the case for a semipolar LED due to intrinsically reduced polarization, demonstrating the major advantages of using a semipolar LED for VLC.

A monolithically integrated HEMT-microLED has been developed using our direct epitaxy approach, where an individually addressable microLED can be modulated using the gate of an individual HEMT around each microLED. Our integration has eliminated the usage of any dry-etching technique which is necessary for the fabrication of conventional microLEDs, allowing for stable, high current density operation. Consequently, the integrated HEMT-microLED achieved a record modulation bandwidth of 1.2 GHz at 13.3 kA/cm^2.

Acknowledgements

Publications

Journal publications

Haggar, J. I. H.; Cai, Y.; Ghataora, S. S.; Smith, R. M.; Bai, J.; Wang, T. "High Modulation Bandwidth of Semipolar (11–22) InGaN/GaN LEDs with Long Wavelength Emission". *ACS Appl. Electron. Mater.* **2020**, *2* (8), 2363–2368.

Cai, Y.; Haggar, J. I. H.; Zhu, C.; Feng, P.; Bai, J.; Wang, T. "Direct Epitaxial Approach to Achieve a Monolithic On-Chip Integration of a HEMT and a Single Micro-LED with a High-Modulation Bandwidth". *ACS Appl. Electron. Mater.* **2021**, *3* (1), 445–450.

Haggar, J. I. H.; Cai, Y.; Bai, J.; Ghataora, S.; Wang, T. "Long-Wavelength Semipolar (11–22) InGaN/GaN LEDs with Multi-Gb/s Data Transmission Rates for VLC". *ACS Appl. Electron. Mater.* **2021**, *3* (9), 4236–4242.

Haggar, J. I. H.; Ghataora, S.; Trinito, V.; Bai, J; Wang, T. "A study of the luminescence decay of a semipolar green LED for visible light communications by time-resolved electroluminescence". *ACS Photonics* **2022**, *9* (7), 2378–2384.

Conference contributions

Haggar, J. I. H.; Cai, Y.; Ghataora, S. S.; Smith, R. M.; Bai, J.; Wang, T. "High Modulation Bandwidth of Semipolar (11–22) InGaN/GaN LEDs with Long Wavelength Emission". *Semiconductor and Integrated OptoElectronics (SIOE) Conference,* **2021**

Haggar, J. I. H.; Cai, Y.; Bai, J.; Ghataora, S.; Wang, T. "Long-Wavelength Semipolar (11–22) InGaN/GaN LEDs with Multi-Gb/s Data Transmission Rates for VLC". *Semiconductor and Integrated OptoElectronics (SIOE) Conference,* **2022**

Table of Contents

List of figures

Chapter 1: Introduction

1.1   Motivation

Cisco, a world-leading telecommunications enterprise, predicts a 46% compound annual growth rate (CAGR) in global mobile data traffic from 2017-2022[1]. Currently, wi-fi or 5G utilise the radio frequency (RF) spectrum. Due to its limited bandwidth ($\sim$300 GHz) and the annually increasing data usage, it has been predicted that the RF spectrum is rapidly becoming saturated even though heavy bandwidth restrictions are in place. For example, the industrial, scientific and medical (ISM) sector utilises a RF band of 5.4 GHz with a bandwidth of only 500 MHz[2]. Based on Cisco's prediction, it can be expected that in 10 years the ISM RF band would use roughly 120 times the current data usage of 2022. In 20 years, this number would rise to $\sim$5300 times the current data usage assuming the CAGR is constant. It is unlikely that the CAGR will drop due to the upcoming 4G and 5G infrastructure which demand mobile cell receiver sizes on the order of 100 m and 25 m, respectively[2]. Bandwidth saturation is therefore inevitable and prompts the adoption of alternative methods for optical wireless communications (OWC). A somewhat short-term solution to the RF saturation problem for the ISM band is the use of the 'millimetre' wave region between 28 GHz and 250 GHz. For example, the unlicensed WiGig spectrum makes use of the 57-66 GHz frequency range whereas most traditional wireless networks use the 2.4 GHz and 5 GHz bands[3]. However, this method is not practical in the long term as higher frequencies suffer from increased path loss and directionality, which increases the need for line-of-sight (LoS) between devices[2].

A promising long-term solution is communication through visible light. The entire RF spectrum takes up around 1% of the visible spectrum's unlicensed 340 THz bandwidth. Since telecommunications via optical fibres with modulated lasers has been very successfully demonstrated in the infrared spectral region, namely, in the either 1300 nm or 1500 nm band[4], similar methods could be applied to the visible spectral region, i.e., the 380-740 nm range. Such research would eliminate the looming RF 'spectrum crunch' and allow high-speed communications in all types of infrastructure at relatively low cost. The driving interest behind visible light communications (VLC) research is the increasing popularity of solid-state lighting (SSL) technology. Incandescent and compact fluorescent lamp (CFL) lighting is now being replaced with higher brightness, more efficient and longer lifetime light emitting diodes (LEDs). Also, due to the 2020 ban on tungsten and halogen light sources across Europe there is a significantly increasing demand for SSL. Perhaps the most interesting characteristic of certain LEDs are their fast modulation speeds. Japanese researchers were the leaders in visible LED technology ever since the demonstration of the first GaN-based

blue LED by Nakamura et al. in 1994[5]. After which, they formed the visible light communications consortium (VLCC) with the purpose of bringing other industries and academics together to promote this new technology. Today, there are a number of standards for the commercialisation of VLC technology[6-8].

The first successful VLC link was demonstrated by Pang et al. [9] in 1999 by using traffic lights to broadcast audio information. In general, VLC is realised through intensity modulation of light, meaning that it requires illumination for successful data communication. However, several Mb/s of data transfer has been demonstrated when a LED is perceived as off (Lights-off VLC)[10]. Infrared (IR) LEDs can also be used as a substitution if illumination is not designed for the application[9]. When any communication link is established for private or commercial use, security and health regulations need to be addressed. Due to the nature of VLC, electro-magnetic interference (EMI) effects can be neglected while this is not the case for standard RF signals. From this stems interesting security and health benefits for specific applications such as hospitals, aeroplane cabins, nuclear power stations, mines, and underwater communication applications[10]. From a consumer's perspective, VLC is expected to be a key technology in the implementation of the Internet of Things (IoT) whereby all personal day-to-day devices are sharing information. A consumer's implementation of the IoT provides a future 'smart-home' where home appliances such as kitchen equipment, thermostats, security cameras and lighting fixtures are all interconnected and manageable on one device. Most of these devices already have LEDs displaying useful information to the user. This lighting infrastructure along with the potential high data transmission rates makes VLC a cost effective and viable alternative to RF communications.

1.2 History of III-Nitride LEDs

Electroluminescence i.e., light emission from a solid-state material using a voltage source was first discovered in 1907 by H. J. Round when testing SiC crystals commonly used in radio receivers[11]. Later, in 1928 O. V. Lossev published the results of electroluminescence from a SiC semiconductor rectifier under reverse bias with corresponding current-voltage characteristics, indicating the regions of electroluminescence[12]. Eventually, Lossev deduced that electroluminescence is generated by an 'active layer' in the material and by 1940 managed to correlate the emission energy to the absorption edge (i.e., bandgap energy) of SiC.

The first LED operating in the visible spectrum was successfully demonstrated in 1962 by N. Holonyak and S. F. Bevacqua with red emission (710 nm) based on the GaAsP material system[13]. Substantial efforts were made to further extend the emission wavelength to the shorter end of the spectrum by increasing the phosphor (P) content. However, the LED

radiative efficiency significantly decreased when the P content reached 44% due to the direct to indirect bandgap transition of GaAsP[14,15]. Therefore, alternative approaches were needed in order to generate viable solutions for short wavelength visible LEDs.

In 1968, H. P. Muruska had gained a lot of experience in growing GaAsP red LEDs using metal-halide vapor-phase epitaxy (MHVPE) and was tasked by his supervisor J. Tietjen to attempt to grow single crystalline films of GaN to eventually create a blue LED that Tietjen could use in his RGB flat panel display. Shortly after in 1969, Maruska managed to grow a single GaN film after realising that growth occurs in an ammonia environment at elevated temperatures. The films were found to be intrinsically n-type with a direct bandgap of 3.39 eV[16]. J. I Pankove later created a metal-insulator-semiconductor (MIS) diode consisting of an n-type region, an insulating Zn-doped layer and an indium surface layer, thus demonstrating the first electrically injected GaN light emitter[17]. Maruska postulated that Mg would be a better dopant than Zn and reported later in 1974 on another MIS device exhibiting blue emission[18]. The Mg doping however proved not to be p-type conductive and deemed to be very inefficient, resulting in Maruska retiring from further research in the MIS/LED area.

There were very few publications on GaN after Maruska's contribution and was not until the late 1980s and early 1990s where a team of Japanese researchers invented a two-step growth method, namely, firstly depositing a thin AlN nucleation layer on a sapphire substrate at a low temperature before a GaN layer grown at a high temperature, enabling crack-free, high quality GaN films, where the thin AlN nucleation plays an important role in accommodating the lattice mismatch between sapphire and GaN[19,20]. GaN with p-type conductivity using Mg dopants was achieved unintentionally by low-energy electron-beam irradiation (LEEBI) which decomposes neutral Mg-H complexes formed during Mg-doped GaN growth, allowing for p-type conductivity. This permitted for strong violet-blue electroluminescence, demonstrating the first GaN PN homojunction LED in 1989 with 1% efficiency[21]. In 1994, S. Nakamura and colleagues demonstrated the first blue GaInN based double-heterostructure LEDs with an InGaN/AlGaN quantum well structure with efficiencies up to 10%[5,22,23]. The breakthrough in efficiencies were attributed to the thermal activation of Mg dopants, achieved alternatively by annealing the p-type film under nitrogen ambient. As a result of the significant breakthroughs in GaN LEDs, the 2014 Nobel prize was awarded to I. Asaki, H. Amano and S. Nakamura.

1.3   Challenges

Green LEDs and blue LEDs which are based on III-nitride semiconductors are commercially available, while the technologies for the growth and the fabrication of red LEDs are based on the mature AlInGaP system. Together, they can form RGB LEDs. Currently, there exists

several fundamental challenges that are yet to be overcome with the AlInGaN system which hinders the progress of VLC. The majority of which are agreed by most to stem from the large lattice-mismatch between sapphire and GaN, as well as the lattice mismatch between the InGaN/GaN quantum well layers in heterostructure LEDs. As will be explained further below, the Quantum Confined Stark Effect (QCSE) resulting from the mismatch acts as a challenging roadblock in achieving efficient LEDs at longer emission wavelengths.

1.3.1 Substrate

Due to the lack of affordable GaN substrates, III-nitride growth is limited to lattice-mismatched heteroepitaxy using foreign substrates, typically sapphire (Al_2O_3), silicon carbide (6H-SiC) and silicon (Si). The considerably large difference in both lattice mismatch and thermal expansion coefficients between the foreign substrates and III-nitrides serves to induce a high density of defects. These defects generally introduce non-radiative recombination centres, which is detrimental to the quantum efficiency. For example, the lattice mismatch between GaN and the foreign substrate is 16%, 3.4% and 17% for sapphire, silicon carbide and silicon, respectively. Free-standing GaN substrates can be formed via hydride vapor phase epitaxy (HVPE) by first growing a very thick GaN layer with a thickness of typically more than 300 μm onto a foreign substrate such as sapphire and then utilising a laser-lift off technique to remove the substrate[24–26]. However, this is not a cost-effective procedure and there are other issues such as cracking and bowing which occurs during the lift-off process.

Clearly, the substrate of choice should be SiC, since it experiences the smallest lattice mismatch difference. However, SiC substrates are extremely expensive (around $1000 per 2-inch wafer) which is not practical when scaling for mass production. Si substrates, whilst being the cheapest of the three, have serious issues when considering for III-Nitride growth due to the largest lattice mismatch difference and the large thermal expansion coefficient difference induced tensile strain. The latter easily leads to severe cracking issues. As a compromise, sapphire is the usual substrate of choice for III-Nitride heteroepitaxy as it is transparent to visible light, inexpensive and very chemically and structurally stable. All samples in this thesis are grown on sapphire substrates.

1.3.2 Quantum Confined Stark Effect

In the absence of an external electric field, electrons and holes in a quantum well (QW) may only occupy states within a discrete set of energy sub-bands for the valence band and conduction band, respectively. With an applied electric field, however, the electron states shift to lower energies and hole states shift to higher energies resulting in a reduction in permitted light absorption and emission energies, causing a redshift in emission. In addition,

the electric field potential causes the electrons and holes to move to the opposite sides of the QW, leading to a reduction in the electron and hole wavefunction overlap integrals and ultimately reducing the recombination rate and quantum efficiency. This is known as the quantum confined stark effect (QCSE) which can be schematically illustrated under an unbiased and a biased case in Figure 1-1.
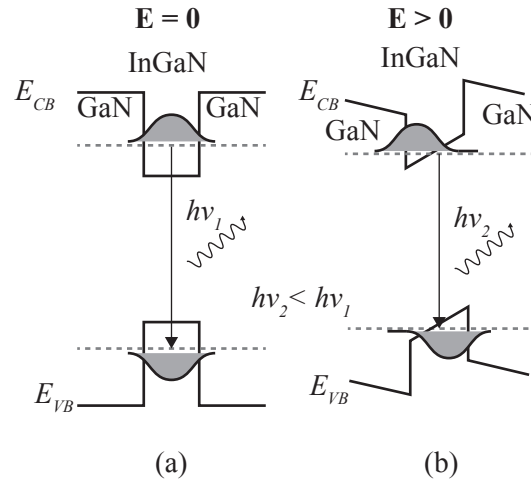
Figure 1-1 InGaN/GaN quantum well structure demonstrating the quantum confined Stark effect for unbiased (a) and biased (b) cases.

This effect is synonymous with the heterostructure of LED active regions. Since there exists a lattice mismatch between quantum well structures, for example, InGaN/GaN quantum wells and barriers, a strain is introduced once the heterostructure is formed. The induced strain generates piezoelectric fields across the InGaN quantum wells and forms the QCSE mentioned above resulting in long-reaching consequences on device electrical and optical performance. Longer wavelength emitters such as green, yellow, or red can be achieved by increasing the indium content which once again increases the lattice mismatch between the InGaN/GaN structure resulting in an enhanced QCSE, further reducing device efficiency. Increasing the carrier density in the active region flattens the bandstructure (depending on the field direction) since the injected carriers partially screen out the piezoelectric fields, resulting in a blue shift in emission wavelength[27,28]. Small active area devices such as microLEDs capable of very high current densities can screen out the polarisation fields significantly, but at the heavy sacrifice of optical performance due to significant efficiency droop at elevated carrier densities, which will be discussed later.

The even greater concern for VLC applications is how the QCSE decreases the modulation bandwidth due to its influence on the total carrier lifetime. In addition to the piezoelectric polarisation generated by the lattice mismatch in an active region, another spontaneous polarisation arises due to the intrinsic nature of wurtzite III-nitride materials on widely used

c-plane substrates. Since the modulation bandwidth of an LED is inversely proportional to its carrier recombination lifetime by $f \propto 1/\tau$ (when not limited by its geometrical capacitance), the piezoelectric and the spontaneous polarisations across InGaN/GaN quantum wells on *c-plane* substrates limits the modulation bandwidth to a few 10s of MHz[29,30].

QCSE is considered to be one of the main contributing factors to the 'Green Gap' phenomenon of III-nitrides, which will be discussed in more detail below.

1.3.3   The Green Gap

Figure 1-2 shows the bandgap energies and corresponding lattice constants for the AlInGaN material system. By tuning the indium or aluminium fraction in InGaN and AlInN systems respectively, the deep UV to the near infrared (NIR) region can be achieved. Changing the relative compositions nearer to the green/yellow spectral regions however impacts the efficiency of the device significantly, mainly due to the QCSE described above. Other approaches are to use the III-phosphide (III-P) system by tuning the Al composition as shown in the inset of Figure 1-2. Unfortunately, emission wavelengths are restricted between 560-650 nm as the direct-indirect bandgap transition occurs with Al compositions > 53% after which the efficiency reduces significantly. This phenomenon is known as the 'Green Gap' since it is very difficult to achieve similar efficiencies in the green and yellow regions as the blue and red regions for the III-N and III-P structures respectively.
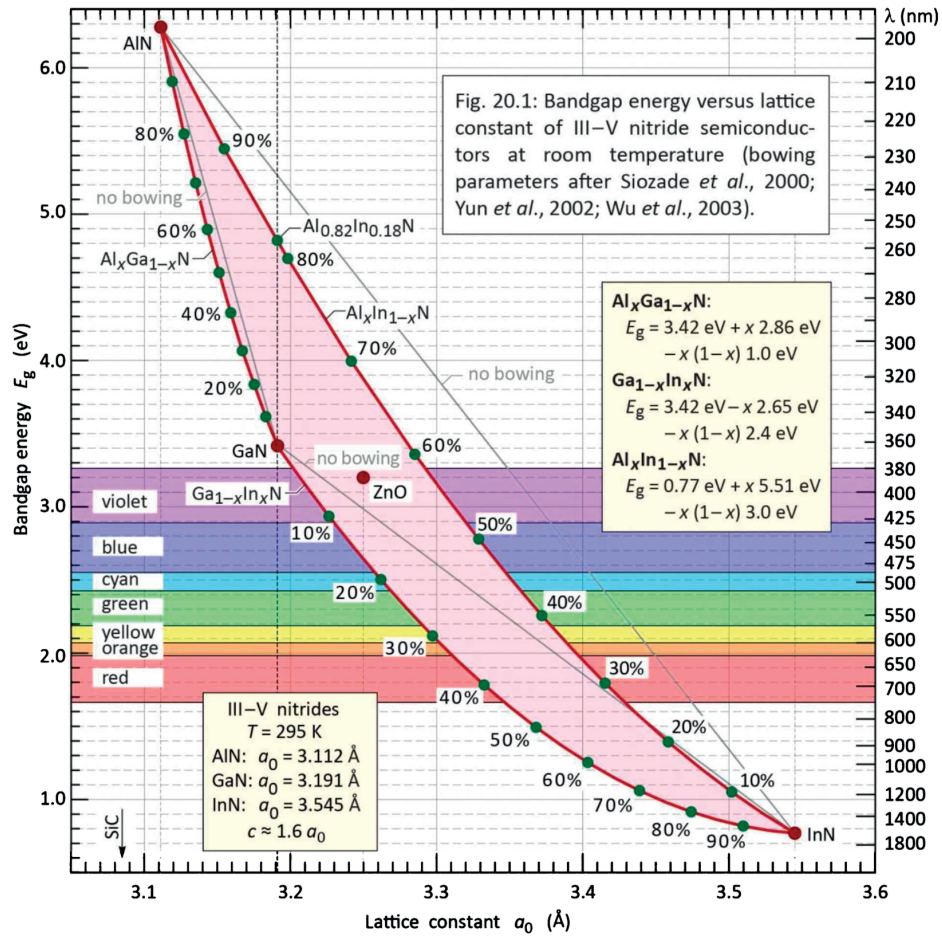
Figure 1-2 Bandgap energy as a function of lattice constant for the AlInGaN material system[31]. Reproduced with permission.

To bypass this issue, white light emission is usually obtained by partially down-converting emission of a blue InGaN/GaN LED to the green/yellow region via a layer of phosphor. The phosphor layer absorbs a photon from the blue LED and enters an excited state, then emits a down-converted photon via vibration energy relaxation. The resulting energy loss in the conversion process is typically around 25%, implying the efficiency of a white LED using this method is relatively low[33]. For VLC applications, the phosphor conversion process is very slow, with a response time on the scale of microseconds resulting in a LED modulation bandwidth of 1 MHz[34–36], which is clearly not practical for data transmission.

1.3.4   Efficiency Droop

The external quantum efficiency of an LED is defined as

$$EQE = \frac{P_{LED}/h\nu}{I/e},$$ (1-1)

where P_{LED} is the measured LED optical power, $h\nu$ is the photon energy, I is the injection current and e is the charge of an electron. Qualitatively, the numerator gives the number of

photons emitted into free space per second by the LED and the denominator represents the number of electrons injected into the LED per second.

In general, LED efficiency tends to decrease gradually with injection current. This phenomenon faced with III-nitride devices is the so called 'efficiency droop'. The origins of this effect are still up for debate within the community, but it is mostly agreed that the effect originates from various non-radiative channels such as Auger recombination, Shockley-Read- Hall (SRH) recombination and current leakage[37]. Figure 1-3 shows EQE as a function of injection current, showing an initial increase in EQE with increasing injection current and then a decrease in EQE with further increasing injection current, typically between 100-1000 A/cm^2 for GaN-based LEDs[38].
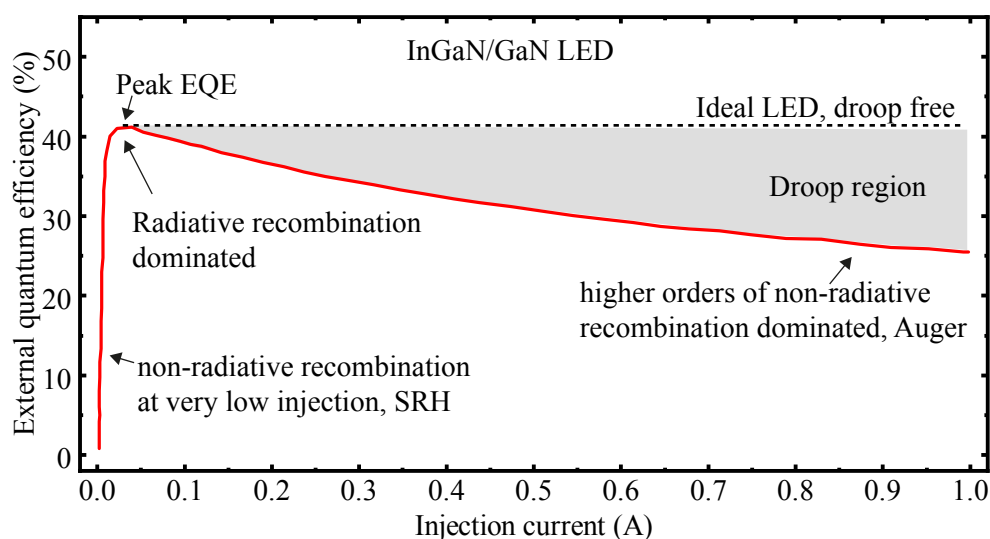
Figure 1-3 Efficiency droop in InGaN/GaN LEDs when increasing the current density in the active region.

Auger recombination occurs after an electron-hole recombination, the resulting photon is absorbed by another electron or hole and is excited to a higher energy state. The excited carrier then loses its energy via the form of a phonon i.e., a vibration which dissipates through the lattice. Since this is a three-particle interaction, the effect is more likely at high current densities where the system is in non-equilibrium conditions. SRH recombination is another non-radiative effect where trap energy levels occur within the bandgap of materials due to dopants or unwanted impurities. When a carrier is in transition between bands, these states trap the carrier and energy is exchanged through a phonon. Current leakage is a carrier transport process whereby injected carriers escape through the active region without undergoing recombination processes, called hot-carriers. An electron-blocking layer (EBL) can be grown between the p-GaN and the active region in order to minimise the generation of hot-carriers, enhancing recombination efficiency[39].

1.4   Realising long wavelength VLC

To optimise devices for VLC applications the fundamental challenges with III-nitrides described above need to be considered. As will be explained in more detail in Chapter 2, the modulation bandwidth of a LED is limited by its total recombination lifetime and is essential for data transmission. Therefore, if the QCSE reduces the recombination efficiency by reducing the wavefunction overlap integrals then to realise large LED modulation bandwidths without sacrificing EQE, the QCSE needs to be minimised. There are two main approaches to increasing the modulation bandwidth of LEDs by mitigating the QCSE, this section will outline these methods.

1.4.1   MicroLEDs

The first and one of the most attractive methods is to reduce the active area of the LED to < 100 μm in diameter, which is the generally accepted size to be named microLED. Due to their small area, desirable heat dissipation, and high crystal quality available from commercial wafers, microLEDs can be driven on the order of kA/cm^2. At such high current densities, the carrier recombination rate can be significantly enhanced (mainly due to the non-radiative recombination), potentially leading to a substantial increase in modulation bandwidth at the expense of sacrificing internal quantum efficiency.

The first report of a GaN microLED suited for VLC was demonstrated by McKendry et al. in 2010, where the electrical-to-optical (-6 dB attenuation point as opposed to the conventional electrical -3 dB point) modulation bandwidth of a 450 nm blue LED with 72 μm pixel diameter reached 245 MHz using off-the-shelf commercial GaN wafers[41]. As a follow up to this work, McKendry fabricated an individually addressable 8 × 8 array with varying pixel sizes from 14 μm to 84 μm[42]. Initially, the smaller LED pixels seemed to demonstrate a higher modulation bandwidth compared with the larger area devices (> 400 MHz). However, it was later found that the modulation bandwidth was independent of device size when evaluating the injected current density into each device, even though the smaller pixels were able to reach higher bandwidths. For broad area LEDs, the modulation bandwidth is usually limited by the RC time constant since junction capacitance scales with device area. These results suggested that microLEDs are not limited by their geometrical capacitance and are instead governed by another mechanism. The best explanation for this is through the differential carrier lifetime of carriers in the quantum wells. The relationship between the differential carrier lifetime, $\tau_{diff,}$ and injected carrier density, n, can be described by the ABC model[40]

$$\tau_{diff}(n) = \frac{1}{A + 2Bn + 3Cn^2},\tag{1-2}$$

where A, B and C are the Shockley-Reed-Hall, radiative and Auger coefficients, respectively. Increasing the carrier density decreases the differential carrier lifetime, and even more so at higher injection levels where Auger non-radiative recombination dominates. This may explain why smaller pixels are in general able to withstand higher carrier densities and demonstrate larger modulation bandwidths, due to their better heat dissipation when dealing with higher orders of non-radiative recombination.

Recent reports have seen *c-plane* GaN based microLEDs reach modulation bandwidths approaching 1 GHz[43] under high injection current regimes. It is worth highlighting that since the increase in modulation bandwidth is dominated by non-radiative recombination, the microLEDs experience very low EQE as a result. MicroLEDs have also been used in many VLC systems with excellent data transmission rates beyond 10 Gb/s by arranging several microLEDs together and driving them simultaneously, which increases the total signal-to-noise ratio (SNR) of the system and enables higher data transmission rates[44-57]. Since microLEDs utilise similar growth structures and orientations to commercial LEDs i.e., *c-plane* InGaN/GaN on sapphire, the problems associated with higher indium content structures are still present. This is why microLED VLC research is generally limited to <500 nm emitters, since the optical performance above this wavelength is extremely poor, and the benefits of the high current density capabilities are no longer applicable due to the absence of high-quality commercial wafers at longer wavelengths. This is shown in Figure 1-4b.

1.4.2   Semipolar and nonpolar LEDs

As will be discussed in more detail in Chapter 2, one of the most effective routes to achieving high modulation bandwidths at long wavelengths for VLC applications is through semipolar and nonpolar LEDs. By growing along a semipolar or nonpolar orientation, the QCSE can be significantly reduced or effectively eliminated. Due to the lack or the reduction of polarisation in these growth directions, a short carrier recombination lifetime and thus an increased optical efficiency is expected[58]. In addition, some semipolar planes are particularly favourable such as the $(11\bar{2}2)$ orientation offering increased indium incorporation efficiency. As a result, enhanced indium compositions can be achieved at elevated growth temperatures in comparison to those on *c-plane* substrates, which is helpful for improving crystal quality. As explained above, large modulation bandwidths are achieved by driving *c-plane* LEDs at very high current densities which reduces the total recombination lifetime. Semipolar and nonpolar LEDs reduce the total recombination lifetime due to the large electron-hole wavefunction overlap. As a result, significantly higher modulation bandwidths are attainable

at much lower current densities than *c-plane* LEDs, which is very desirable when considering both power consumption and efficiency. The influence of the orientation of a LED (i.e., nonpolar, semipolar and polar) on bandwidth is given in Figure 1-4 which highlights the key advantages of alternative growth planes in wurtzite GaN for VLC applications.
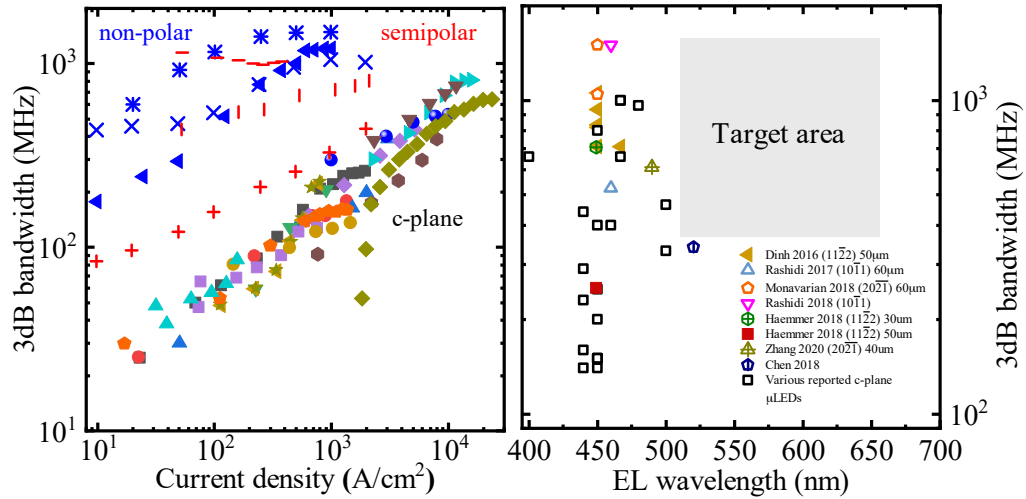
Figure 1-4 (a) Modulation bandwidth of GaN LEDs as a function of injection current density, highlighting different growth orientations (b) corresponding wavelengths. The grey box indicates the motivation for the work in this thesis[45-65].

In addition to the VLC capabilities, nonpolar and semipolar LEDs have more design flexibility in their active region structure due to the absence of QCSE. The efficiency droop mentioned above can be minimised by employing thick QW active regions, which reduces the carrier density for a given current density. Since the carrier density in the active region is reduced, the Auger recombination rate is reduced, leading to an improvement in device effciency[66,67]. In *c-plane* LEDs this is not the case due to the reduced wavefunction overlap from the polarisation induced QCSE, limiting devices to a thin QW active region structure. Semipolar and nonpolar LEDs also experience better wavelength stability as a function of injection current, an important design consideration in display applications[68,69].

1.5   Project description

The work in this thesis aims to demonstrate the need for semipolar LEDs for efficient long wavelength emitters and monolithically integrated high bandwidth microLEDs that exploit the mitigated QCSE to enable Gb/s data transmission rates for VLC applications. The thesis is split into 8 chapters:

Chapter 1 presents an introduction to VLC, a necessary technology for the advancement of OWC in the near future using III-nitride emitters as the vehicles for data transmission. The current challenges in achieving longer wavelength devices are presented, along with the

challenges faced with commercial GaN wafers with respect to modulation bandwidth capabilities.

Chapter 2 delves deeper into the background of the fundamental device physics of LEDs, highlighting the characteristics of interest for VLC. Semipolar and nonpolar LEDs are introduced in detail, and their benefits over *c-plane* GaN discussed. Our approach to developing high-quality crystal semipolar ($11\bar{2}2$) is given, which is the groundwork for enabling the VLC applications demonstrated later in the thesis.

Chapter 3 describes the experimental methods used in the thesis, starting with our custom VLC system. A detailed explanation is presented on the techniques used to measure the frequency response of the devices, along with the important modulation schemes which enable such high data transmission rates. Our time-resolved electro/photoluminescence setups are also presented to study the recombination dynamics in semipolar LEDs along with standard setups for typical LED characteristics.

Chapter 4 demonstrates the record for the modulation bandwidths of semipolar ($11\bar{2}2$) LEDs operating > 500 nm and a detailed comparison to other works is presented, clearly highlighting the benefits of our novel overgrowth approach.

Chapter 5 builds on this work and presents record data transmission rates at each of the LEDs respective wavelengths using DC-biased optical orthogonal frequency division multiplexing (DCO-OFDM). A detailed description on how these data rates were achieved is given.

Chapter 6 presents our time-resolved electroluminescence system, which determines three distinct lifetimes associated with a ($11\bar{2}2$) semipolar LED electroluminescence decay profile, the slowest of which attributed to carrier transport effects, as confirmed by LCR measurements. This system shows what conventional time-resolved photoluminescence cannot in LED structures, since excitation is supplied by an electrical source injected via the contacts where various transport processes occur rather than optically pumping the active region directly.

Chapter 7 presents a novel approach to monolithically integrating a high-electron mobility transistor (HEMT) with a microLED to demonstrate the highest modulation bandwidth at the time of publishing for *c-plane* LEDs. The HEMT acts to provide more device stability at elevated current densities, enabling high frequency performance.

Chapter 8 presents a summary, conclusion, and further work for the future of VLC using semipolar LEDs and microLEDs.

1.6   References

(1)   Index, C. V. N. Global Mobile Data Traffic Forecast Update, 2017–2022. *Cisco white Pap.* **2019**.

(2)   Haas, H. LiFi Is a Paradigm-Shifting 5G Technology. *Rev. Phys.* **2018**, *3*, 26–31. https://doi.org/10.1016/J.REVIP.2017.10.001.

(3)   Hansen, C. J. WiGiG: Multi-Gigabit Wireless Communications in the 60 GHz Band. *IEEE Wirel. Commun.* **2011**, *18* (6), 6–7.

(4)   Dochhan, A.; Eiselt, N.; Hohenleitner, R.; Griesser, H.; Eiselt, M.; Ortsiefer, M.; Neumeyr, C.; Olmos, J. J. V.; Monroy, I. T.; Elbers, J.-P. 56 Gb/s DMT Transmission with VCSELs in 1.5 Um Wavelength Range over up to 12 Km for DWDM Intra-Data Center Connects. In *ECOC 2016; 42nd European Conference on Optical Communication*; VDE, 2016; pp 1–3.

(5)   Nakamura, S.; Mukai, T.; Senoh, M. Candela-class High-brightness InGaN/AlGaN Double-heterostructure Blue-light-emitting Diodes. *Appl. Phys. Lett.* **1994**, *64* (13), 1687–1689.

(6)   *Information Technology--Telecommunications and Information Exchange Between Systems Local and Metropolitan Area Networks--Specific Requirements - Part 11: Wireless LAN Medium Access Control (MAC) and Physical Layer (PHY) Specifications Amendment 7: Light Communications,* IEEE Standard P802.11bb, **2022**

(7)   *Multi-Gigabit per Second Optical Wireless Communications (OWC), with Ranges up to 200 meters, for both stationary and mobile devices,* IEEE Standard P802.15.13, **2020**

(8)   *High-speed indoor visible light communication transceiver – System architecture, physical layer and data link layer specification,* ITU-T Standard G.9991, **2019**

(9)   Pang, G.; Kwan, T.; Chi-Ho Chan; Hugh Liu. LED Traffic Light as a Communications Device. In *Proceedings 199 IEEE/IEEJ/JSAI International Conference on Intelligent Transportation Systems (Cat. No.99TH8383)*; IEEE; pp 788–793. https://doi.org/10.1109/ITSC.1999.821161.

(10)   Borogovac, T.; Rahaim, M. B.; Tuganbayeva, M.; Little, T. D. C. "Lights-off" Visible Light Communications. In *2011 IEEE GLOBECOM Workshops (GC Wkshps)*; IEEE, 2011; pp 797–801.

(11)   Wang, C.-X.; Haider, F.; Gao, X.; You, X.-H.; Yang, Y.; Yuan, D.; Aggoune, H. M.; Haas, H.; Fletcher, S.; Hepsaydir, E. Cellular Architecture and Key Technologies for 5G Wireless Communication Networks. *IEEE Commun. Mag.* **2014**, *52* (2), 122–130.

(12)   Ghassemlooy, Z.; Popoola, W.; Rajbhandari, S. *Optical Wireless Communications: System and Channel Modelling with Matlab®*; CRC press, 2019.

(13)   Round, H. J. A Note on Carborundum. In *Semiconductor Devices: Pioneering Papers*; World Scientific, 1991; p 879.

(14)   Lossev, O. V. CII. Luminous Carborundum Detector and Detection Effect and Oscillations with Crystals. *London, Edinburgh, Dublin Philos. Mag. J. Sci.* **1928**, *6*

(39), 1024–1044.

(15)   Holonyak Jr, N.; Bevacqua, S. F. Coherent (Visible) Light Emission from Ga (As1−
         x P x) Junctions. *Appl. Phys. Lett.* **1962**, *1* (4), 82–83.

(16)   Holonyak Jr, N.; Bevacqua, S. F.; Bielan, C. V; Lubowski, S. J. THE``DIRECT-
         INDIRECT''TRANSITION IN Ga (As1− x P x) P-n JUNCTIONS. *Appl. Phys.
         Lett.* **1963**, *3* (3), 47–49.

(17)   Pilkuhn, M.; Rupprecht, H. Electroluminescence and Lasing Action in GaAs x P1−
         X. *J. Appl. Phys.* **1965**, *36* (3), 684–688.

(18)   Maruska, H. P.; Tietjen, J. J. The Preparation and Properties of Vapor-deposited
         Single-crystal-line GaN. *Appl. Phys. Lett.* **1969**, *15* (10), 327–329.

(19)   Pankove, J. I.; Miller, E. A.; Berkeyheiser, J. E. GaN Electroluminescent Diodes. In
         1971 International Electron Devices Meeting; IEEE, 1971; p 78.

(20)   Maruska, H. P.; Stevenson, D. A. Mechanism of Light Production in Metal-
         Insulator-Semiconductor Diodes; GaN: Mg Violet Light-Emitting Diodes. *Solid.
         State. Electron.* **1974**, *17* (11), 1171–1179.

(21)   Amano, H.; Sawaki, N.; Akasaki, I.; Toyoda, Y. Metalorganic Vapor Phase
         Epitaxial Growth of a High Quality GaN Film Using an AlN Buffer Layer. *Appl.
         Phys. Lett.* **1986**, *48* (5), 353–355.

(22)   Nakamura, S. N. S. GaN Growth Using GaN Buffer Layer. *Jpn. J. Appl. Phys.* **1991**,
         30 (10A), L1705.

(23)   Amano, H.; Kito, M.; Hiramatsu, K.; Akasaki, I. P-Type Conduction in Mg-Doped
         GaN Treated with Low-Energy Electron Beam Irradiation (LEEBI). *Jpn. J. Appl.
         Phys.* **1989**, *28* (12A), L2112.

(24)   Nakamura, S.; Senoh, M.; Mukai, T. High-power InGaN/GaN Double-
         heterostructure Violet Light Emitting Diodes. *Appl. Phys. Lett.* **1993**, *62* (19), 2390–
         2392.

(25)   Nakamura, S.; Senoh, M.; Iwasa, N.; Nagahama, S. N. S. High-Brightness InGaN
         Blue, Green and Yellow Light-Emitting Diodes with Quantum Well Structures. *Jpn.
         J. Appl. Phys.* **1995**, *34* (7A), L797.

(26)   Park, S. S.; Park, I.-W.; Choh, S. H. Free-Standing GaN Substrates by Hydride
         Vapor Phase Epitaxy. *Jpn. J. Appl. Phys.* **2000**, *39* (11B), L1141.

(27)   Motoki, K. M. K.; Okahisa, T. O. T.; Matsumoto, N. M. N.; Matsushima, M. M. M.;
         Kimura, H. K. H.; Kasai, H. K. H.; Takemoto, K. T. K.; Uematsu, K. U. K.; Hirano,
         T. H. T.; Nakayama, M. N. M. Preparation of Large Freestanding GaN Substrates
         by Hydride Vapor Phase Epitaxy Using GaAs as a Starting Substrate. *Jpn. J. Appl.
         Phys.* **2001**, *40* (2B), L140.

(28)   Yoshida, T.; Oshima, Y.; Eri, T.; Ikeda, K.; Yamamoto, S.; Watanabe, K.; Shibata,
         M.; Mishima, T. Fabrication of 3-in GaN Substrates by Hydride Vapor Phase
         Epitaxy Using Void-Assisted Separation Method. *J. Cryst. Growth* **2008**, *310* (1),
         5–7.

(29)   Waltereit, P.; Brandt, O.; Trampert, A.; Grahn, H. T.; Menniger, J.; Ramsteiner, M.;
         Reiche, M.; Ploog, K. H. Nitride Semiconductors Free of Electrostatic Fields for
         Efficient White Light-Emitting Diodes. *Nature* **2000**, *406* (6798), 865–868.

(30)   Takeuchi, T.; Wetzel, C.; Yamaguchi, S.; Sakai, H.; Amano, H.; Akasaki, I.;
        Kaneko, Y.; Nakagawa, S.; Yamaoka, Y.; Yamada, N. Determination of
        Piezoelectric Fields in Strained GaInN Quantum Wells Using the Quantum-
        Confined Stark Effect. *Appl. Phys. Lett.* **1998**, *73* (12), 1691–1693.

(31)   Gopal, P.; Spaldin, N. A. Polarization, Piezoelectric Constants, and Elastic
        Constants of ZnO, MgO, and CdO. *J. Electron. Mater.* **2006**, *35* (4), 538–542.

(32)   Takeuchi, T.; Amano, H.; Akasaki, I. Theoretical Study of Orientation Dependence
        of Piezoelectric Effects in Wurtzite Strained GaInN/GaN Heterostructures and
        Quantum Wells. *Jpn. J. Appl. Phys.* **2000**, *39* (Part 1, No. 2A), 413–416.
        https://doi.org/10.1143/jjap.39.413.

(33)   Schubert, E. F. *Light-Emitting Diodes*; E. Fred Schubert, 2018.

(34)   Caro Bayo, M. Á. Theory of Elasticity and Electric Polarization Effects in the
        Group-III Nitrides. University College Cork 2013.

(35)   Tsao, J. Y.; Crawford, M. H.; Coltrin, M. E.; Fischer, A. J.; Koleske, D. D.;
        Subramania, G. S.; Wang, G. T.; Wierer, J. J.; Karlicek, R. F. Toward Smart and
        Ultra-Efficient Solid-State Lighting. *Adv. Opt. Mater.* **2014**, *2* (9), 809–836.
        https://doi.org/10.1002/adom.201400131.

(36)   Wang, S. W.; Chen, F.; Liang, L.; He, S.; Wang, Y.; Chen, X.; Lu, W. A High-
        Performance Blue Filter for a White-Led-Based Visible Light Communication
        System. *IEEE Wirel. Commun.* **2015**, *22* (2), 61–67.
        https://doi.org/10.1109/MWC.2015.7096286.

(37)   Chow, C. W.; Yeh, C. H.; Liu, Y. F.; Huang, P. Y.; Liu, Y. Adaptive Scheme for
        Maintaining the Performance of the In-Home White-LED Visible Light Wireless
        Communications Using OFDM. *Opt. Commun.* **2013**, *292*, 49–52.
        https://doi.org/10.1016/j.optcom.2012.11.081.

(38)   Le Minh, H.; O'Brien, D.; Faulkner, G.; Zeng, L.; Lee, K.; Jung, D.; Oh, Y.; Won,
        E. T. 100-Mb/s NRZ Visible Light Communications Using a Postequalized White
        LED. *IEEE Photonics Technol. Lett.* **2009**, *21* (15), 1063–1065.

(39)   Cho, J.; Schubert, E. F.; Kim, J. K. Efficiency Droop in Light-emitting Diodes:
        Challenges and Countermeasures. *Laser Photon. Rev.* **2013**, *7* (3), 408–421.

(40)   David, A.; Grundmann, M. J. Droop in InGaN Light-Emitting Diodes: A
        Differential Carrier Lifetime Analysis. *Appl. Phys. Lett.* **2010**, *96* (10), 103504.

(41)   McKendry, J. J. D.; Green, R. P.; Kelly, A. E.; Gong, Z.; Guilhabert, B.; Massoubre,
        D.; Gu, E.; Dawson, M. D. High-Speed Visible Light Communications Using
        Individual Pixels in a Micro Light-Emitting Diode Array. *IEEE Photonics Technol.
        Lett.* **2010**, *22* (18), 1346–1348.

(42)   McKendry, J. J. D.; Massoubre, D.; Zhang, S.; Rae, B. R.; Green, R. P.; Gu, E.;
        Henderson, R. K.; Kelly, A. E.; Dawson, M. D. Visible-Light Communications
        Using a CMOS-Controlled Micro-Light-Emitting-Diode Array. *J. Light. Technol.*
        2011, *30* (1), 61–67.

(43)   Wang, L.; Wei, Z.; Chen, C.-J.; Wang, L.; Fu, H. Y.; Zhang, L.; Chen, K.-C.; Wu,
        M.-C.; Dong, Y.; Hao, Z. 1.3 GHz EO Bandwidth GaN-Based Micro-LED for
        Multi-Gigabit Visible Light Communication. *Photonics Res.* **2021**, *9* (5), 792–802.

(44)   Zhang, S.; Watson, S.; McKendry, J. J. D.; Massoubre, D.; Cogman, A.; Gu, E.;

Henderson, R. K.; Kelly, A. E.; Dawson, M. D. 1.5 Gbit/s Multi-Channel Visible Light Communications Using CMOS-Controlled GaN-Based LEDs. *J. Light. Technol.* **2013**, *31* (8), 1211–1216.

(45)   Liao, C.-L.; Chang, Y.-F.; Ho, C.-L.; Wu, M.-C. High-Speed GaN-Based Blue Light-Emitting Diodes with Gallium-Doped ZnO Current Spreading Layer. *IEEE Electron Device Lett.* **2013**, *34* (5), 611–613.

(46)   Islim, M. S.; Ferreira, R. X.; He, X.; Xie, E.; Videv, S.; Viola, S.; Watson, S.; Bamiedakis, N.; Penty, R. V; White, I. H.; Kelly, A. E.; Gu, E.; Haas, H.; Dawson, M. D. Towards 10 Gb/s Orthogonal Frequency Division Multiplexing-Based Visible Light Communication Using a GaN Violet Micro-LED. *Photonics Res.* **2017**, *5* (2), A35–A43. https://doi.org/10.1364/PRJ.5.000A35.

(47)   Tian, P.; Liu, X.; Yi, S.; Huang, Y.; Zhang, S.; Zhou, X.; Hu, L.; Zheng, L.; Liu, R. High-Speed Underwater Optical Wireless Communication Using a Blue GaN-Based Micro-LED. *Opt. Express* **2017**, *25* (2), 1193–1201.

(48)   Liu, X.; Tian, P.; Wei, Z.; Yi, S.; Huang, Y.; Zhou, X.; Qiu, Z.-J.; Hu, L.; Fang, Z.; Cong, C. Gbps Long-Distance Real-Time Visible Light Communications Using a High-Bandwidth GaN-Based Micro-LED. *IEEE Photonics J.* **2017**, *9* (6), 1–9.

(49)   Xie, E.; He, X.; Islim, M. S.; Purwita, A. A.; McKendry, J. J. D.; Gu, E.; Haas, H.; Dawson, M. D. High-Speed Visible Light Communication Based on a III-Nitride Series-Biased Micro-LED Array. *J. Light. Technol.* **2018**, *37* (4), 1180–1186.

(50)   Tsonev, D.; Chun, H.; Rajbhandari, S.; McKendry, J. J. D.; Videv, S.; Gu, E.; Haji, M.; Watson, S.; Kelly, A. E.; Faulkner, G. A 3-Gb/s Single-LED OFDM-Based Wireless VLC Link Using a Gallium Nitride $\mu {\rm LED}$. *IEEE photonics Technol. Lett.* **2014**, *26* (7), 637–640.

(51)   Chun, H.; Manousiadis, P.; Rajbhandari, S.; Vithanage, D. A.; Faulkner, G.; Tsonev, D.; McKendry, J. J. D.; Videv, S.; Xie, E.; Gu, E. Visible Light Communication Using a Blue GaN μ LED and Fluorescent Polymer Color Converter. *IEEE Photonics Technol. Lett.* **2014**, *26* (20), 2035–2038.

(52)   Manousiadis, P.; Chun, H.; Rajbhandari, S.; Mulyawan, R.; Vithanage, D. A.; Faulkner, G.; Tsonev, D.; McKendry, J. J. D.; Ijaz, M.; Xie, E. Demonstration of 2.3 Gb/s RGB White-Light VLC Using Polymer Based Colour-Converters and GaN Micro-LEDs. In *2015 IEEE Summer Topicals Meeting Series (SUM)*; IEEE, 2015; pp 222–223.

(53)   Ferreira, R. X. G.; Xie, E.; Mckendry, J. J. D.; Rajbhandari, S.; Chun, H.; Faulkner, G.; Watson, S.; Kelly, A. E.; Gu, E.; Penty, R. V; White, I. H.; O'brien, D. C.; Dawson, M. D. High Bandwidth GaN-Based Micro-LEDs for Multi-Gb/s Visible Light Communications. *IEEE PHOTONICS Technol. Lett.* **2016**, *28* (19). https://doi.org/10.15129/9fae8c57-6d24-42cf-93e3-5a88018deb81.

(54)   Shi, J.-W.; Chi, K.-L.; Wun, J.-M.; Bowers, J. E.; Shih, Y.-H.; Sheu, J.-K. III-Nitride-Based Cyan Light-Emitting Diodes With GHz Bandwidth for High-Speed Visible Light Communication. *IEEE ELECTRON DEVICE Lett.* **2016**, *37* (7). https://doi.org/10.1109/LED.2016.2573265.

(55)   Li, X.; Bamiedakis, N.; Guo, X.; McKendry, J. J. D.; Xie, E.; Ferreira, R.; Gu, E.; Dawson, M. D.; Penty, R. V; White, I. H. Wireless Visible Light Communications Employing Feed-Forward Pre-Equalization and PAM-4 Modulation. *J. Light. Technol.* **2016**, *34* (8), 2049–2055.

(56)   Rajbhandari, S.; Jalajakumari, A. V. N.; Chun, H.; Faulkner, G.; Cameron, K.; Henderson, R.; Tsonev, D.; Haas, H.; Xie, E.; Mckendry, J. J. D.; Herrnsdorf, J.; Ferreira, R.; Gu, E.; Dawson, M. D.; O'brien, D. A Multigigabit per Second Integrated Multiple-Input Multiple-Output VLC Demonstrator. *J. Light. Technol.* **2017**, *35* (20). https://doi.org/10.1109/JLT.2017.2694486.

(57)   Lu, Z.; Tian, P.; Chen, H.; Baranowski, I.; Fu, H.; Huang, X.; Montes, J.; Fan, Y.; Wang, H.; Liu, X.; Liu, R.; Zhao, Y. Active Tracking System for Visible Light Communication Using a GaN-Based Micro-LED and NRZ-OOK. *Opt. Express* **2017**, *25* (15), 17971. https://doi.org/10.1364/OE.25.017971.

(58)   Northrup, J. E. GaN and InGaN (1122) Surfaces: Group-III Adlayers and Indium Incorporation. *Appl. Phys. Lett.* **2009**, *95* (13). https://doi.org/10.1063/1.3240401.

(59)   Zhang, H.; Li, P.; Li, H.; Song, J.; Nakamura, S.; Denbaars, S. P. High Polarization and Fast Modulation Speed of Dual Wavelengths Electroluminescence from Semipolar (20-21) Micro Light-Emitting Diodes with Indium Tin Oxide Surface Grating. *Appl. Phys. Lett.* **2020**, *117* (18). https://doi.org/10.1063/5.0022412.

(60)   Haemmer, M.; Roycroft, B.; Akhter, M.; Dinh, D. V; Quan, Z.; Zhao, J.; Parbrook, P. J.; Corbett, B. Size-Dependent Bandwidth of Semipolar ($11\overline{2}2$) Light-Emitting-Diodes. *IEEE Photonics Technol. Lett.* **2018**, *30* (5), 439–442.

(61)   Rashidi, A.; Monavarian, M.; Aragon, A.; Rishinaramangalam, A.; Feezell, D. Nonpolar M-Plane InGaN/GaN Micro-Scale Light-Emitting Diode With 1.5 GHz Modulation Bandwidth. *IEEE ELECTRON DEVICE Lett.* **2018**, *39* (4). https://doi.org/10.1109/LED.2018.2803082.

(62)   Monavarian, M.; Rashidi, A.; Aragon, A. A.; Oh, S. H.; Rishinaramangalam, A. K.; DenBaars, S. P.; Feezell, D. Impact of Crystal Orientation on the Modulation Bandwidth of InGaN/GaN Light-Emitting Diodes. *Appl. Phys. Lett.* **2018**, *112* (4), 041104. https://doi.org/10.1063/1.5019730.

(63)   Chen, C.-J.; Yan, J.-H.; Chen, D.-H.; Lin, K.-H.; Feng, K.-M.; Wu, M.-C. A 520-Nm Green GaN LED with High Bandwidth and Low Current Density for Gigabits OFDM Data Communication. In *Optical Fiber Communication Conference*; Optical Society of America, 2018; pp Th2A-18.

(64)   Rashidi, A.; Monavarian, M.; Aragon, A.; Okur, S.; Nami, M.; Rishinaramangalam, A.; Mishkat-Ul-Masabih, S.; Feezell, D. High-Speed Nonpolar InGaN/GaN LEDs for Visible-Light Communication. *IEEE Photonics Technol. Lett.* **2017**, *29* (4), 381–384. https://doi.org/10.1109/LPT.2017.2650681.

(65)   Dinh, D. V; Quan, Z.; Roycroft, B.; Parbrook, P. J.; Corbett, B. GHz Bandwidth Semipolar (11¯22) InGaN/GaN Light-Emitting Diodes. **2016**. https://doi.org/10.1364/OL.41.005752.

(66)   Becerra, D. L.; Zhao, Y.; Oh, S. H.; Pynn, C. D.; Fujito, K.; DenBaars, S. P.; Nakamura, S. High-Power Low-Droop Violet Semipolar (30 3¯ 1¯) InGaN/GaN Light-Emitting Diodes with Thick Active Layer Design. *Appl. Phys. Lett.* **2014**, *105* (17), 171106.

(67)   Gardner, N. F. _ GO Müller, YC Shen, G. Chen, S. Watanabe, W. Götz, and MR Krames," Blue-Emitting InGaN–GaN Double-Heterostructure Light-Emitting Diodes Reaching Maximum Quantum Efficiency above 200 A/Cm2. *Appl. Phys. Lett* **2007**, *91*, 243506.

(68)   Funato, M.; Ueda, M.; Kawakami, Y.; Narukawa, Y.; Kosugi, T.; Takahashi, M.; Mukai, T. Blue, Green, and Amber InGaN/GaN Light-Emitting Diodes on Semipolar {11-22} GaN Bulk Substrates. *Jpn. J. Appl. Phys.* **2006**, *45* (7L), L659.

(69)   Bai, J.; Xu, B.; Guzman, F. G.; Xing, K.; Gong, Y.; Hou, Y.; Wang, T. (11-22) Semipolar InGaN Emitters from Green to Amber on Overgrown GaN on Micro-Rod Templates. *Appl. Phys. Lett.* **2015**, *107* (26). https://doi.org/10.1063/1.4939132.

Chapter 2: Background

2.1   Semiconductor device fundamentals

2.1.1   From atoms to crystals

The energies required for specific electronic transitions in an atom can be solved using the Schrödinger equation with appropriate electronic potentials. Figure 2-1 illustrates these electronic transitions in an isolated atom in a crystal. For the isolated atom, E_1 to E_0 is the only transition possibly allowed. Therefore, for a successful electronic transition, a very specific energy is required, i.e., $E_1 - E_0$.
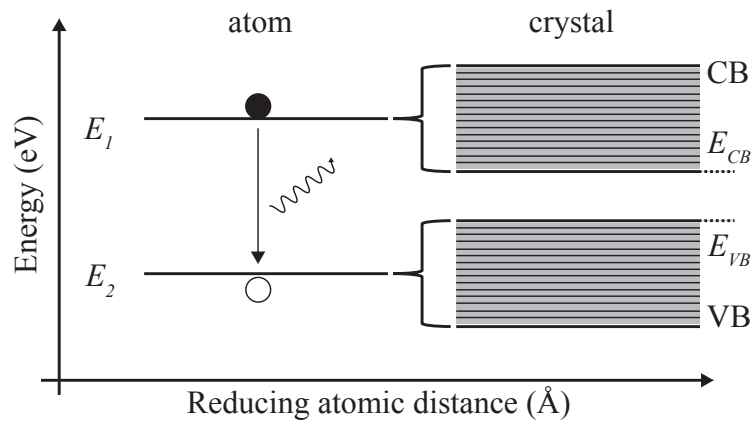
Figure 2-1 Discrete energy levels for an isolated atom and reducing the distance between neighbouring atoms creates energy bands forming a crystal.

However, when bringing two of these isolated atoms near one another to form a covalent bond (i.e., sharing of an electron pair between two atoms) the outer shell electron of one of the atoms arranges itself into either a low-energy bonding (symmetric) charge distribution between the two nuclei or high-energy bonding (asymmetric) distribution in absence of charge between the nuclei. Since there are now two ways the electron can distribute itself around the atoms, the energy levels (E_1 and E_0) splits in two. If another atom is introduced into the system, a new charge distribution which is neither symmetric nor asymmetric is available for the valence electron, meaning a third energy level forms between the two bonding extremes. Adding N covalently bonded atoms in a chain forms N energy levels distributed between the lowest and highest energy bonding states, forming a band of allowed energies. Along the chain of atoms, electron spin-degeneracy allows all N valence electrons to fall in the lower half of the energy band which leaves the upper half vacant[1].

The upper- most energy level (and all levels below) by which all valence electrons fill forms the valence band (VB) and the lowest energy level (and all levels above) in the vacant energy levels forms the conduction band (CB). Since electrons are fermions, they are subject to the Pauli Exclusion Principle (PEP) whereby no two electrons can occupy the same quantum

state. The Fermi-Dirac distribution describes the probability an electron with a given energy, E, and temperature, T, occupies an energy level as[2]

$$F(E) = \frac{1}{1 + e^{(E-E_F)/k_B T}},$$ (2-1)

where k_B is the Boltzmann constant and E_F is the Fermi level energy. The Fermi level is the energy at which the probability of finding an occupied electron is exactly 0.5 at a given temperature. At absolute zero (0 K), the Fermi level is the highest possible energy level an electron can occupy and therefore the probability of finding an electron below this level is certain i.e., $F(E, T = 0\ K) = 1$ for $E < E_F$[3].

2.1.2 Crystal band structure

Next, we consider how electrons traverse through a semiconductor crystal. The energy of a free electron in a vacuum is given by

$$E = \frac{p^2}{2m_0},$$ (2-2)

where p is the momentum and m_0 is the free-electron mass. If we then place this electron in a semiconductor crystal, m_0 is replaced with an effective mass m_n (the subscript n referring to the electron's intrinsic negative charge) since the electron is subject to the influence of all the other electrons and the periodic potential created by the chain of atoms within the crystal, which restricts and changes its movement. For this reason, the effective mass is usually given as a fraction of the free electron mass. Taking the second derivative of energy with respect to momentum in Equation 2-2 allows us to obtain an expression for the effective mass i.e.,

$$m_n = \left(\frac{d^2 E}{dp^2}\right)^{-1}.$$ (2-3)

The difference in energy between the VB maxima and CB minima is called the bandgap energy i.e., E_g, which is the minimum energy required for an electron in the VB to be excited to the CB. The excited electron in the CB can freely move through the crystal, leaving behind a freely moving quasi-particle in its now vacant place in the VB called a hole with opposing properties to the electron i.e., positively charged $+e$ and with effective mass m_p.

Plotting the energy verses momentum relationship with electron effective mass $m_n = 0.5\ m_0$ and hole effective mass $m_p = m_0$ gives us the energy band diagram of a simple semiconductor, as shown in Figure 2-2a. The effective mass is heavily dependent on the material properties of the semiconductor. For the narrower CB parabola in Figure 2-2a, the larger the second derivative in Equation 2-3 resulting in a smaller effective electron mass.

This effective mass concept greatly simplifies complex semiconductor band structures and allows us to treat a single electron or hole moving through a semiconductor crystal as a classical particle. This diagram i.e., the $E(k)$ diagram, is known as the dispersion relationship and describes the energy band structure of specific semiconductors which are often much more complicated than drawn here. Momentum, p on the x-axis is usually substituted with the wavenumber, k with the relation $p = \hbar k$.
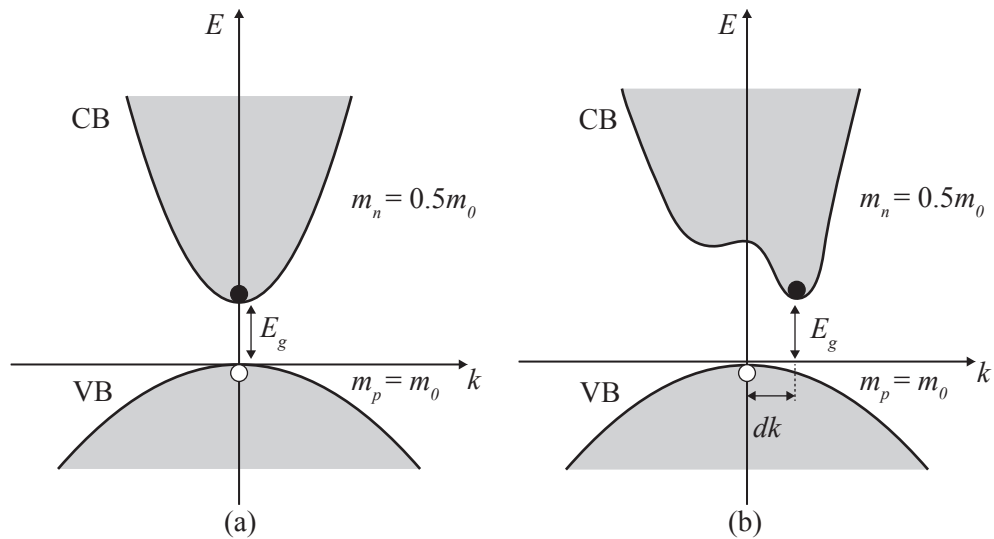
Figure 2-2 Dispersion relationship of a simple semiconductor with effective mass $0.5m_0$ and m_0 for electrons and holes respectively: as a direct bandgap semiconductor (a) and an indirect bandgap semiconductor (b).

Up to now, it was assumed that the bandgap in semiconductors occur at the same point in k-space i.e., at the same wavevector or momentum vector. This is true for a direct bandgap semiconductor. However, for some materials this is not the case. Figure 2-2b shows how the bandgap energy can vary with k. Therefore, along with an electrical or optical excitation, the electrons need an additional dk (the difference in electron and hole momentum often in the form of a lattice vibration called a phonon) for a successful transition. This is known as an indirect semiconductor. Involving a phonon in this process means radiative processes are much less likely to occur and offers much longer recombination lifetimes than direct bandgap materials. GaN, AlN and InN for example, all possess direct bandgaps, therefore from a material perspective, radiative processes can be optimised[4].

2.1.3   Carrier concentration and doping under thermal equilibrium

The conductivity of a semiconductor depends on the densities of free carriers within the semiconductor (electrons and holes) and their mobilities, which can be described by

$$\sigma = e(n_0\mu_n + p_0\mu_p), \qquad (2\text{-}4)$$

where e is the elemental charge of an electron (1.602×10^{-19} C), μ_n and μ_p are the electron and hole mobilities, respectively. The mobility is a material parameter which describes how easily electrons and holes can move through a material in response to an electric field.

For an intrinsic semiconductor, the carrier density labelled as n_i is

$$n_i = \sqrt{N_{CB}N_{VB}}\, e^{\left(-\frac{E_g}{2k_BT}\right)} \tag{2-5}$$

where N_{CB} and N_{VB} are the effective density of states in the CB and VB respectively. Adding impurities to a semiconductor generates an excess of free carriers, increasing the carrier concentration at equilibrium therefore increasing the conductivity of the material, a technique known as doping. Dopants can be either p-type (acceptor - holes) or n-type (donor - electrons) depending on which column in the periodic table they fall i.e., how many valence electrons they have and whether they have more valence electrons than the atoms in the intrinsic semiconductor they replace. For example, in a III-V semiconductor such as GaN, Magnesium atoms which are a group II element, can be used as an p-type dopant to generate excess holes in the valence band. Similarly, a group IV element like Si can be used as an n-type dopant for obtaining n-type GaN, generating an excess of electrons. Introducing dopants into the intrinsic semiconductor creates allowed energy states slightly below the CB for n-type dopants and slightly above the VB for p-type dopants. These shallow dopant states usually only require a small amount of energy, around k_BT (0.026 eV) at room temperature, for complete ionisation of the free carriers[3]. Under this condition therefore, the electron and hole carrier densities are equal to the donor and acceptor concentrations, respectively i.e., $n = N_D$ and $p = N_A$. Since the CB and VB density of states available for carriers to occupy changes with N_D, and N_A, the Fermi level will also shift towards the highest concentration of free carriers to either the CB or VB depending on type of doping as shown in Figure 2-3.
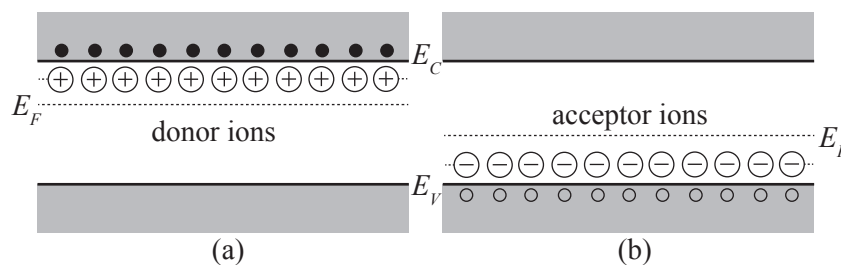
Figure 2-3 Effect of doping on the energy band diagram for n-type (a) and p-type (b) semiconductors.

2.1.4   Recombination

Without any external excitation (i.e., under equilibrium conditions at a given temperature) the law of mass action states that in a semiconductor crystal the product of equilibrium electron and hole carrier concentrations is a constant value i.e.,

$$n_0 p_0 = n_i{}^2, \tag{2-6}$$

under the assumption that the doped semiconductor discussed previously is non-degenerate i.e., not highly doped. Upon excitation, statistically, it is more probable for electrons to relax down from their excited state in the CB and recombine with a hole in the VB via a radiative (with a production of a photon) or non-radiative process than to remain in the CB. There are three main types of radiative processes: spontaneous band-edge, exciton, and donor-acceptor recombination. The less desirable non-radiative processes are mainly caused by Schockley-Reed-Hall (SRH) recombination and Auger recombination. These are demonstrated schematically in Figure 2-4 and discussed in more detail below.
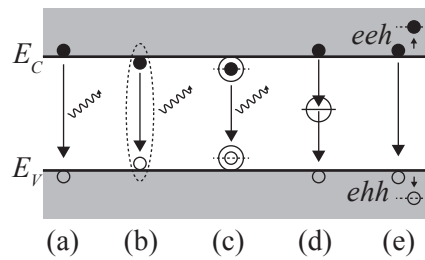
Figure 2-4 recombination mechanisms in semiconductors: spontaneous band-edge recombination (a), exciton pair recombination (b), donor-acceptor recombination (c) Schockley-Reed-Hall (SRH) recombination (d) and Auger recombination (e).

Radiative

After excitation, whether it be electronically or optically, excess carriers are introduced such that the total carrier concentration is the sum of the equilibrium and excess concentrations i.e., $n = n_0 + \Delta n$ and $p = p_0 + \Delta p$. For radiative processes, the probability that this event occurs is governed by the radiative recombination rate, R_{rad}, and is proportional to the product of the electron and hole concentrations along with a material constant called the bimolecular recombination coefficient i.e.,

$$R_{rad} = B(n_0 + \Delta n)(p_0 + \Delta p). \tag{2-7}$$

B has a typical value of 10^{-9} - 10^{-11} cm³/s in III-nitrides[5].

Figure 2-4a demonstrates the simplest radiative transition, whereby an excited electron at the CB edge spontaneously recombines with a hole at the VB edge emitting a photon equal to the bandgap of the material. Under certain temperatures and due to the coulombic attraction between an electron and a hole, the electron-hole pair can bind to one another forming a

stable exciton as shown in Figure 2-4b. The exciton acts as a single particle with neutral charge. Eventually, the exciton recombines except the energy released in recombination is reduced by the exciton binding energy i.e., $E_g - E_n$. The exciton binding energy depends on the material, for example, GaN has an exciton binding energy of 25 meV suggesting that stable excitons can form at room temperature (from $k_B T$)[6]. As discussed previously, dopants introduce allowed energy states within the bandgap of the intrinsic semiconductor. Figure 2-4c describes how electrons recombine with holes through the impurity induced states, releasing a photon with an energy $E_g - E_a$, where E_a is the ionisation energy of the dopant.

We can look more closely at the radiative recombination dynamics of a semiconductor subject to a small excitation by modelling the generation and recombination of free carriers as a function of time. Since electron-hole pairs recombine together instantaneously, the steady state and excess carrier concentrations are equal i.e., $\Delta n(t) = \Delta p(t)$. At low excitation levels, the excess generation rate is much less than the total carrier concentration i.e., $\Delta n(t) \ll n_0 p_0$, under these assumptions and multiplying out Equation 2-7 then rearranging gives us

$$R_{rad} = B n_i{}^2 + B(n_0 + p_0)\Delta n(t) = R_0 + R_{excess},\qquad(2\text{-}8)$$

where the left summand of Equation 2-8 denotes the equilibrium recombination rate and right summand the excess recombination rate. The net rate of change of carriers in the semiconductor is the difference between the generation rate and recombination rate of carriers i.e., $G - R$ encompassing contributions from carriers in equilibrium (G_0 and R_0) and excess carriers introduced by the excitation (G_{excess} and R_{excess}). Considering an excitation source which is switched off when $t = 0$, then $G_{excess} = 0$ and $G_0 = R_0$, Equation 2-8 can be rewritten as

$$\frac{d}{dt}\Delta n(t) = -B(n_0 + p_0)\Delta n(t)\qquad(2\text{-}9)$$

with a general solution

$$\Delta n(t) = \Delta n_0 e^{-B(n_0 + p_0)t}.\qquad(2\text{-}10)$$

where $\Delta n_0 = \Delta n$ at $t = 0$. Collecting the constants in the exponential yields

$$\Delta n(t) = \Delta n_0 e^{-t/\tau_{rad}}\qquad(2\text{-}11)$$

where τ_{rad} denotes the radiative carrier lifetime of a simple semiconductor which is the average time taken for the luminescence decay to reach $1/e$ of its initial value. Depending on the doping level, τ_{rad} changes to

$$\tau_{rad} = \frac{1}{B(n_0 + p_0)}, \quad \text{for undoped semiconductors,} \tag{2-12}$$

$$\tau_{rad} = \frac{1}{BN_A}, \quad \text{for p-type semiconductors,} \tag{2-13}$$

$$\tau_{rad} = \frac{1}{BN_D}, \quad \text{for n-type semiconductors.} \tag{2-14}$$

From Equation 2-11, the luminescent decay of minority carriers follows a single exponential decay. In more complex structures such as multiple-quantum well (MQW) InGaN LEDs, mono-exponential decays are seldom seen due to a convolution of the various radiative processes described above in Figure 2-4 along with non-radiative mechanisms. Figure 2-5 describes illustratively how the luminescence of InGaN evolves with time.
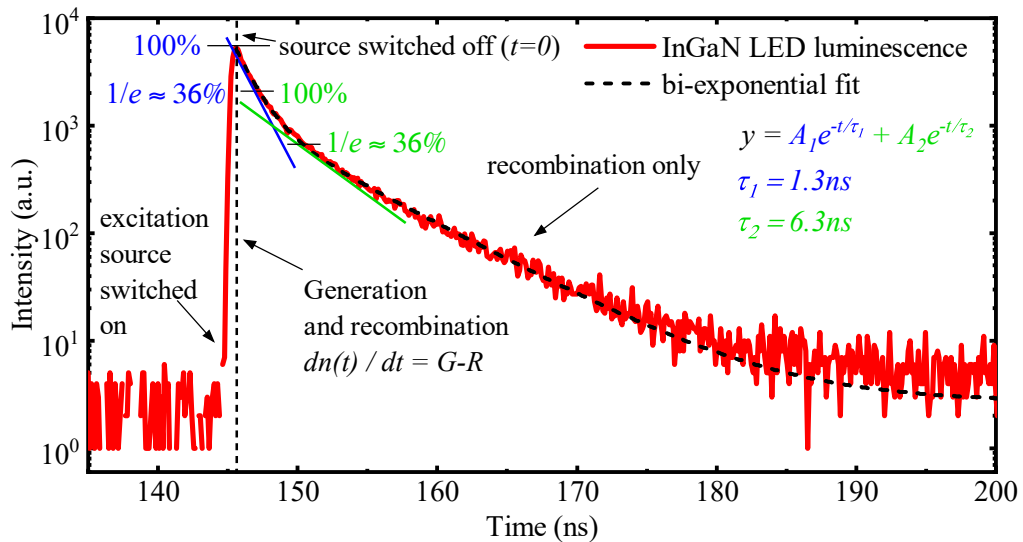
Figure 2-5 An InGaN semiconductor subject to a photoexcitation source and resulting luminescent decay, deviating from a conventional single exponential function.

Non-radiative

SRH recombination, which is a non-radiative process, is shown in Figure 2-4d. SRH recombination occurs when trap levels are created within the bandgap of the semiconductor, often caused by defects in the lattice which interrupt the periodicity. An excited electron in the CB can recombine with a hole via multiple phonon emissions through many trap levels. The rate of SRH recombination therefore is dependent on the trap's capture cross-section, σ_e, electron thermal velocity, v_{th}, and trap density, N_T, i.e.,

$$R_{SRH} = \sigma_e v_{th} N_T n = An. \tag{2-15}$$

Since SRH is predominantly a single particle process, under low excitation SRH is expected to be the dominating source of non-radiative recombination.

The second non-radiative process is shown in Figure 2-4e, namely, Auger recombination. Auger recombination involves three carriers, two electrons and one hole in the CB (eeh) or one electron and two holes in the VB (ehh) and is therefore statistically more likely to occur under higher excitation levels. Auger recombination is like spontaneous band-edge recombination, but the energy released in recombination is instead used to excite another carrier deep into the energy band. The 'hot' carrier will then relax down to the band-edge by releasing multiple phonon emission. The rate of Auger recombination is described by

$$R_{Auger} = Cn^3,\tag{2-16}$$

where C is the Auger coefficient.

The total recombination rate is therefore a sum of the three main contributors to recombination, i.e.,

$$R_{total} = R_{rad} + R_{SRH} + R_{Auger}.\tag{2-17}$$

Total carrier lifetime

The average time for an electron and hole to recombine is governed by the carrier lifetime in Equation 2-12. However, this is for purely spontaneous radiative recombination. The actual carrier lifetime of a semiconductor is a weighted sum from both radiative and non-radiative lifetimes stemming from the various transition mechanisms described above i.e.,

$$\tau_{total}{}^{-1} = \tau_{rad}{}^{-1} + \tau_{non-rad}{}^{-1}\tag{2-18}$$

Therefore, it is often useful to modify Equation 2-12 to various non-monoexponential decay models such as bi-exponentials, tri-exponentials and stretched exponentials to fit the luminescence profile of the sample. Under temperature dependent measurements, τ_{rad} and $\tau_{non-rad}$ can be separated under the assumption that non-radiative recombination centres are frozen at low temperature.

2.1.5   p-n Junctions and Heterojunctions

In this section, we bring a p-type and n-type semiconductor together to form a pn-junction. The carrier transport process for a simple pn-junction under zero bias (0 V) is shown in Figure 2-6. As the two doped layers of semiconductor material are brought together, negatively charged electrons in the n-type material and positive charged holes in the p-type material will diffuse toward the opposite directions due to the carrier concentration gradient, leaving positive charges in the n-type layer and negative charges in the p-type layer which eventually

builds up an electric field. A depletion region devoid of free carriers forms between the n-type layer and the p-type layer. Equilibrium in the junction occurs due to the build-up in electrostatic potential V_b which prevents further diffusion across the interface. Therefore, an external electric field is needed for current to flow, and only under forward bias. The applied forward voltage reduces the depletion width, lowers the potential barrier height, and allows carriers to diffuse through the interface.
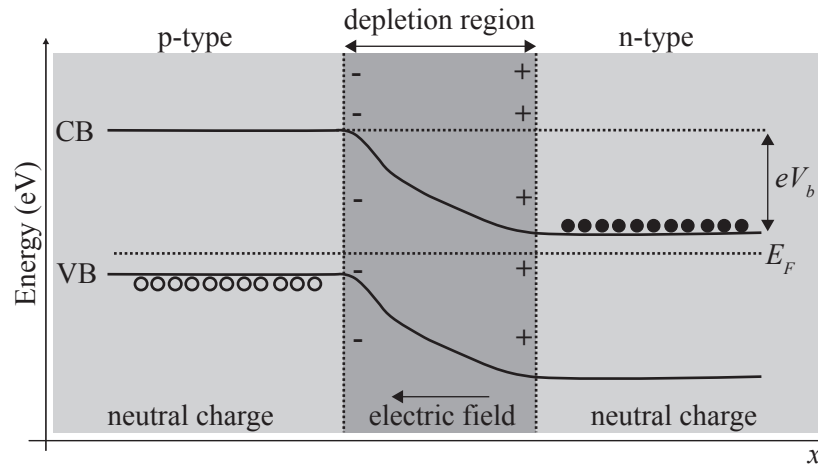
Figure 2-6 Schematic illustration of a pn-junction under 0V bias.

2.1.6   Light emitting diodes (LEDs)

LEDs utilise the radiative properties discussed in Section 2.1.4. A typical GaN based LED is shown in Figure 2-7. Firstly, a GaN nucleation layer is used to accommodate the lattice mismatch between the sapphire and GaN therefore promoting GaN growth. The pn-junction in this case consists of a low dimensional active region between a p-GaN and n-GaN layer. The active region serves to confine the carriers in 1D (quantum well), 2D (quantum wire) or 3D (quantum dot) depending on the strength of confinement. The active region size must be reduced to the order of the de Broglie wavelength so that the carriers are sufficiently confined, and their available energy states quantised. Therefore, when an electron and hole recombine, the released energy not only depends on the bandgap of the semiconductor, but also the energy level at which the carriers are confined in the active region, i.e., for a quantum well sandwiched with two infinite potential barriers,

$$E_n = \frac{1}{m_n}\left(\frac{\pi\hbar n}{L}\right)^2, \qquad (2\text{-}19)$$

where E_n is the discrete energy of the quantum well, which is the so-called quantization energy, n is the principal quantum number and L is the quantum well thickness. Most commercially available visible light LEDs use a quantum well structure as the active region. Such a structure can be formed by sandwiching together a material with a smaller bandgap between two other materials with a larger bandgap, creating a heterostructure. Quantum wells

and barriers are formed by the smaller and larger bandgap materials, respectively. A current spreading layer (CSL) is used to help distribute the current across the whole device and prevent current crowding around the contact. These are usually made transparent such that the generated light can escape from the top of the device. An electron blocking layer (EBL) is used to prevent current leakage out of the active region.
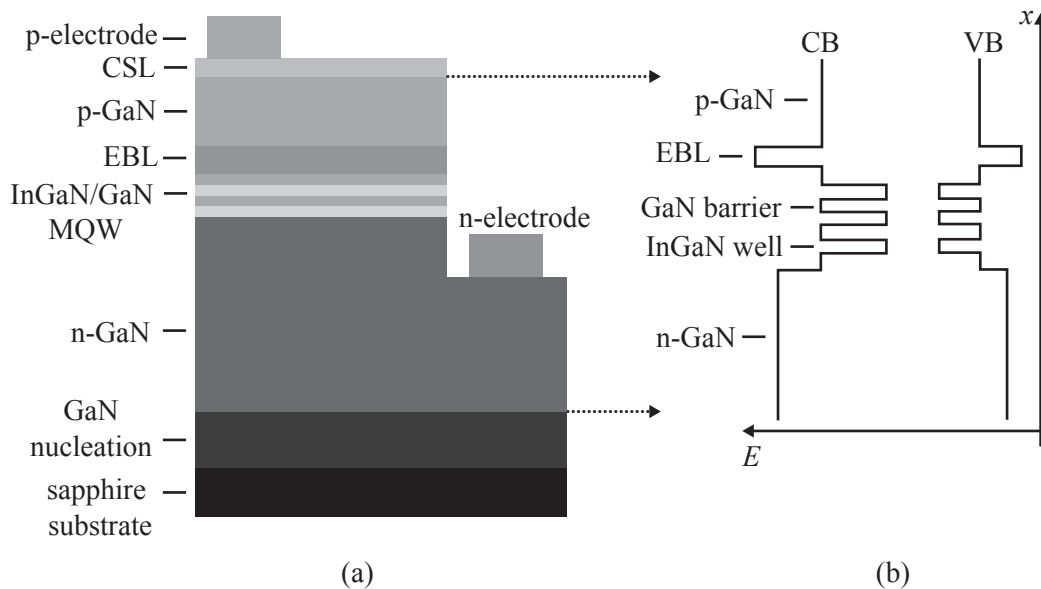
Figure 2-7 InGaN/GaN LED epitaxy structure (a) and corresponding band diagram (b).

2.1.7 High-electron mobility transistors (HEMTs)

HEMTs are heterojunctions-based devices where the current flow between the two terminals (called source and drain) is controlled by a third terminal (gate). A metal is used for the gate terminal to form a metal-semiconductor junction, where a Schottky barrier is formed between the metal and the semiconductor and is characterised by its barrier height ϕ_B. The contact for a source and a drain must be ohmic.

2.2 III-nitride semiconductors

This section aims to specifically explain GaN based semiconductors, and how semipolar and nonpolar LEDs can mitigate some of the main problems associated with the III-nitride material system.

2.2.1 Crystal structure

GaN exists in three types of crystalline structures: wurtzite, zinc-blende, and rock salt. The most common and thermodynamically stable under ambient conditions is the wurtzite (or hexagonal) structure. The work done in this thesis will focus on devices fabricated from this structure.

The crystal structure of wurtzite GaN is shown in Figure 2-8. Two lattice constants, *c,* and *a*, corresponding to the length of the unit cell along the vertical direction and the basal-plane lattice constant, respectively, can describe the structure. Multiple unit cells can be joined together in a hexagonal closed packed (HCP) arrangement along the c-plane direction, wurtzite GaN is therefore said to have a hexagonal symmetry. The structure can be either Ga terminated which is the so-called Ga face (+c plane) or nitrogen terminated which is the so called Nitrogen face (-c plane). The physical and chemical properties are therefore different in the +c and -c directions. The Ga and N atoms are tetrahedrally bonded together but with slight distortions with respect to the bond angle and length. Due to this imbalance, there exists a net polarisation in the +c direction i.e., an electric field, which, as we discuss below, is the fundamental property behind many issues with devices grown along this direction.
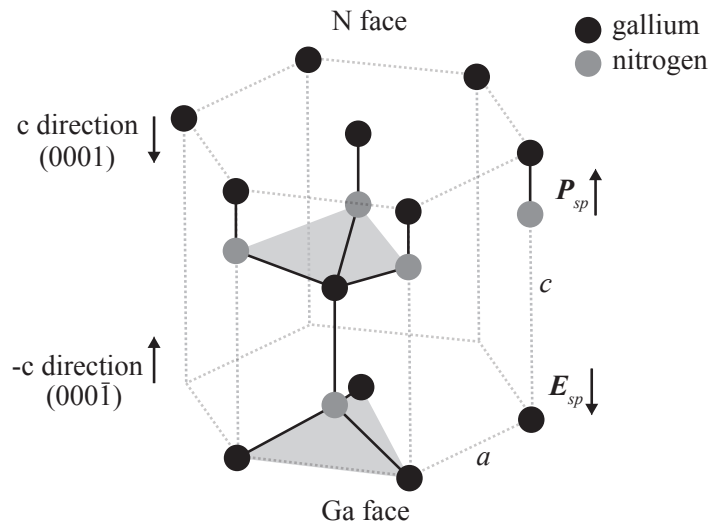
Figure 2-8 GaN wurtzite structure, shaded regions indicating the tetrahedral bonding of N and Ga atoms.

Material properties

As mentioned previously, the AlGaInN system offer direct bandgaps allowing tuneable alloy compositions from the deep UV to the near infrared spectral range. In many semiconductor systems, the bandgap can be simply described linearly as a function of lattice constant using Vegard's law[4]. In a more accurate manner, an extra non-linear term known as the bowing parameter, *b*, is required to account for the deviation from a linear relationship. The resulting bandgap energy of the ternary alloy (either InGaN or AlGaN) can be expressed as

$$E_g(A_xB_{1-x}N) = E_g(A)x + E_g(B)(1-x) - x(1-x)E_b \qquad (2\text{-}20)$$

Where A and B are different binary alloys of GaN, InN, and AlN, E_b is the bowing parameter and *x* is the alloy fraction. The material properties of these three binary alloys are shown in Table 2-1[5].

Table 2-1 Material parameters of wurtzite structure III-nitrides.

material	a (Å)	c (Å)	E_g (eV)	λ (nm)
GaN	3.191	5.185	3.42	363
AlN	3.112	4.982	6.20	200
InN	3.545	5.403	0.78	1590

Electrical properties

The electrical and thermal properties of GaN along with the other major semiconductors is shown in Table 2-2. The wide bandgap (WBG) of GaN means a very high breakdown voltage. This property, coupled with intrinsically high thermal conductivity, makes GaN devices ideal for high-power, high-frequency and high temperature applications where efficient heat dissipation is crucial. In addition, WBG semiconductors such as GaN result in fabricated devices with lower on-resistance and switching losses than a Si-based device with comparable voltage and current capabilities[7]. The electron mobility of GaN is the only property where it lags compared with other more mature semiconductors. Since mobility is dependent on various factors such as impurities and defects within the crystal, optimising growth conditions and therefore crystal quality is important for high frequency applications such as visible light communications (VLC).

Table 2-2 Approximate electrical and thermal properties of GaN compared with other major semiconductors at room temperature, 300K.

material	electron mobility ($cm^2 V^{-1} s^{-1}$)	hole mobility ($cm^2 V^{-1} s^{-1}$)	breakdown field ($M V cm^{-1}$)	thermal conductivity ($W cm^{-1} K^{-1}$)
GaN	**1245**[8]	**150**[31]	**3.3**[9]	**2.3**[10]
GaAs	9400[11]	1000[32]	0.4[12]	0.55[11]
Si	1400[13]	300[33]	0.3[3]	1.56[14]
SiC	380[15]	40[34]	3[16]	3.6[16]
InP	5400[17]	120[35]	0.5[12]	0.68[18]

2.2.2 Polarisation

In an ideal wurtzite structure, the lattice constant ratio i.e., c/a is calculated to be $\sqrt{8/3}$=1.633. In reality, wurtzite GaN is 1.626[19,20]. This means that there is a slight asymmetry in the tetrahedron made up of Ga and N atoms, leaving some charge uncompensated for and resulting in a net, spontaneous polarisation field in the +c-direction i.e., P_{sp}. For unstrained GaN, InN and AlN, the spontaneous polarisations are 0.029, 0.032 and 0.081 C/m², respectively[21]. Mechanical strain caused by lattice mismatch between different materials can result in the tetrahedral bonding configuration to become further distorted, increasing the effect of the polarisation field. This is known as piezoelectric polarisation i.e., P_{pz}, which can

either oppose or contribute to the spontaneous polarisation, depending on the type of strain being compressive or tensile. In compressive strain, such as in an InGaN/GaN heterostructure, the direction of P_{pz} is in the opposite direction to P_{sp} as InGaN is compressed when grown on a GaN surface. AlGaN grown on GaN in contrast results in tensile strain, causing P_{pz} and P_{sp} to align along the same field direction. The total polarisation field, P_{tot}, is therefore the sum of both sources of polarisation i.e., $P_{tot}= P_{sp}+ P_{pz}$. This is illustrated schematically in Figure 2-9 for different heterostructures.
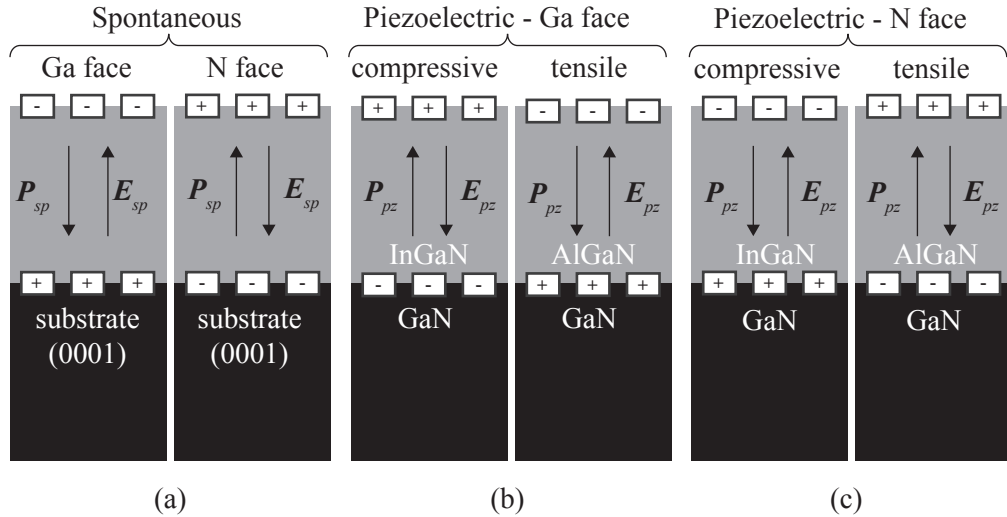
Figure 2-9 Spontaneous polarisation field and resulting electric field direction for GaN on sapphire (a). Piezoelectric field direction and corresponding electric field directions for InGaN/GaN and AlGaN/GaN heterostructures for (b) Ga face and (c) N face.

2.2.3   Semipolar and nonpolar GaN

The strain induced piezoelectric field drastically changes optoelectronic devices such as LEDs grown along the c-plane GaN direction. The electron-hole wavefunctions move further apart in the quantum well region leading to long radiative recombination times and reduced device efficiency, i.e., the QCSE. Adding more indium content to the InGaN/GaN region for longer wavelength emitters for example, such as green, yellow, and amber further increases the strain due to the increased lattice-mismatch between layers enhancing the QCSE. A promising solution to this is by epitaxially growing along a semipolar or nonpolar GaN direction, thereby reducing or eliminating the strain induced piezoelectric field.

Reduced QCSE

The earliest work on semipolar and nonpolar GaN was a theoretical approach to calculating the piezoelectric fields in a strained 3nm InGaN/GaN quantum well as a function of the polar angle from the c-axis[22]. The results proved that the lowest electron-hole transition probability occurred along the c-plane direction, where the polarisation field strength was highest. Consequently, as the angle from this axis increases, the transition probability increases

significantly as the polarisation fields reduces. Crystal facets which are orientated perpendicular to the *c-plane* direction are called nonpolar planes, i.e., the a-*plane* and *m-plane* which eliminate piezoelectric fields. Orientations which lie in-between these two planes are semipolar, where the piezoelectric fields are reduced depending on the angle subtended from the c-axis. Some crystal facets of interest are shown in Figure 2-10a-d.
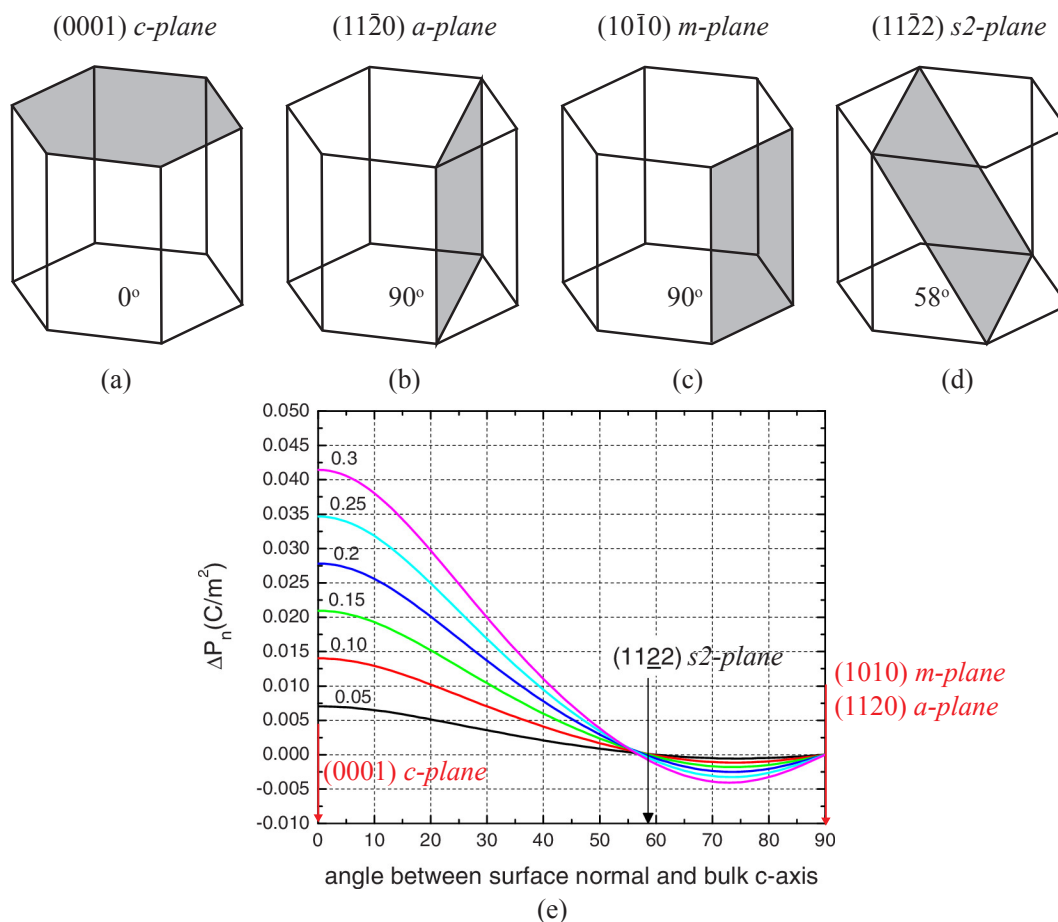
Figure 2-10 Crystal orientations of wurtzite GaN and their angles with respect to *c-plane*: polar (a) *c-plane*, nonpolar (b) *a-plane* and (c) *m-plane* and semipolar (d) *s2-plane*. (e) The polarisation of InGaN with different indium content as a function of angle with respect to *c-plane*[23].

Figure 2-10e shows how the polarisation changes with indium content with respect to *c-plane*. The polarisation significantly reduces with angles >60° with respect to the c-axis and indium composition has a reduced dependence on the amount of polarisation in the structure. Therefore, longer wavelength emitters with higher efficiency should be achievable due to the reduced (eliminated) dependence of polarisation along semipolar (nonpolar) planes. Because of these highly attractive benefits, a considerable amount of effort has been devoted to utilising the semipolar and nonpolar orientations for GaN growth.

Enhanced indium incorporation

As was discussed previously, it is very difficult to achieve long wavelength emitters such as green, yellow, or red with high indium compositions (typically >20%[24]) without drastically reducing the efficiency and optical performance using *c-plane* GaN. This is because in general, higher indium contents are achieved by lowering the growth temperature which is detrimental to crystal quality[25].

Indium incorporation into an InGaN semiconductor relies on the indium chemical bonding energy, which in polar and nonpolar directions are very high, and therefore restricts high indium composition emitters with high efficiency. Semipolar structures however, for example, the $(11\bar{2}2)$ plane have the advantage of enhanced indium incorporation due to the significantly lower indium chemical potential arising from the orientation's specific surface structure[23]. This means more indium atoms can be accommodated on semipolar surfaces at potentially higher growth temperatures, suggesting crystal quality can be improved over polar and nonpolar orientations for longer wavelength emitters. A recent report measuring the emission properties of InGaN quantum well structures grown at different orientations under identical growth conditions shows that the $(11\bar{2}2)$ plane structure exhibited the longest wavelength compared with the other orientations[26]. This demonstrates the key advantage of the growth along the $(11\bar{2}2)$ plane. Another report demonstrated that the indium incorporation efficiency is 2-3 times less on nonpolar surfaces than for *c-plane* GaN[27], suggesting semipolar LEDs are better equipped for developing longer wavelength emitters.

2.2.4   Overgrowth technique for $(11\bar{2}2)$ GaN on sapphire

Since there exists a large lattice mismatch (16%) between GaN and sapphire, the growth of $(11\bar{2}2)$ GaN contains many more defects in the form of basal stacking faults (BSF) compared to its *c-plane* counterpart as well as the dislocations common to both orientations. The reason for this is that BSFs are restricted to the interface of GaN and sapphire and are perpendicular to the growth direction. In the *c-plane* orientation, the BSFs cannot extend up to the surface of the sample and as a result there is no concern for device performance. In $(11\bar{2}2)$ GaN however, the BSF planes are inclined to the growth direction, meaning they can eventually extend upwards towards the surface of the sample which would strongly affect device electrical and optical performance. For this reason, it is very difficult to grow semipolar GaN with good crystal quality on sapphire.

To address the defect related issues, our group has recently developed a cost-effective overgrowth technique using regularly arrayed micro-rod templates demonstrating crystal quality comparable to commercial *c-plane* GaN wafers. The growth process is shown in Figure 2-11. Initially, $(11\bar{2}2)$ GaN is grown on a 2-inch *m-plane* sapphire wafer using our

high temperature AlN buffer technique by metal organic chemical vapour deposition (MOCVD)[28]. This is followed by the deposition of a SiO_2 layer using plasma enhanced chemical vapor deposition (PECVD). A standard photolithography process is then used to pattern the SiO_2 with a series of regularly arrayed circles. Then, a nickel layer is deposited using thermal evaporation after which a lift-off process is used to remove the photoresist. Reactive ion etching (RIE) is then used to etch any exposed SiO_2 areas to form the micro-rods. The nickel is then removed using wet etching. The patterned semipolar GaN micro-rod template is then loaded back into the MOCVD chamber for overgrowth of $(11\bar{2}2)$ GaN. The overgrowth takes place from the exposed sidewalls of the micro-rods and eventually overflows over the top of the micro-rods and coalescences into an atomically flat surface (when the overflow thickness reaches about 4 μm). This method serves to reduce the BSF associated with the semipolar planes due to the SiO_2 effectively blocking any BSF or dislocation development to the surface. As a result, dislocation and BSF densities were reported for typical wafers as low as 2×10^8 cm^{-2} and 4×10^4 cm^{-2}, respectively[29].

(a) (11-22) growth   (b) SiO_2 deposition   (c) Photoresist deposition   (d) Photolithography pattern

(h) Overgrow (11-22) GaN   (g) Remove Ni, wet etch   (f) Remove photoresist, RIE, ICP etch   (e) Ni deposition
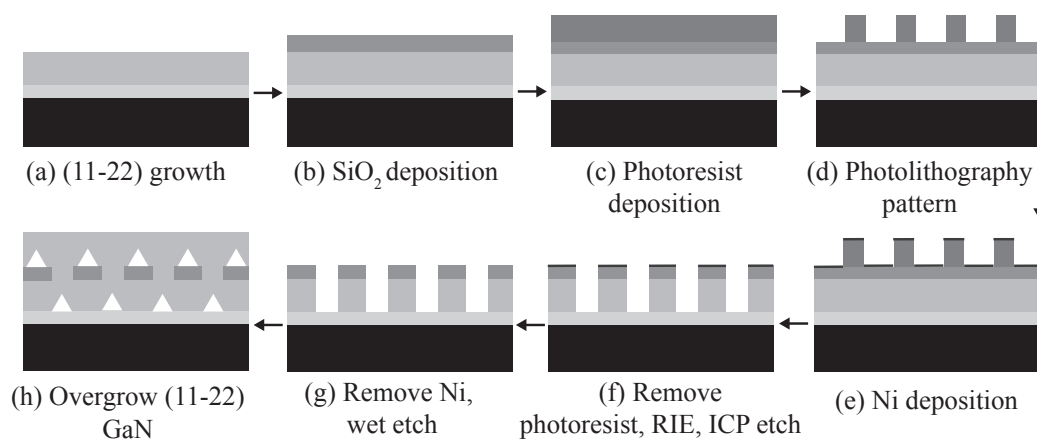
Figure 2-11 Micro-rod template fabrication and overgrowth process.

Due to the step-change in crystal quality achieved by our novel overgrowth method in developing $(11\bar{2}2)$ GaN on sapphire, semipolar LEDs with emission wavelengths up to the amber spectral region with low efficiency droop was successfully demonstrated[30]. The work in this thesis will aim to utilise these LEDs to unlock long wavelength VLC and progress towards the ultimate goal of monolithic integration of an RGB chip capable of general illumination as well as the additional capability of Gb/s data transmission rates.

2.3   References

(1)   Coldren, L. A.; Corzine, S. W.; Mashanovitch, M. L. *Diode Lasers and Photonic Integrated Circuits*; John Wiley & Sons, 2012.

(2)   Kittel, C.; McEuen, P. *Kittel's Introduction to Solid State Physics*; John Wiley & Sons, 2018.

(3)   Sze, S. M.; Li, Y.; Ng, K. K. *Physics of Semiconductor Devices*; John wiley & sons, 2021.

(4)   Schubert, E. F. *LIGHT-EMITTING DIODES*.

(5)   Morkoç, H. *Nitride Semiconductors and Devices*; Springer Science & Business Media, 2013; Vol. 32.

(6)   Fox, M. Optical Properties of Solids. American Association of Physics Teachers 2002.

(7)   Jones, E. A.; Wang, F. F.; Costinett, D. Review of Commercial GaN Power Devices and GaN-Based Converter Design Challenges. *IEEE J. Emerg. Sel. Top. Power Electron.* **2016**, *4* (3), 707–719.

(8)   Look, D. C.; Sizelove, J. R. Predicted Maximum Mobility in Bulk GaN. *Appl. Phys. Lett.* **2001**, *79* (8), 1133–1135.

(9)   Gaskill, D. K.; Brandt, C. D.; Nemanich, R. J. *III-Nitride, SiC and Diamond Materials for Electronic Devices. Symposium Held April 8-12 1996, San Francisco, California, USA Volume 423.*; MATERIALS RESEARCH SOCIETY PITTSBURGH PA, 1996.

(10)   Sichel, E. K. Thermal Conductivity of GaN, 25-360 K. *J. Phys. Chem. Solids* **1977**, *38* (3), 330.

(11)   Blakemore, J. S. Semiconducting and Other Major Properties of Gallium Arsenide. *J. Appl. Phys.* **1982**, *53* (10), R123–R181.

(12)   Kyuregyan, A. S.; Yurkov, S. N. Room-Temperature Avalanche Breakdown Voltages of p-N# 3 Junctions Made of Si, Ge, SiC, GaAs, GaP, and InP. *Sov. Physics--Semiconductors(English Transl.* **1989**, *23* (10), 1126–1131.

(13)   Canali, C.; Jacoboni, C.; Nava, F.; Ottaviani, G.; Alberigi-Quaranta, A. Electron Drift Velocity in Silicon. *Phys. Rev. B* **1975**, *12* (6), 2265.

(14)   Glassbrenner, C. J.; Slack, G. A. Thermal Conductivity of Silicon and Germanium from 3 K to the Melting Point. *Phys. Rev.* **1964**, *134* (4A), A1058.

(15)   Nishino, S.; Powell, J. A.; Will, H. A. Production of Large-area Single-crystal Wafers of Cubic SiC for Semiconductor Devices. *Appl. Phys. Lett.* **1983**, *42* (5), 460–462.

(16)   Levinshtein, M. E.; Rumyantsev, S. L.; Shur, M. S. *Properties of Advanced Semiconductor Materials: GaN, AIN, InN, BN, SiC, SiGe*; John Wiley & Sons, 2001.

(17)   Razeghi, M.; Maurel, P.; Defour, M.; Omnes, F.; Neu, G.; Kozacki, A. Very High Purity InP Epilayer Grown by Metalorganic Chemical Vapor Deposition. *Appl. Phys. Lett.* **1988**, *52* (2), 117–119.

(18)   Slack, G. A. The Thermal Conductivity of Nonmetallic Crystals. *Solid state Phys.* **1979**, *34*, 1–71.

(19)   Harrison, P.; Jeffrey, G. A.; Townsend, J. R. An Experimental Study of the Anomalous Scattering of Mo Kα Radiation by Single Crystals of ZnO. *Acta Crystallogr.* **1958**, *11* (8), 552–556.

(20)   Ueno, M.; Yoshida, M.; Onodera, A.; Shimomura, O.; Takemura, K. Stability of the Wurtzite-Type Structure under High Pressure: GaN and InN. *Phys. Rev. B* **1994**, *49* (1), 14.

(21)   Bernardini, F.; Fiorentini, V.; Vanderbilt, D. *Spontaneous Polarization and Piezoelectric Constants of III-V Nitrides*; 1997.

(22)   Takeuchi, T.; Amano, H.; Akasaki, I. Theoretical Study of Orientation Dependence of Piezoelectric Effects in Wurtzite Strained GaInN/GaN Heterostructures and Quantum Wells. *Jpn. J. Appl. Phys.* **2000**, *39* (Part 1, No. 2A), 413–416. https://doi.org/10.1143/jjap.39.413.

(23)   Northrup, J. E. GaN and InGaN (1122) Surfaces: Group-III Adlayers and Indium Incorporation. *Appl. Phys. Lett.* **2009**, *95* (13). https://doi.org/10.1063/1.3240401.

(24)   Wang, T. Topical Review: Development of Overgrown Semi-Polar GaN for High Efficiency Green/Yellow Emission. *Semicond. Sci. Technol.* **2016**, *31* (9). https://doi.org/10.1088/0268-1242/31/9/093003.

(25)   Wang, T. Topical Review: Development of Overgrown Semi-Polar GaN for High Efficiency Green/Yellow Emission. *Semicond. Sci. Technol.* **2016**, *31* (9), 93003.

(26)   Zhao, Y.; Yan, Q.; Huang, C.-Y.; Huang, S.-C.; Shan Hsu, P.; Tanaka, S.; Pan, C.-C.; Kawaguchi, Y.; Fujito, K.; Van de Walle, C. G. Indium Incorporation and Emission Properties of Nonpolar and Semipolar InGaN Quantum Wells. *Appl. Phys. Lett.* **2012**, *100* (20), 201108.

(27)   Koleske, D.; Lee, S. R.; Crawford, M. H.; Coltrin, M. E.; Fini, P. *Semi-Polar GaN Materials Technology for High IQE Green LEDs.*; Sandia National Lab.(SNL-NM), Albuquerque, NM (United States); Inlustra …, 2013.

(28)   Wang, T.; Lee, K. B.; Bai, J.; Parbrook, P. J.; Airey, R. J.; Wang, Q.; Hill, G.; Ranalli, F.; Cullis, A. G. Greatly Improved Performance of 340 Nm Light Emitting Diodes Using a Very Thin GaN Interlayer on a High Temperature AlN Buffer Layer. *Appl. Phys. Lett.* **2006**, *89* (8), 81126.

(29)   Zhang, Y.; Bai, J.; Hou, Y.; Smith, R. M.; Yu, X.; Gong, Y.; Wang, T. Defect Reduction in Overgrown Semi-Polar (11-22) GaN on a Regularly Arrayed Micro-Rod Array Template. *AIP Adv.* **2016**, *6* (2), 25201.

(30)   Bai, J.; Xu, B.; Guzman, F. G.; Xing, K.; Gong, Y.; Hou, Y.; Wang, T. (11-22) Semipolar InGaN Emitters from Green to Amber on Overgrown GaN on Micro-Rod Templates. *Appl. Phys. Lett.* **2015**, *107* (26). https://doi.org/10.1063/1.4939132.

(31)   Shmidt, N. M.; Levinshtein, M.; Rumyantsev, S.; Shur, M. Indium Phosphide (InP). *Handb. Ser. Semicond. Parameters* **1996**, *1*, 169–190.

(32)   Yamanaka, M.; Daimon, H.; Sakuma, E.; Misawa, S.; Yoshida, S. Temperature Dependence of Electrical Properties of N-and P-type 3C-SiC. *J. Appl. Phys.* **1987**, *61* (2), 599–603.

(33)   Logan, R. A.; Peters, A. J. Impurity Effects upon Mobility in Silicon. *J. Appl. Phys.* **1960**, *31* (1), 122–124.

(34)   Willardson, R. K.; Beer, A. C. *Semiconductors and Semimetals*; Academic press, 1977.

(35)   Rubin, M.; Newman, N.; Chan, J. S.; Fu, T. C.; Ross, J. T. P-type Gallium Nitride by Reactive Ion-beam Molecular Beam Epitaxy with Ion Implantation, Diffusion, or Coevaporation of Mg. *Appl. Phys. Lett.* **1994**, *64* (1), 64–66.

Chapter 3: Experimental techniques for VLC

Several experimental techniques are used in this research project to realise light-emitting diodes (LEDs) for visible light communications (VLC) applications, most of which are specific device characterisation methods. The VLC system will be presented from a fundamental basis of light intensity modulation, as it is important for replication of work in this thesis, and complex modulation schemes will be explained. The MATLAB source code for the on-off keying (OOK) and DC-biased optical – orthogonal division frequency multiplexing (DCO-OFDM) schemes along with instrument specific code is provided in the Appendix. Our time-resolved luminescence systems will be explained, along with the electrical and optical excitation methods used to study the recombination dynamics. The inductance, capacitance, and resistance (LCR) system used for capacitance measurements is also described. The VLC system was designed and built by Jack Haggar. The time-resolved electroluminescence system was designed and built by Jack Haggar and Dr Suneal Ghataora. The time-resolved PL system was built by Dr Richard Smith.

3.1   Visible Light Communications (VLC) system

A photograph of our VLC system is shown in Figure 3-2. The system can measure the frequency response of LEDs and apply complex modulation schemes such as DCO-OFDM to exploit bandwidth limited systems such as optoelectronic devices.

3.1.1   Modulation bandwidth

The modulation bandwidth is a measure of the frequency response of a device. It can be quantified as the optical power of an LED subject to a chirped frequency signal falling to half of its initial value. As explained previously, for LEDs the modulation bandwidth is limited by the total carrier recombination lifetime or the resistance-capacitance (RC) time constant for large junction capacitance values under electrical injection. Considering the former case, the alternating current (AC) variation in a LED, i, when subject to a small AC input signal with frequency, ω, is given by

$$i(\omega) = \frac{i_0}{\sqrt{1 + \omega^2 \tau_{diff}^2}},$$

(3-1)

where i_0 is the DC bias and τ_{diff} is the differential carrier lifetime of a LED. A differential carrier lifetime is used here instead of the total carrier recombination lifetime since the LED is subject to a small AC signal, such that the derivative of the recombination rate equation in Equation 2-17 is used. The electrical power dissipated through a resistor is $P = i^2 R$. Therefore, the electrical power variation is proportional to the square of the current variation

i.e., $P_{electrical} \propto i(\omega)^2$. The modulation bandwidth, therefore, is defined as $i(\omega)^2 = \frac{1}{2}i_0{}^2$. Rearranging Equation 3-1 defines the cut-off frequency, f_{3dB} as

$$f_{3dB} = \frac{1}{2\pi\tau_{diff}},\tag{3-2}$$

the 3 dB corresponds to the halving of the electrical power using a logarithmic scale. This is known as the *electrical-to-optical* bandwidth. To measure the frequency response, a photodiode with an integrated transimpedance amplifier (TIA) is typically used and is measured with a vector network analyser (VNA). The photodiode converts the total received power from the LED into a photocurrent. The TIA converts the current into a voltage and amplifies the signal to increase the sensitivity. TIAs are AC coupled such that no light intensity originating from the DC bias is amplified. When the light intensity of the LED drops to the 3 dB point, the generated photocurrent is $i(\omega) = \frac{1}{2}i_0$. The corresponding power in the photodiode is therefore $P = \left(\frac{1}{2}i_0\right)^2 R = \frac{1}{4}i_0{}^2 R$ and the bandwidth becomes $i(\omega)^2 = \frac{1}{4}i_0{}^2$. This is defined as the *electrical-to-optical-to-electrical* bandwidth when measured on the VNA, the power at which the LED drops to a quarter i.e., the 6 dB point of its initial value, due to the photodiode and VNA used for detection. Many reports use this bandwidth definition as a measure of LED performance instead of the *electrical-to-optical* bandwidth commonly used. The equipment schematic for frequency response and VLC measurements is shown in Figure 3-1.
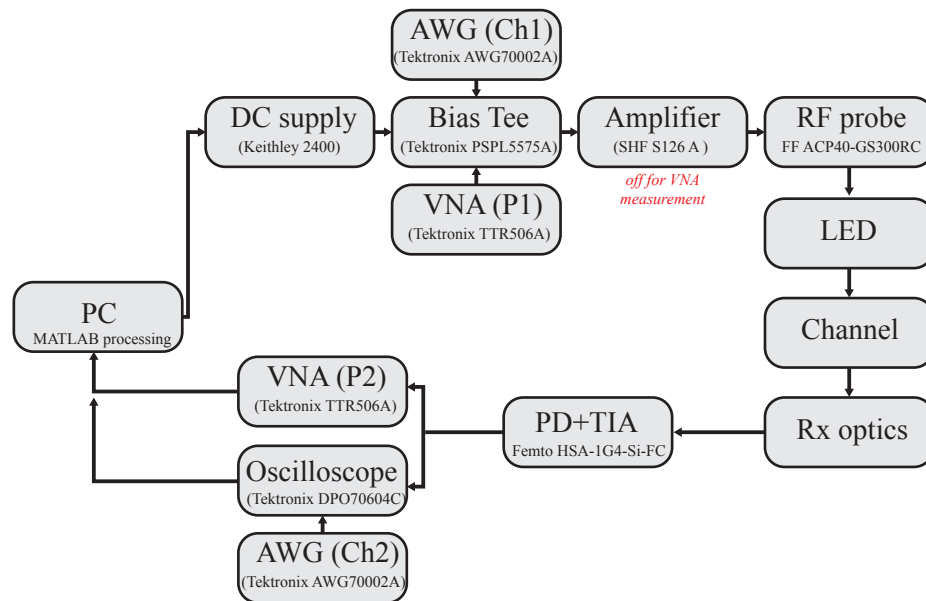
Figure 3-1 Equipment schematic for frequency response and VLC measurements.

VNA software
frequency response
measurement

transmitted
QAM signals

LED sample
view from CCD
for probing

received
QAM signals

(a)

CCD

lens tube for
CCD viewing

collection optics
objective/mirror

Sample stage

magnetic
probe station

arbitrary waveform
generator 10 GHz

digital phospor
oscilloscope 6 GHz

(b)

RF probe

40× 0.75 NA
objective
lens

mirror

translation stage

translation stage

1.4 GHz photoreciever

2-inch aspheric lens

(c)

Figure 3-2 Visible light communications (VLC) system. (a) typical PC output, (b) probe station and RF measurement equipment and (c) SNR optimised collection optics for substrate emission.

3.1.2   Frequency response measurement

The setup used to measure the frequency response is shown in Figure 3-3. Initially, a small signal spanning 6GHz (usually shortened to 1.4GHz, the cut-off of the photoreceiver) from port 1 of a VNA (Tektronix TTR506A) is generated. The signal strengths are typically in the range of 0 dBm to -10 dBm, which corresponds to modulation depths in the 100 mV range assuming the series resistance of the LED is around 50 Ω (which can vary depending on the IV characteristics). The AC signal is combined with a constant current through a 12 GHz bias tee (Tektronix PSPL5575A) and fed into a high-frequency ground-signal (GS) 40 GHz probe (FormFactor ACP40-GS300RC). As shown in Figure 3-3a, all the components apart from the RF probe and DUT are calibrated out of all measurements by connecting short, open, load (50 Ω) and thru reference connections supplied by the VNA.

(a)

(b)

Figure 3-3 Frequency response setup for LED measurements. (a) schematic and (b) annotated photograph.

The LEDs are generally on-wafer, and electroluminescence is collected via the top (through a transparent p-contact) or the transparent sapphire substrate, which can be polished for enhancing light collection efficiency. For the former case, emission is collected using an infinity corrected objective (Mitutoyo 10×, NA = 0.28) and then coupled into a multimode fibre using a parabolic collimator (Thorlabs RC12SMA-P01). In the latter case, since probing

is not obstructive to the LED emission plane, a stronger infinity-corrected objective (Olympus 40×, NA = 0.75) is used which increases the light collection efficiency and therefore the total signal-to-noise ratio (SNR) of the system. Since the frequency response of a device is relative and typically normalised, the collection efficiency is not that important. For smaller, less efficient devices such as microLEDs or SNR sensitive applications like VLC however, maximising the SNR is crucial. A large 2-inch aspheric lens is then used to focus the light onto the photoreceiver (Femto HSA-1G4-Si-FC). The VNA then compares the signal from the photoreceiver to the input signal to generate a frequency response plot.
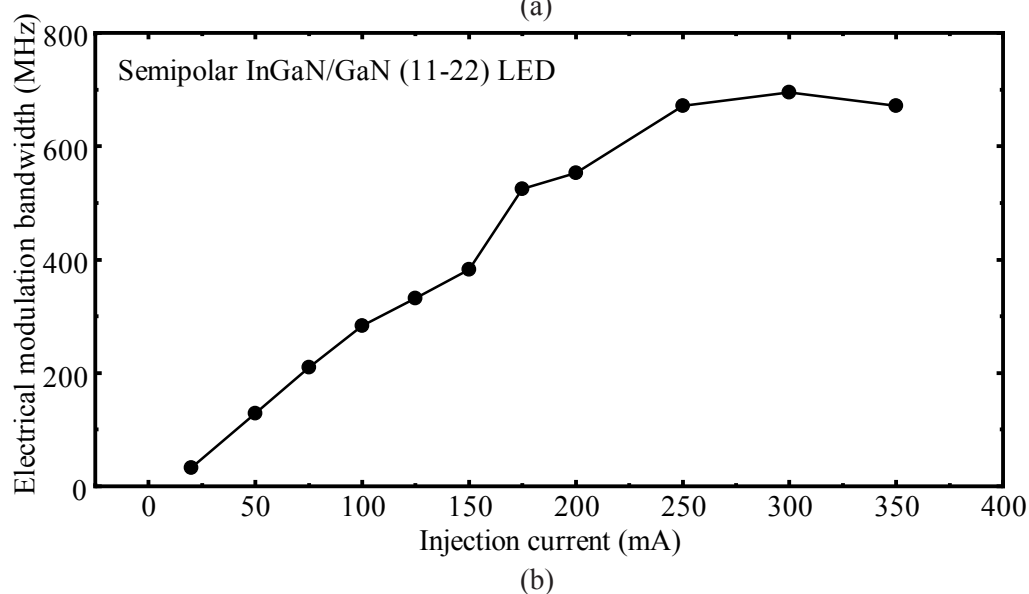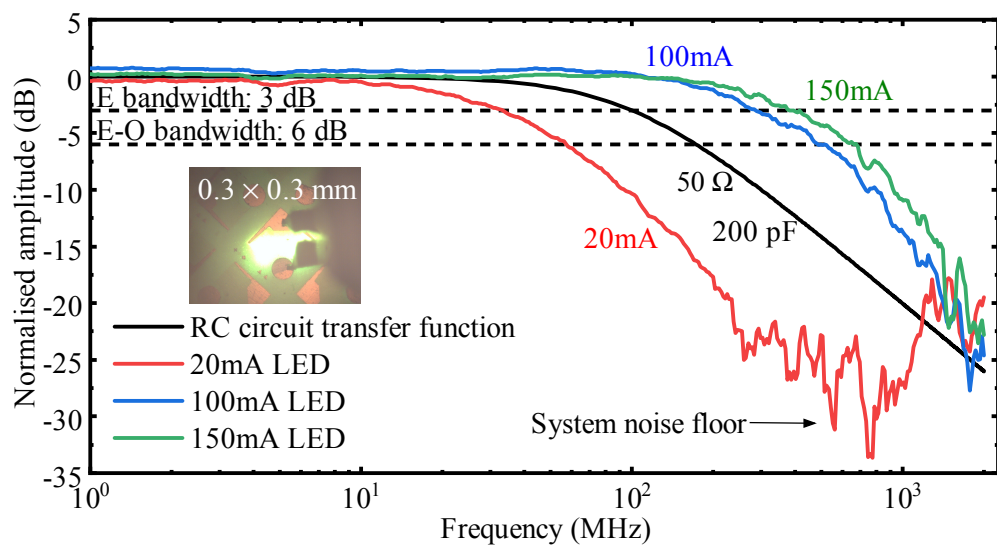
Figure 3-4 (a) Typical Frequency response of an InGaN/GaN semipolar LED (coloured lines) and the simulated frequency response of a low pass filter with R = 50 Ω and C = 200 pF. (b) electrical modulation bandwidth as a function of injection current.

An example of the frequency response of various InGaN/GaN LEDs is shown in Figure 3-4a. The roll-off in frequency is expected due to the speed of the signal generated from the VNA

exceeding the recombination time of the LED. In LEDs driven at higher current densities, however, the gradual decrease in power at higher frequencies can be advantageous by employing complex modulation schemes after the cut-off frequency, essentially increasing the available bandwidth for data transfer. The only concern here is the SNR after the cut-off frequency, which can be optimised through device design or collection optics. Figure 3-4b shows the modulation bandwidth increasing with the applied constant current. As explained in Chapter 1 and 2, this is due to the increased current density in the active region decreasing the total recombination lifetime.

3.1.3   Modulation schemes

There are a number of modulation schemes available for VLC. On a fundamental level, optical wireless communications (OWC) data is sent through a transmitter using streams of '1s' and '0s' which, in the analogue domain, consists of discrete voltage levels provided by a waveform generator. The waveform modulates the transmitter's light intensity which travels through a OWC channel, introducing various distortions and delays before reaching the receiver. The recovered signal is compared with the input signal by strictly looking at where '1s' and '0s' should be which is then presented as errors in the form of a bit-error-ratio (BER). The BER is a crucial characteristic which represents the quality of signal recovered at the receiver. The Forward Error Correction (FEC) is a standard dictating the maximum BER of 3.8×10^{-3} for a successful communication link.

More specifically to optoelectronics such as LEDs, the modulation schemes must consider certain operating conditions such as turn-on voltage, series resistance, and output power as it can be detrimental to BER. The modulation waveform therefore needs to be bipolar, in that the signals must exist above and below a threshold, which in this case is the constant current supplied from the power source to bias the LED. The bias is needed to ensure the negative parts of the modulated waveform are utilised in the output of the LED. Care must be taken when modulating the LED as clipping and distortion can occur to the resulting waveform around the turn-on voltage and thermal roll-off regions. For this reason, modulation schemes should be targeted towards the linear regime of the LED's IV characteristics. Two modulation schemes of interest are used in this work: OOK and DCO-OFDM. OOK is used as a precursor for higher level modulation formats such as DCO-OFDM in this case as eye-diagrams give a lot of information and diagnostics on a OWC link whilst being relatively simple to implement.

OOK

OOK is a single carrier baseband modulation scheme where the transmitted waveform consists of a pseudorandom bit sequence (PRBS). '1s' and '0s' are encoded as the bit

sequence is present or absent, respectively. The PRBS serves to modulate the LED's light intensity which can be represented in an eye-diagram, overlaying all the possible bit transitions in a sequence. The experimental setup for OOK data transmission is similar to the frequency response setup, however a 10 GHz arbitrary waveform generator (Tektronix AWG70002A) and 6 GHz digital phosphor oscilloscope (Tektronix DPO70604C) are used for the PRBS generation and receiver hardware, respectively. A variable gain amplifier is used to match the output modulation depth from the AWG to the LEDs dynamic range. A typical transmitted and received PRBS-7 (2^7-1 bits long) signal is shown in Figure 3-5a, along with the experimental setup and corresponding eye-diagram at 1Gb/s in Figure 3-5b and Figure 3-5c, respectively. As the data transmission rate increases, the eye tends to close as the system approaches the modulation bandwidth of the LED and the SNR decreases.
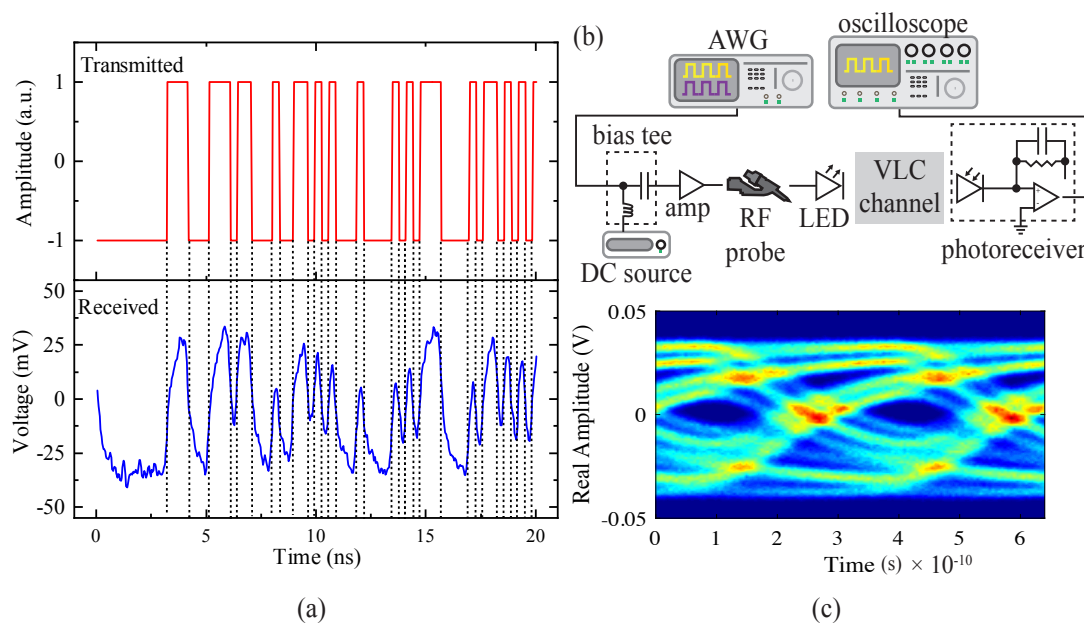
Figure 3-5 VLC setup for OOK modulation. (a) Typical transmitted and received waveforms of a 1Gb/s PRBS-7 from a semipolar LED. (b) VLC schematic of experimental setup and (c) resulting eye diagram of the received signal.

DCO-OFDM

A higher order, multi-carrier modulation scheme known as OFDM is very useful in dynamic range and bandwidth limited systems such as LEDs. The reason being that this particular scheme can adapt to the device under test excellently. The roll-off associated with the frequency response of the LEDs can be exploited by using adaptive frequency domain modulation formats such as OFDM. A simple schematic of OFDM is given in Figure 3-6. At its core, OFDM is realised using closely spaced subcarriers with orthogonality in the frequency domain. Orthogonality is realised when subcarriers are separated such that they only partially overlap, with the peak of one subcarrier coinciding with the zero-crossing of its neighbouring subcarrier. The subcarriers are then considered to be orthogonal to each

other when crosstalk is eliminated. Each subcarrier is modulated with a fixed quadrature amplitude modulation (QAM) order, for example, 4-QAM containing 2 bits per symbol. QAM consists of two carrier waves, one 90° out of phase with the other which groups the incoming bit stream and assigns different amplitudes and phases of the two carrier waves to each possible bit configuration. The resulting modulated signal can be expressed as a constellation diagram, with each point corresponding to a different amplitude and phase coordinate. The modulation order, M is defined by 2^n, where n is the group of bits being modulated. Increasing the M-QAM order to higher levels increases the spectral efficiency ((bit/s)/Hz) of the available channel, and therefore the data throughput can be increased dramatically compared with the OOK method described above. The higher data throughput results in a degraded BER since the QAM constellation points are spaced closer together and is limited by the noise associated with the channel. The experimental setup for DCO-OFDM is the same setup as used for OOK, the difference is in the pre and post processing methods to generate the OFDM waveform in MATLAB.
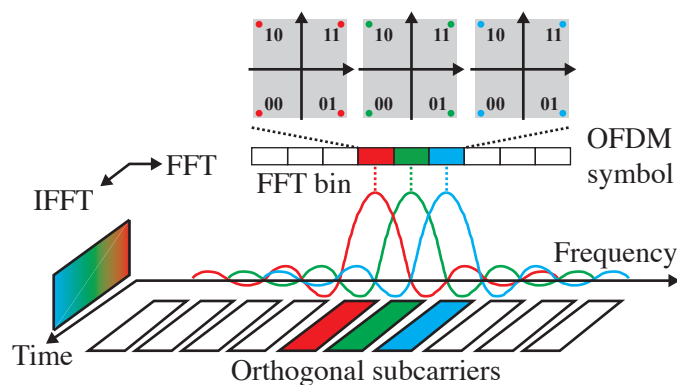
Figure 3-6 OFDM waveform visualised in the frequency and time domain consisting of multiple QAM constellations situated on closely spaced subcarriers.

The DCO-OFDM scheme discussed above utilises a fixed M-QAM order for data transmission. From this, we can measure the SNR per subcarrier from the response of the signal, effectively measuring the frequency response of the entire system i.e., the OWC channel response. From this, we can adaptively load each subcarrier with a different M-QAM order to increase the spectral efficiency. Figure 3-7 shows a typical LED DCO-OFDM input and output power spectrum, and the associated adaptively loaded QAM constellations based on SNR at different subcarriers. For more discussion on OFDM and VLC encoding techniques in general, please refer to [1-6]. More experimental detail specific to semipolar LEDs is found in Chapter 5.
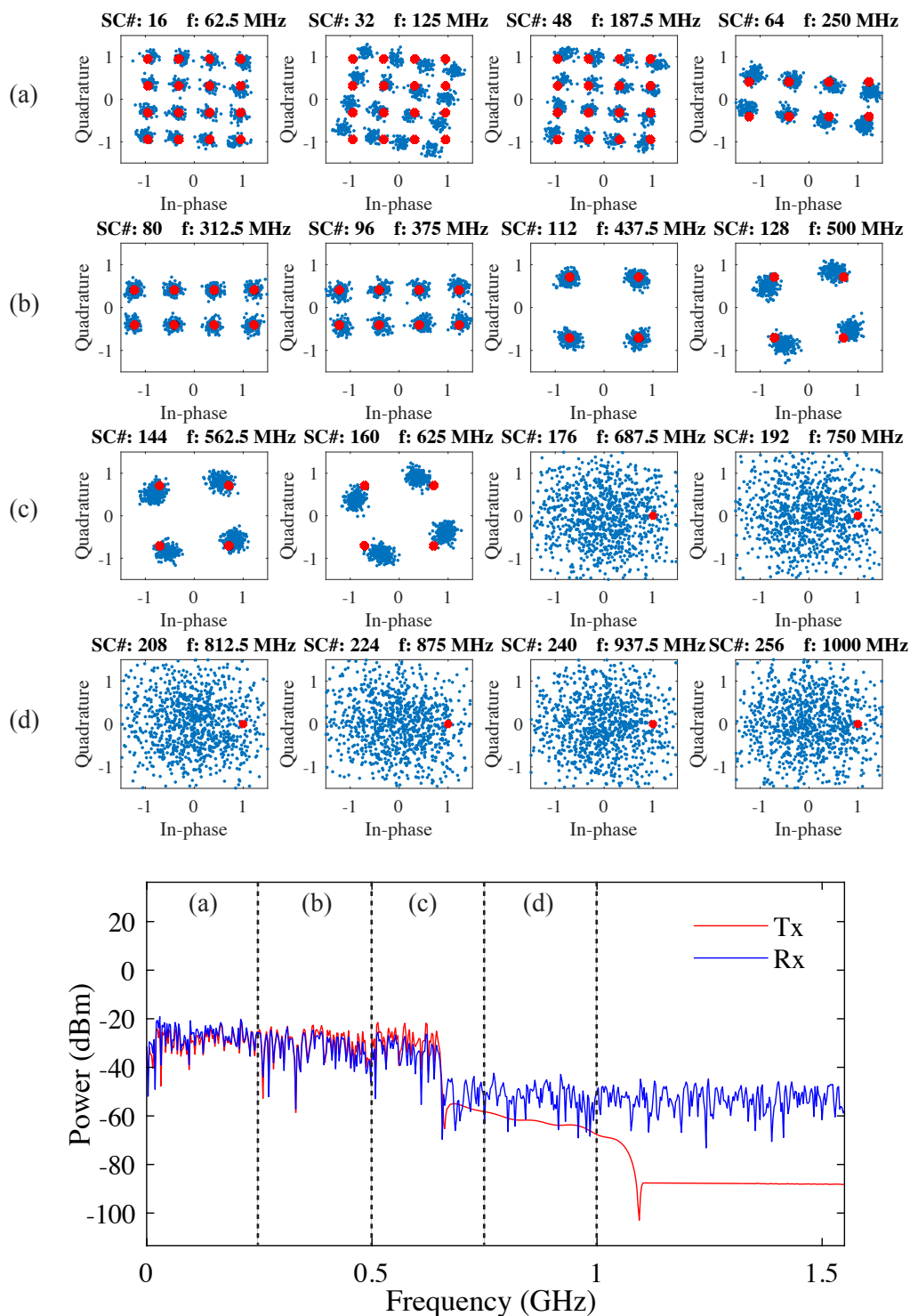
Figure 3-7 Typical QAM constellations of different subcarriers (top) extracted from the received (blue) unequalised OFDM power spectrum of a semipolar LED (bottom) and transmitted data (red). Higher frequencies (above 686.5 MHz) correspond to unmodulated subcarriers for improved BER. The total data rate in this case is 1.76 Gb/s.

3.2   Time-resolved luminescence

Time-resolved luminescence spectroscopy involves the measurements of the temporal luminescent decay of a semiconductor subject to an excitation source, i.e., under either optical pumping or electronic excitation. In doing so, the fundamental physics of carrier behaviours can be measured within a sample. This allows for a more detailed analysis of the sample, measuring parameters such as the non-radiative and radiative recombination lifetimes of carriers as a function of temperature by fitting an appropriate decay model. As the luminescent decay of a sample occurs on the order of nanoseconds or less, specialised equipment is needed to accurately resolve the signal. This is achieved using a method called time-correlating single photon counting (TCPSC).

Time correlated single photon counting (TCSPC)

TCSPC operates using a periodic excitation from a source, for example, a pulsed laser or an electronic square wave. Data can then be sampled over multiple excitation and emission events using a single photon detector such as a photo-multiplier tube (PMT). The collected photons from thousands of events can then be reconstructed into a decay profile using precisely timed registration and allocation of photons into individual timing bins[7,8].

A simplified process of TCSPC is described as follows: An excitation source is generated, at the same time, a trigger signal is sent to a timing electronics synchronisation module. The sample is excited, and the emission is collected via a PMT where a photon is detected. This generates a voltage signal which is sent to the same timing electronics module. The difference in the trigger signal and detector signal is logged in memory. A histogram of photon events is then produced over many trigger and detection cycles, analogous to an intensity plot as a function of time. To make the technique as accurate as possible, the probability of multiple photon detection between adjacent pulses needs to be negligible. This is achieved by limiting the detection rate of the PMT between 1-5% of the excitation source repetition rate. Another important consideration in TCSPC systems is the instrument response function (IRF). The IRF is a convolution of all timing jitters present in a system, originating from the cables and equipment. Therefore, when measuring the luminescence decay of a sample, the IRF would be an intrinsic part of the response. It is therefore necessary to either deconvolve and remove the IRF from the decay profile or ensure that it is not a deciding factor in the extracted lifetime parameters. Deconvolving the IRF from the response directly is quite difficult, the accepted solution is to use an iterative re-convolution fitting method. The Fluofit software from PicoQuant is used to do this for our time-resolved photoluminescence setup (TRPL). The weakest part of the IRF, that is, the piece of equipment that contributes the most to the IRF is usually the detector. We can approximately estimate the IRF response using the sum-of

the squares of the full-width at half maximum (FWHM) responses of each piece of equipment in the system

$$e_{IRF} = \sqrt{\sum e_{equipment}^2}.$$

(3-3)

Due to the nature of the calculation, e_{IRF} will be proportionally more skewed towards the slowest part of the system, in this case, the detector rendering the other component's contributions negligible.

3.2.1   Photoluminescence

Our TRPL system is shown in Figure 3-8. A pulsed 375 nm laser (PicoQuant PDL 800-B) is used to directly excite InGaN/GaN quantum well structures. The laser has characteristics of 50 ps pulse width and a variable repetition rate of 2.5 – 40 MHz, which integrates with the TCSPC electronics module (Becker & Hickl Simple-Tau 130). The laser excites the sample through a dichroic mirror and a high magnification objective (Mitutoyo 50×, NA = 0.42) with a micron-scale spot size. The emission from the sample is then collected through the same microscope objective and reflected from the dichroic mirror to be dispersed through diffraction grating on a monochromator (Horiba Jobin Yvon iHR550) before being focused onto a hybrid-PMT with an integrated pre-amplifier (Becker & Hickl HPM-100- 40 with a Hamamatsu R10467). The PMT detects a photon down to a response time of 120 ps. As a result, the IRF of the system is calculated to be 150 ps, which is removed from each measurement. The system has a timing resolution of 15 ps.
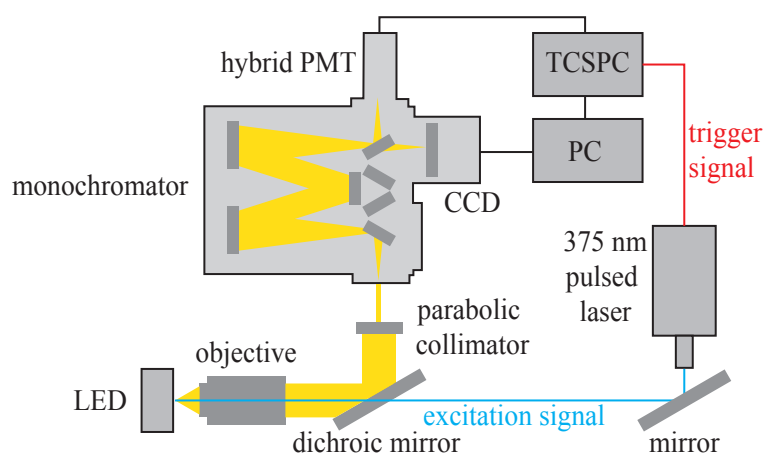
Figure 3-8 Time-resolved photoluminescence (TRPL) setup.

3.2.2   Electroluminescence

Our time-resolved electroluminescence (TREL) system is shown in Figure 3-9. The TREL and VLC systems share components such as the AWG, bias tee, RF probe and oscilloscope. An electrical square wave with an ultrafast falling edge (around 23 ps) is generated from our

AWG and used as an excitation source. The trigger signal, which is identical to the excitation signal operating at the same clock frequency is created on the adjacent AWG channel for the timing electronics module. A bias tee is used to combine the excitation source and a constant current from a power supply (Keithley 2400). Our RF probe then delivers the signal to excite the sample and the resulting electroluminescence is collected through a microscope objective (Mitutoyo 50×, NA = 0.42) which is infinity corrected. A 50:50 beam splitter is used to direct half of the emission to be coupled into a fibre using a parabolic collimator. Like TRPL, the light is dispersed through a monochromator and onto a hybrid PMT and the resulting photon detection triggers the TCSPC module, and a histogram of electroluminescence is created over multiple excitation and emission events. The hybrid PMT used in this case (PicoQuant PMA Hybrid Series – 06) has a faster response than in TRPL, resulting in an estimated system IRF of 67 ps. Comparisons between the TRPL and TREL excitation methods along with the advantages for VLC are given in detail in Chapter 6.
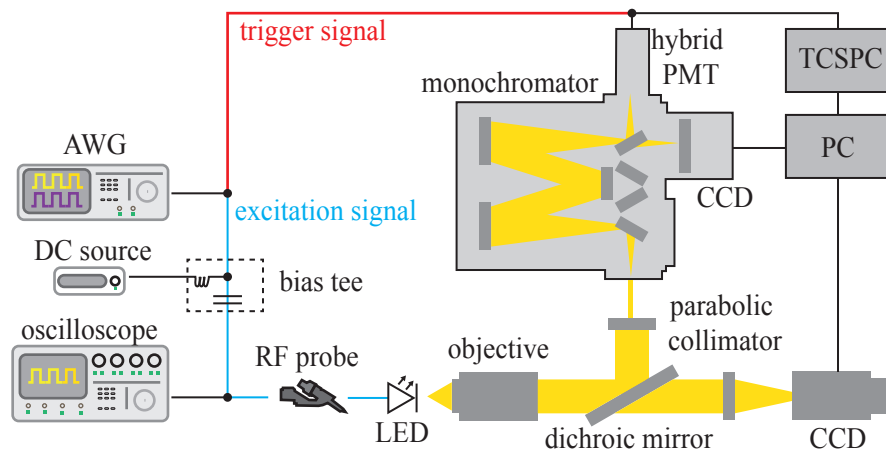
Figure 3-9 Time-resolved electroluminescence (TREL) setup.

3.3   Precision inductance, capacitance, and resistance (LCR) system

As the junction capacitance of a LED influences the modulation bandwidth, a precise measurement of the capacitance as a function of voltage is necessary for VLC applications. In principle, the LCR meter generates an AC signal and measures the current, *I,* through and voltage, *V,* across a device and measures the phase angle between them to determine the impedance. From the impedance, we can calculate L, C and R. Our system uses a precision LCR meter (Keysight E4980A Precision LCR Meter, 20 Hz to 2 MHz) to measure the capacitance of LEDs. The system is calibrated such the cables and the system phase response is accounted for, leaving the measured values of L, C and R characteristic of the device itself.

3.4 References

(1) Rajbhandari, S.; McKendry, J. J. D.; Herrnsdorf, J.; Chun, H.; Faulkner, G.; Haas, H.; Watson, I. M.; O'Brien, D.; Dawson, M. D. A Review of Gallium Nitride LEDs for Multi-Gigabit-per-Second Visible Light Data Communications. *Semicond. Sci. Technol.* **2017**, *32* (2), 023001.

(2) Sufyan Islim, M.; Ferreira, R. X.; He, X.; Xie, E.; Videv, S.; Viola, S.; Watson, S.; Bamiedakis, N.; Penty, R. V; White, I. H.; Kelly, A. E.; Gu, E.; Haas, H.; Dawson, M. D. Towards 10 Gb/s Orthogonal Frequency Division Multiplexing-Based Visible Light Communication Using a GaN Violet Micro-LED. **2017**.

(3) O'Brien, D.; Rajbhandari, S.; Chun, H. Transmitter and Receiver Technologies for Optical Wireless. *Philos. Trans. R. Soc. A Math. Phys. Eng. Sci.* **2020**, *378* (2169).

(4) Lowery, A. J. Spectrally Efficient Optical Orthogonal Frequency Division Multiplexing. *Philos. Trans. R. Soc. A Math. Phys. Eng. Sci.* **2020**, *378* (2169).

(5) Haas, H.; Elmirghani, J.; White, I.; Haas, H. Optical Wireless Communication Subject Areas : Author for Correspondence : **2020**.

(6) Tsonev, D.; Chun, H.; Rajbhandari, S.; Mckendry, J. J. D.; Videv, S.; Gu, E.; Haji, M.; Watson, S.; Kelly, A. E.; Faulkner, G.; Dawson, M. D.; Haas, H.; O'brien, D. A 3-Gb/s Single-LED OFDM-Based Wireless VLC Link Using a Gallium Nitride MLED. *IEEE PHOTONICS Technol. Lett.* **2014**, *26* (7).

(7) O'Connor, D. *Time-Correlated Single Photon Counting*; Academic press, **2012**.

(8) Lakowicz, J. R. *Principles of Fluorescence Spectroscopy*; Springer, **2006**.

Chapter 4: High Modulation Bandwidth of Semipolar (11-22) InGaN/GaN LEDs with Long Wavelength Emission

Visible light communications (VLC) requires III-nitride light emitting diodes (LEDs) with high modulation bandwidth but suffer from various c-plane limitations as explained in Chapter 2. In addition, white light illumination requires green/yellow III-nitride LEDs with high efficiency but are very difficult to achieve on *c-plane* substrates. Other LED structures, for example, microLEDs with low efficiency can be used to obtain high modulation bandwidths but do not satisfy the requirement for standalone general illumination. In this chapter, we demonstrate a record modulation bandwidth of 540 MHz for semipolar green LEDs with the additional capability of general illumination due to their broad area. Semipolar yellow and amber LEDs with modulation bandwidths of 350 and 140 MHz, respectively, have also been reported. These results agree with differential carrier lifetime measurements.

4.1   Introduction

Since the 1990s, there has been unprecedented progress in developing solid state lighting (SSL) sources, which are overwhelmingly dominated by III-nitride semiconductor LEDs. Much like the evolution from traditional telephones to smartphones, it is anticipated that the development of SSL sources will undergo a similar trend from current devices with a single function to future devices with multiple functions. A smart lighting source, for example, can be used as a transmitter for VLC (i.e., Li- Fi)[1,2] along with its original function for general illumination.

So far, a "blue LED + yellow phosphor" approach still remains the dominant technique in manufacturing white LEDs, where white lighting is generated by mixing the blue emission of InGaN/GaN LEDs and the downconversion yellow emission from yellow phosphors radiatively pumped by the blue LEDs. However, this approach has a number of fundamental challenges such as limited efficiency, severe colour rendering, and instability issues as a result of employing the downconversion phosphors. The even greater concern is due to the phosphors with an intrinsically slow response time on the scale of microseconds, meaning that the resultant bandwidth is limited to be less than 1 MHz[2–4]. Therefore, the ultimate white LED for VLC is possibly a package of either three individual LED chips containing red, green, and blue (i.e., RGB) emissions or at least two LEDs each emitting blue and yellow. High efficiency blue LEDs have been widely commercialized, but one of the remaining challenges is still the optical performance of green and yellow LEDs, the longer emission wavelength emissions, which is far from satisfactory.

In addition to the issues of the downconversion yellow phosphors in current white LEDs for Li-Fi applications, another fundamental issue for Li-Fi applications is due to blue LEDs themselves. Simply speaking, a maximum modulation bandwidth (f_{3dB}) is inversely proportional to the total carrier recombination lifetime (τ_{total}) of an LED by $f_{3dB} \propto 1/\tau_{total}$. Current blue LEDs that are commercially available are grown on *c-plane* sapphire substrates, intrinsically producing piezoelectric fields as a result of the strain generated by the large lattice mismatch between InGaN and GaN. Consequently, the LEDs exhibit a reduction in the overlap of the electron and hole wave functions leading to an increased radiative recombination lifetime of 10−100 ns, reduced quantum efficiency, and other issues such as efficiency droop[5,6]. Therefore, a maximum attainable modulation bandwidth is in principle on the order of MHz if any extra methods are not used (for example, using microLEDs, which will be explained later), which is far from the practical requirements for Li-Fi. In order to enhance the modulation bandwidth when using current blue LEDs for Li-Fi, complicated modulation techniques with pre- and post-equalization and a large amount of postprocessing have to be employed, making the communication system complicated and expensive[7–10]. Even so, the modulation bandwidth is still far from satisfactory, as it is fundamentally determined by the long radiative recombination lifetime of blue LEDs on c-*plane* substrates, which is limited by their intrinsic polarization. This increases concerns when LEDs move toward longer emission wavelengths such as green or yellow, which require higher indium content leading to further enhancement in strain-induced piezoelectric fields. Recently, it has been proposed to employ microLEDs driven at a very high current density to achieve a high modulation bandwidth for Li- Fi applications[11–14]. However, the great challenge is that the optical efficiency of current microLEDs is too low as a result of significantly enhanced nonradiative recombination[15–17].Therefore, this cannot meet the requirements for both Li-Fi and general illumination simultaneously.

One of the most promising approaches to overcoming the intrinsic polarization is to grow LEDs along a nonpolar or semipolar orientation. In terms of effectively reducing the intrinsic polarization, nonpolar LEDs would be best. However, InGaN intrinsically suffers limited indium incorporation efficiency if it is grown on nonpolar GaN, meaning that it is extremely challenging to grow nonpolar LEDs with green or yellow or any other longer wavelength emissions[18–22]. In contrast, indium atoms can be accommodated on a semipolar GaN surface more easily than those on either a *c-plane* surface or nonpolar surface[20], making semipolar GaN more attractive for obtaining longer wavelength LEDs, which require higher indium content. Out of all the semipolar orientations, (11$\bar{2}$2) GaN is possibly the best choice when considering all factors including high indium content InGaN, a reduction in strain-induced piezoelectric fields, and a short carrier recombination lifetime (by referring to a topical

review for the details about III-nitride semipolar LEDs[21]). This makes ($11\bar{2}2$) semipolar LEDs strong candidates for achieving longer wavelength LEDs for high-speed applications. It is therefore interesting to explore the upper limit in the maximum modulation bandwidth of semipolar LEDs with green, yellow or any other longer wavelength emissions and beyond for which there are no reports so far. Prior to starting the investigation, the crystal quality of semipolar ($11\bar{2}2$) GaN on the more widely used sapphire substrate needs to be improved to a point where it is similar to or at least approaching its *c-plane* counterpart. In order to meet the material challenges, our group has established a number of cost-effective approaches to achieve high quality semipolar ($11\bar{2}2$) GaN grown on *m-plane* sapphire, leading to the demonstration of high performance semipolar InGaN LEDs covering a wide wavelength range up to amber[22].

In this work, frequency response measurements have been performed on semipolar ($11\bar{2}2$) LEDs with long emission wavelengths from green to amber demonstrating a modulation bandwidth of up to 540 MHz for green LEDs with a typical size of $330 \times 330~\mu m^2$, a record modulation bandwidth for III- nitride macroLEDs (not microLEDs) reported so far. This work also presents the first report on the modulation bandwidth of III-nitride based yellow and amber LEDs and is also the record for the longest wavelength III-nitride LED achieved.

4.2   Fabrication

Three different LEDs each containing an InGaN single quantum well (SQW) with different InN mole fractions were prepared on our overgrown semipolar ($11\bar{2}2$) GaN by metal organic chemical vapour deposition (MOCVD). Our detailed structural characterization including both X-ray diffraction and transmission electron microscopy measurements confirm that our overgrown semipolar ($11\bar{2}2$) GaN templates typically exhibit a dislocation density of 2×10^8 /cm², which has been achieved using our mature overgrowth approach on regularly arrayed microrod templates. The crystal quality is even better than that of standard *c-plane* GaN on sapphire for the growth of *c-plane* LEDs. All three LEDs exhibit a similar structure except for in the indium content of their InGaN quantum well. These three LEDs are labelled as LED-A, LED-B, and LED-C, respectively, corresponding to the green LED at 515 nm, the yellow LED at 550 nm, and the amber LED at 610 nm. Detailed information about the growth of these three LEDs is available elsewhere[22–24]. A structural cross-section of our LEDs is shown in Figure 4-1. Using a photolithography technique and then a dry-etching process, LEDs with typical dimensions of $330 \times 330~\mu m^2$ have been fabricated. A transparent p-contact consisting of a 100 nm thick ITO film was deposited using an electron beam deposition technique and then annealed by rapid thermal annealing (RTA). A Ti/Al/Ti/Au

metal stack was then evaporated onto the n-GaN to form an n-contact. Ti/ Au was finally prepared on both the p- and n- contacts to form the n- and p-electrode pads.
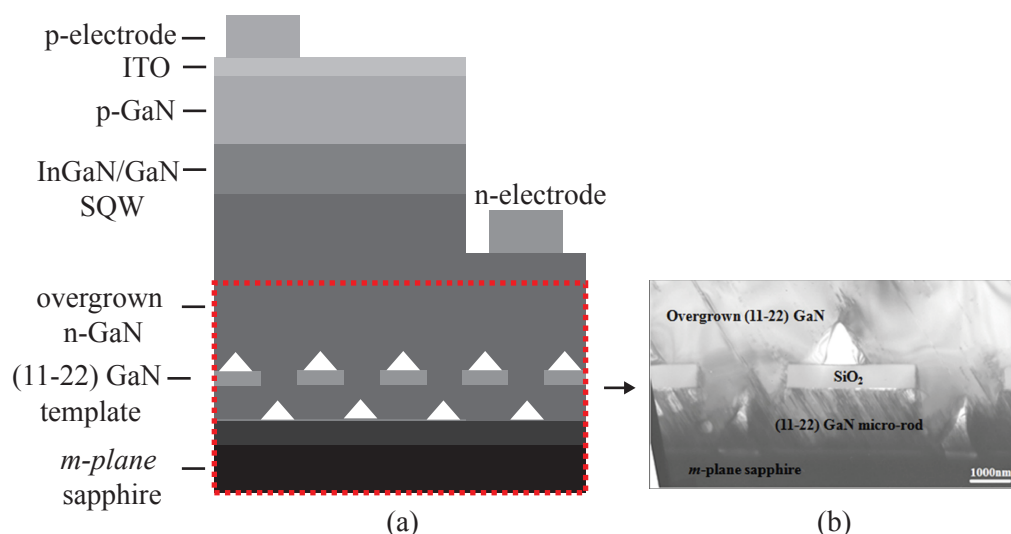
Figure 4-1 Structural cross-section of our single InGaN/GaN quantum well (11$\bar{2}$2) semipolar LEDs (a) and an SEM image of the micro-rod GaN template enabling efficient, long wavelength emitters (b)[22].

4.3   Results and discussion

4.3.1   Electrical and optical characteristics

The IV characteristics of each LED is shown in Figure 4-2a. Turn on voltages (measured at 20 mA) are measured to be 3.7 V, 3.6 V and 5.2 V for LED-A, LED-B and LED-C respectively. The devices do not experience any thermal roll-off in the measurement range for this study (up to 100 mA). Figure 4-2b shows the typical electroluminescence (EL) spectra of the three LEDs measured at a 20 mA injection current in a continuous wave (CW) mode at room temperature, demonstrating strong EL emission centred at 515, 550, and 610 nm for LED-A, LED-B, and LED-C, respectively. Insets shows the EL emission images of these three LEDs taken at an injection current of 20 mA. The higher turn-on voltage for LED-C is due to a poorer p-type activation than the other LEDs, resulting in a lower conductivity and a lower EL peak intensity at the same current density as LED-A and LED-B. The broader full width at half maximum (FWHM) and apparent shoulder on the longer wavelength side of the LED-C EL peak may be due to an indium segregation as a result of the higher indium content than LED-A and LED-B which induces localised, lower energy states available to carriers[22].
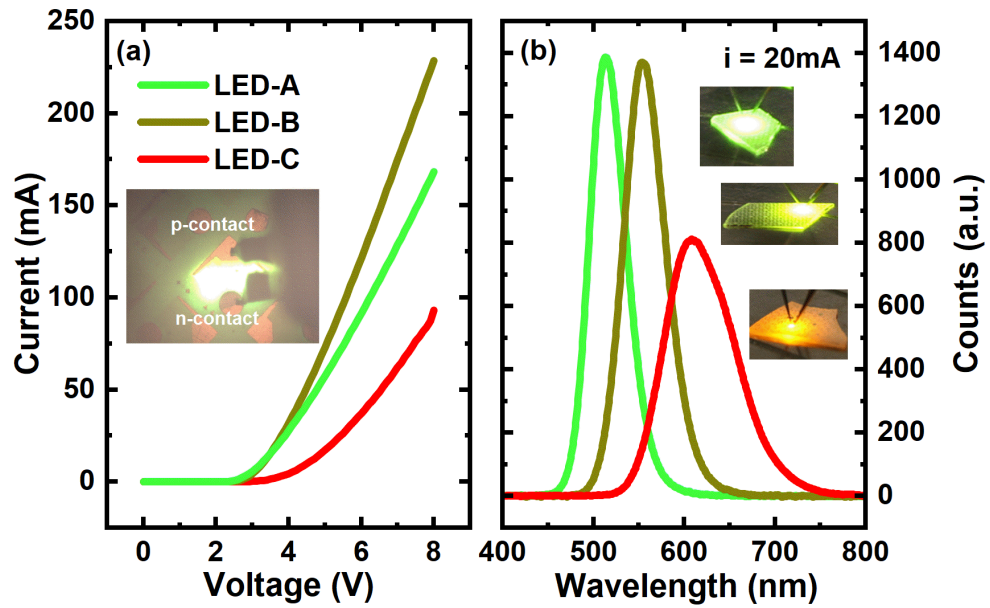
Figure 4-2 IV measurements tested over an 8 V range, inset shows top-down view of LED-B from the charge coupled device (CCD) camera highlighting probing pads (a) and received spectra when biased at 20 mA with the inset showing photographs for LED-A, LED-B and LED-C (b).

4.3.2   Frequency response

A standard system has been used to perform modulation bandwidth measurements on these LEDs. To measure the frequency response, a DC bias from a source meter (Keithley 2612B) was added to a bias tee (Tektronix PSPL5575A) along with a small sinusoidal signal with an amplitude of 100 mV from port 1 of a vector network analyser (VNA, Tektronix TTR506A). The combined signal was sent to our RF probe station equipped with a DC to a 40 GHz signal-ground RF probe (FormFactor ACP40-GS300RC). The EL was collected using an infinity corrected objective (10×, NA = 0.28) and then coupled into a multimode fibre using a parabolic collimator (Thorlabs RC12SMA-P01). A photoreceiver (Femto HSA-1G4-Si-FC) consisting of a silicon photodiode with an integrated transimpedance amplifier was used for optical to electrical conversion and the amplified electrical signal was sent to port 2 of the network analyser. The RF cables and bias tee were also accounted for in the calibration of the S_{21} transmission. The photoreceiver has a 3 dB modulation bandwidth of 1.4 GHz, and our RF probes are designed for 40 GHz testing, ensuring that the frequency response of our devices is not limited by the system response. Figure 4-3 shows the frequency responses of our three LEDs, namely, the normalized output power as a function of frequency for the three LEDs measured under identical conditions. The frequency response measurements have also been carried out as a function of injection current density ranging from 9.2 to 92 A/cm², which cover the major range for practical applications. The normalized power is obtained by taking the initial frequency point (100 kHz) as 0 dB.
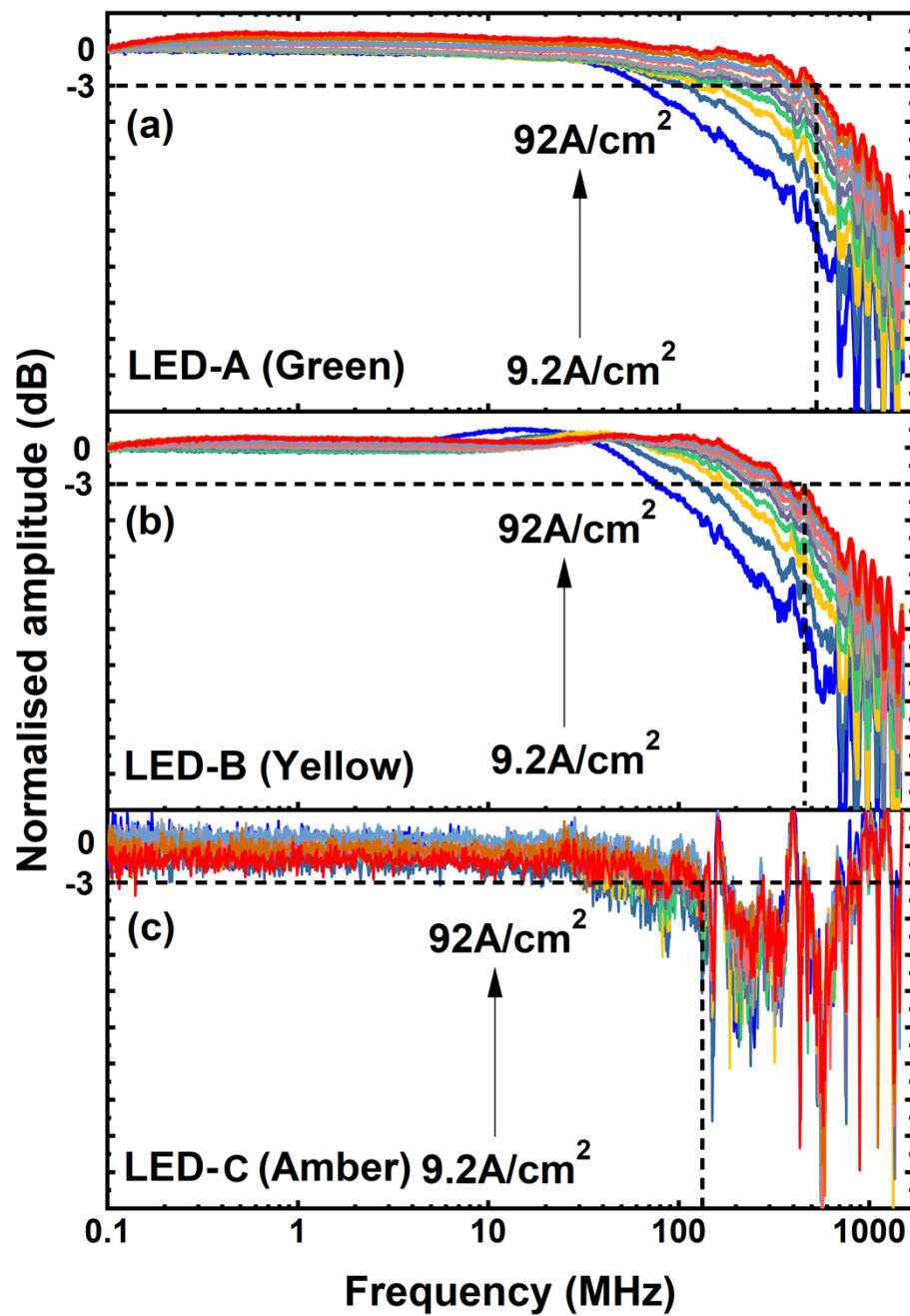
Figure 4-3 Figure 4 3 Frequency responses of LED-A (a), LED-B (b) and LED-C (c) measured between 10-100mA. The horizontal dashed line denotes the 3 dB bandwidth.

All the devices demonstrate a maximum 3 dB modulation bandwidth exceeding 100 MHz when driven at a higher current density. For example, LED-A shows a 3 dB modulation bandwidth of 540 MHz at 92 A/cm^2, which is the highest reported on III-nitride LEDs with a standard area of 330 × 330 μm^2 or above (not microLEDs) for general illumination. LED-B and LED-C exhibit a maximum 3 dB modulation bandwidth of 350 and 140 MHz, both of which are the first report in the yellow and amber regions. The small "shoulder" around 20 MHz apparent on the yellow LED may be due to the relaxation resonant frequency often observed in laser diodes[25], but in LEDs, this needs further study. Small fluctuations at higher frequencies (before the noise floor of the VNA) are from signal reflections within our testing system. It is worth highlighting that there still exists piezoelectric polarization in semipolar LEDs, although the polarization in semipolar LEDs is substantially weaker compared with that of their *c-plane* counterparts as stated above. Longer wavelength LEDs require higher indium content, leading to an increase in piezoelectric polarization and thus a reduced quantum efficiency. Consequently, the SNR decreases with increasing emission wavelength. This is why the amber LED signal is noisy compared with other LEDs.

Figure 4-4a displays the 3 dB modulation bandwidth as a function of injection current density from 9.2 to 92 A/cm^2 for the three LEDs. During the frequency response measurements at each injection current density, the EL spectra of the three LEDs have been measured simultaneously, and Figure 4-4a also provides their corresponding emission wavelengths. For LED-A, the emission wavelength shows a slight blue-shift with increasing injection current density as a result of the screening effect of polarization-induced electrical fields. LED-B exhibits a slightly enhanced blue-shift in emission wavelength with increasing injection current density compared to LED-A. However, it is worth highlighting that the blue-shift in emission wavelength is much smaller than that of their *c-plane* counterparts as a result of the intrinsically low polarization of semipolar LEDs. LED-C initially exhibits a large blue-shift in emission wavelength at low injection current densities as a result of band-filling of localized states[22], and then, the blue- shift reduces quickly but is still larger than those for LED-A and LED-B. LED-C exhibits amber emission at 596 nm even under 92 A/cm^2 and red emission at 620 nm under 9.2 A/cm^2. Therefore, our LEDs have demonstrated a high frequency response in a wide spectral region, which has not been previously reported.
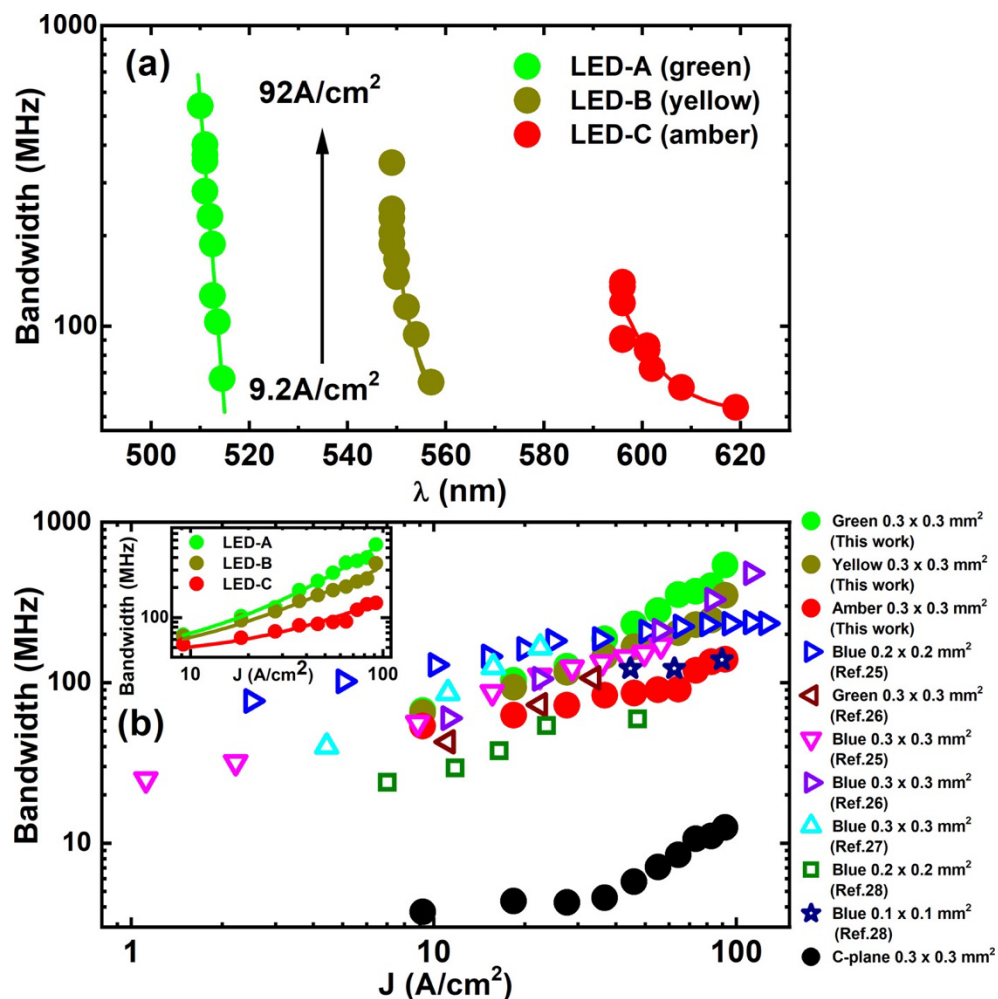
Figure 4-4 (a) Modulation bandwidth (3 dB) as a function of injection current density from 9.2 to 92 A/cm^2 and the corresponding emission wavelength for each injection current density for the three LEDs. (b) Benchmarking our device performance against current state-of-the-art data from semipolar macro-LEDs (>100 × 100 μm^2) in terms of the 3 dB modulation bandwidth. Our data obtained in this work are exhibited by solid symbols, while data collected from the literature are presented as open symbols with different colours. The inset only includes our data from LED-A, LED-B, and LED-C.

Figure 4-4b benchmarks our device performance against the current state-of-the-art semipolar macroLEDs ($>100 \times 100$ μm^2) in terms of the 3 dB modulation bandwidth[26–29]. The inset includes only our data from LED-A, LED-B, and LED-C, provided to make them easier to observe. In the current literature, there has been an entire absence of data from longer emission wavelengths such as yellow and amber LEDs, and thus, the majority of devices reported on so far are blue LEDs whose emission wavelength is below 500 nm. One of the major reasons is due to it being extremely challenging to obtain III- nitride based yellow and amber LEDs with reasonably good device performance. Our data obtained in this work are all labelled by solid symbols in Figure 4-4b, while all the data from literature are presented by using open symbols. A conventional c-plane blue LED with a standard size of 330×330 μm^2 measured under identical conditions has also been provided as a reference. As expected, the *c-plane* blue LED (where 2.5 nm InGaN quantum wells are typically used as an active region) exhibits a low 3 dB modulation bandwidth of 4 MHz at a 9.2 A/cm^2 current density and 12.5 MHz at 92 A/cm^2. The inset in Figure 4-4b shows that the green LED (i.e., LED-A) exhibits the highest 3 dB bandwidth of 540 MHz at 92 A/ cm^2, which is much larger than that of its *c-plane* blue counterpart. This is followed by the yellow LED at 350 MHz and then the amber LED at 140 MHz, also higher than that of the *c-plane* blue counterpart, although the indium content in any *c-plane* blue LED is much lower than those of LED-A−C.

This demonstrates the major advantage of semipolar LEDs, which exhibit intrinsically weak polarization. However, it is worth highlighting that the significantly lower polarization for semipolar LEDs does not mean that the polarization is zero. Furthermore, with increasing indium content in InGaN, the polarization in semipolar LEDs increases due to the enhancement in strain. Consequently, the carrier recombination lifetime of the semipolar LEDs also increases with increasing emission wavelength (i.e., increasing indium content), although this increase is not so significant as in its *c-plane* counterparts. As stated earlier, a modulation bandwidth is inversely proportional to the carrier recombination lifetime of a LED. The polarization of an III-nitride LED, which is enhanced with increasing emission wavelength (this requires higher indium content) will lead to a long recombination lifetime. As a result, the modulation bandwidth decreases with increasing emission wavelength. With increasing injection current density, the polarization can be partially screened out, leading to a reduction in carrier recombination lifetime. Of course, if a very high injection current density, beyond what is used in this work is employed (for example, in the case of microLEDs, where the emission mechanism is fully dominated by a nonradiative recombination mechanism), the situation is different and thus is beyond the scope of this work.

More interestingly, by fitting the data from LED-A, LED-B, and LED-C, it can be found that the 3 dB modulation bandwidth of these three LEDs as a function of injection current density follows a strong power law relationship, $f_{3dB} \propto J^k$. This suggests that a junction capacitance effect is not a limiting factor in the 3 dB modulation bandwidth of each device when the injection current density is below 92 A/cm^2 [26]. This means that a further increase in 3 dB bandwidth can be possibly achieved.

4.3.3 Differential carrier lifetime

The above small-signal microwave method can also be used to determine a differential carrier lifetime [30,31], rearranging Equation 3-2 gives

$$\tau_{diff} = \frac{1}{2\pi f_{3dB}}, \tag{4-1}$$

where τ_{diff} is the differential lifetime and f_{3dB} is the modulation bandwidth. Figure 4-5 exhibits the differential carrier lifetime as a function of injection current density for the three LEDs, demonstrating that the differential carrier lifetime increases with increasing emission wavelength. Furthermore, in each case, the differential carrier lifetime decreases with increasing injection current density. At 92 A/cm^2, LED-A shows a differential carrier time of 0.31 ns, which is shorter than that of LED-B, whose differential carrier lifetime is 0.56 ns. Both values are consistent with the carrier recombination lifetime with similar emission wavelengths obtained by time-resolved photoluminescence measurements (TRPL) [32], although a differential carrier lifetime, which also considers transport effects, is different from a carrier recombination lifetime (the former is typically smaller than the latter by a factor of 2−3 [33]). Of course, as expected, LED-C (amber LED) exhibits a stronger polarization than LED-A and LED-B. Consequently, LED-C exhibits a differential carrier lifetime of 0.92 ns, which is longer than those for LED-A and LED-B. This result also confirms that a reduction in carrier recombination lifetime with increasing injection current density can be attributed to the screening effect mentioned above. In contrast, the *c-plane* LED exhibits a typical differential carrier lifetime of >12 ns, which is far longer than those of our semipolar LEDs. However, it is worth noting that the differential carrier lifetimes of the semipolar LEDs are much shorter than those of any *c-plane* III-nitride LEDs, although the indium content in these semipolar LEDs is much higher than that for any *c-plane* blue LEDs. This further confirms that the fundamental physics for the significantly enhanced modulation bandwidth for these semipolar LEDs with long emission wavelengths is due to their intrinsically short recombination lifetime.
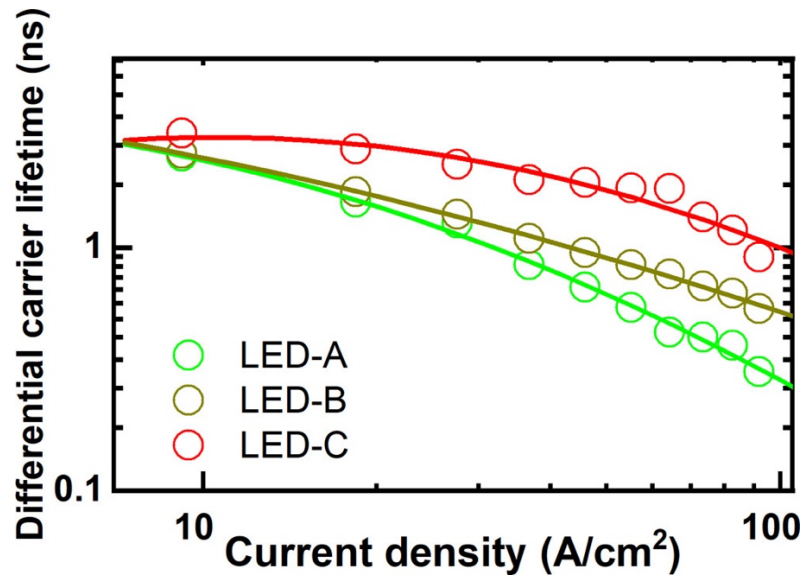
Figure 4-5 Differential carrier lifetimes of the three LEDs as a function of injection current density, which are extracted from the frequency response measurements. Solid lines are guides to the eye.

4.4   Summary

In conclusion, we have demonstrated a modulation bandwidth of 540 MHz for semipolar $(11\bar{2}2)$ green LEDs with typical dimensions of $330 \times 330\ \mu m^2$, which is a record modulation bandwidth for III-nitride macroLEDs (not microLEDs) reported so far. We also demonstrated a modulation bandwidth of 350 MHz for the semipolar $(11\bar{2}2)$ yellow LEDs and 140 MHz for the semipolar $(11\bar{2}2)$ amber LEDs, which are the first report for the longest wavelength III-nitride LEDs with such a high modulation bandwidth. All these long wavelength III-nitride LEDs are grown on our overgrowth semipolar $(11\bar{2}2)$ GaN with a significantly improved crystal quality on m-plane sapphire. The differential carrier lifetimes of these long wavelength LEDs have been extracted from frequency response measurements, further confirming that the significantly enhanced modulation bandwidth is due to the intrinsically low polarization. This result may pave the way for a next generation white light source, which can meet both the requirements for VLC and general illumination simultaneously.

4.5   References

(1)   Haas, H. LiFi Is a Paradigm-Shifting 5G Technology. *Rev. Phys.* **2018**, *3*, 26–31.

(2)   Wang, S. W.; Chen, F.; Liang, L.; He, S.; Wang, Y.; Chen, X.; Lu, W. A High-Performance Blue Filter for a White-Led-Based Visible Light Communication System. *IEEE Wirel. Commun.* **2015**, *22* (2), 61–67. https://doi.org/10.1109/MWC.2015.7096286.

(3)   Le Minh, H.; O'Brien, D.; Faulkner, G.; Zeng, L.; Lee, K.; Jung, D.; Oh, Y.; Won, E. T. 100-Mb/s NRZ Visible Light Communications Using a Postequalized White LED. *IEEE Photonics Technol. Lett.* **2009**, *21* (15), 1063–1065.

(4)   Chow, C. W.; Yeh, C. H.; Liu, Y. F.; Huang, P. Y.; Liu, Y. Adaptive Scheme for Maintaining the Performance of the In-Home White-LED Visible Light Wireless Communications Using OFDM. *Opt. Commun.* **2013**, *292*, 49–52. https://doi.org/10.1016/j.optcom.2012.11.081.

(5)   Takeuchi, T.; Amano, H.; Akasaki, I. Theoretical Study of Orientation Dependence of Piezoelectric Effects in Wurtzite Strained GaInN/GaN Heterostructures and Quantum Wells. *Jpn. J. Appl. Phys.* **2000**, *39* (Part 1, No. 2A), 413–416. https://doi.org/10.1143/jjap.39.413.

(6)   Bernardini, F.; Fiorentini, V.; Vanderbilt, D. *Spontaneous Polarization and Piezoelectric Constants of III-V Nitrides*; 1997.

(7)   Tsonev, D.; Chun, H.; Rajbhandari, S.; McKendry, J. J. D.; Videv, S.; Gu, E.; Haji, M.; Watson, S.; Kelly, A. E.; Faulkner, G. A 3-Gb/s Single-LED OFDM-Based Wireless VLC Link Using a Gallium Nitride $\mu {\rm LED}$. *IEEE photonics Technol. Lett.* **2014**, *26* (7), 637–640.

(8)   Manousiadis, P.; Chun, H.; Rajbhandari, S.; Mulyawan, R.; Vithanage, D. A.; Faulkner, G.; Tsonev, D.; McKendry, J. J. D.; Ijaz, M.; Xie, E. Demonstration of 2.3 Gb/s RGB White-Light VLC Using Polymer Based Colour-Converters and GaN Micro-LEDs. In *2015 IEEE Summer Topicals Meeting Series (SUM)*; IEEE, 2015; pp 222–223.

(9)   Rajbhandari, S.; Jalajakumari, A. V. N.; Chun, H.; Faulkner, G.; Cameron, K.; Henderson, R.; Tsonev, D.; Haas, H.; Xie, E.; McKendry, J. J. D. A Multigigabit per Second Integrated Multiple-Input Multiple-Output VLC Demonstrator. *J. Light. Technol.* **2017**, *35* (20), 4358–4365.

(10)   Islim, M. S.; Ferreira, R. X.; He, X.; Xie, E.; Videv, S.; Viola, S.; Watson, S.; Bamiedakis, N.; Penty, R. V; White, I. H.; Kelly, A. E.; Gu, E.; Haas, H.; Dawson, M. D. Towards 10 Gb/s Orthogonal Frequency Division Multiplexing-Based Visible Light Communication Using a GaN Violet Micro-LED. *Photonics Res.* **2017**, *5* (2), A35–A43. https://doi.org/10.1364/PRJ.5.000A35.

(11)   Ji, R.; Wang, S.; Liu, Q.; Lu, W. High-Speed Visible Light Communications: Enabling Technologies and State of the Art. *Appl. Sci.* **2018**, *8* (4), 589.

(12)   Jukaria, M.; Singh, B. K.; Kumar, A. Review of Li Fi Technology: Scope of next Generation Communication System for Home Area Network. *Int. J. Eng. Sci. Math.* **2018**, *7* (3), 265–275.

(13)   Mei, S.; Liu, X.; Zhang, W.; Liu, R.; Zheng, L.; Guo, R.; Tian, P. High-Bandwidth White-Light System Combining a Micro-LED with Perovskite Quantum Dots for Visible Light Communication. *ACS Appl. Mater. Interfaces* **2018**, *10* (6), 5641–5648.

(14)   Liu, X.; Lin, R.; Chen, H.; Zhang, S.; Qian, Z.; Zhou, G.; Chen, X.; Zhou, X.; Zheng, L.; Liu, R.; Tian, P. High-Bandwidth InGaN Self-Powered Detector Arrays toward MIMO Visible Light Communication Based on Micro-LED Arrays. *ACS Photonics* **2019**, *6* (12), 3186–3195. https://doi.org/10.1021/acsphotonics.9b00799.

(15)   Bai, J.; Cai, Y.; Feng, P.; Fletcher, P.; Zhao, X.; Zhu, C.; Wang, T. A Direct Epitaxial Approach to Achieving Ultrasmall and Ultrabright InGaN Micro Light-Emitting Diodes (MLEDs). *ACS photonics* **2020**, *7* (2), 411–415.

(16)   Konoplev, S. S.; Bulashevich, K. A.; Karpov, S. Y. From Large-size to Micro-LEDs: Scaling Trends Revealed by Modeling. *Phys. status solidi* **2018**, *215* (10), 1700508.

(17)   Olivier, F.; Tirano, S.; Dupré, L.; Aventurier, B.; Largeron, C.; Templier, F. Influence of Size-Reduction on the Performances of GaN-Based Micro-LEDs for Display Application. *J. Lumin.* **2017**, *191*, 112–116.

(18)   Masui, H.; Nakamura, S.; DenBaars, S. P.; Mishra, U. K. Nonpolar and Semipolar III-Nitride Light-Emitting Diodes: Achievements and Challenges. *IEEE Trans. Electron Devices* **2009**, *57* (1), 88–100.

(19)   Strittmatter, A.; Northrup, J. E.; Johnson, N. M.; Kisin, M. V.; Spiberg, P.; El-Ghoroury, H.; Usikov, A.; Syrkin, A. Semi-Polar Nitride Surfaces and Heterostructures. *Phys. status solidi* **2011**, *248* (3), 561–573. https://doi.org/10.1002/pssb.201046422.

(20)   Northrup, J. E. GaN and InGaN (1122) Surfaces: Group-III Adlayers and Indium Incorporation. *Appl. Phys. Lett.* **2009**, *95* (13). https://doi.org/10.1063/1.3240401.

(21)   Wang, T. Topical Review: Development of Overgrown Semi-Polar GaN for High Efficiency Green/Yellow Emission. *Semicond. Sci. Technol.* **2016**, *31* (9), 93003.

(22)   Bai, J.; Xu, B.; Guzman, F. G.; Xing, K.; Gong, Y.; Hou, Y.; Wang, T. (11-22) Semipolar InGaN Emitters from Green to Amber on Overgrown GaN on Micro-Rod Templates. *Appl. Phys. Lett.* **2015**, *107* (26), 261103.

(23)   Zhang, Y.; Bai, J.; Hou, Y.; Yu, X.; Gong, Y.; Smith, R. M.; Wang, T. Microstructure Investigation of Semi-Polar (11-22) GaN Overgrown on Differently Designed Micro-Rod Array Templates. *Appl. Phys. Lett.* **2016**, *109* (24). https://doi.org/10.1063/1.4972403.

(24)   Gong, Y.; Xing, K.; Xu, B.; Yu, X.; Li, Z.; Bai, J.; Wang, T. (Invited) High Efficiency Green-Yellow Emission from InGaN/GaN Quantum Well Structures Grown on Overgrown Semi-Polar (11-22) GaN on Regularly Arrayed Micro-Rod Templates. *ECS Trans.* **2015**, *66* (1), 151–155. https://doi.org/10.1149/06601.0151ecst.

(25)   Lee, C.; Zhang, C.; Becerra, D. L.; Lee, S.; Forman, C. A.; Oh, S. H.; Farrell, R. M.; Speck, J. S.; Nakamura, S.; Bowers, J. E. Dynamic Characteristics of 410 Nm Semipolar (20 2 1) Iii-Nitride Laser Diodes with a Modulation Bandwidth of over 5 Ghz. *Appl. Phys. Lett.* **2016**, *109* (10), 101104.

(26)   Dinh, D. V.; Quan, Z.; Roycroft, B.; Parbrook, P. J.; Corbett, B. GHz Bandwidth Semipolar (112‾2) InGaN/GaN Light-Emitting Diodes. *Opt. Lett.* **2016**, *41* (24), 5752. https://doi.org/10.1364/OL.41.005752.

(27)   Corbett, B.; Quan, Z.; Dinh, D. V.; Kozlowski, G.; O'Mahony, D.; Akhter, M.; Schulz, S.; Parbrook, P.; Maaskant, P.; Caliebe, M.; Hocker, M.; Thonke, K.; Scholz, F.; Pristovsek, M.; Han, Y.; Humphreys, C. J.; Brunner, F.; Weyers, M.; Meyer, T.

M.; Lymperakis, L. Development of Semipolar (11-22) LEDs on GaN Templates. *Light. Diodes Mater. Devices, Appl. Solid State Light. XX* **2016**, *9768* (March 2016), 97681G. https://doi.org/10.1117/12.2204758.

(28) Quan, Z.; Dinh, D. V; Presa, S.; Roycroft, B.; Foley, A.; Akhter, M.; O'Mahony, D.; Maaskant, P. P.; Caliebe, M.; Scholz, F. High Bandwidth Freestanding Semipolar (11–22) InGaN/GaN Light-Emitting Diodes. *IEEE Photonics J.* **2016**, *8* (5), 1–8.

(29) Haemmer, M.; Roycroft, B.; Akhter, M.; Dinh, D. V; Quan, Z.; Zhao, J.; Parbrook, P. J.; Corbett, B. Size-Dependent Bandwidth of Semipolar ($11\overline{2}2$) Light-Emitting-Diodes. *IEEE Photonics Technol. Lett.* **2018**, *30* (5), 439–442.

(30) Rajabi, K.; Wang, J.; Jin, J.; Xing, Y.; Wang, L.; Han, Y.; Sun, C.; Hao, Z.; Luo, Y.; Qian, K.; Chen, C.-J.; Wu, M.-C. Improving Modulation Bandwidth of C-Plane GaN-Based Light-Emitting Diodes by an Ultra-Thin Quantum Wells Design. *Opt. Express* **2018**, *26* (19), 24985. https://doi.org/10.1364/oe.26.024985.

(31) Monavarian, M.; Rashidi, A.; Aragon, A. A.; Oh, S. H.; Rishinaramangalam, A. K.; DenBaars, S. P.; Feezell, D. Impact of Crystal Orientation on the Modulation Bandwidth of InGaN/GaN Light-Emitting Diodes. *Appl. Phys. Lett.* **2018**, *112* (4), 41104.

(32) Liu, B.; Smith, R.; Athanasiou, M.; Yu, X.; Bai, J.; Wang, T. Temporally and Spatially Resolved Photoluminescence Investigation of (11 2 2) Semi-Polar InGaN/GaN Multiple Quantum Wells Grown on Nanorod Templates. *Appl. Phys. Lett.* **2014**, *105* (26), 261103.

(33) Coldren, L. A.; Corzine, S. W.; Mashanovitch, M. L. *Diode Lasers and Photonic Integrated Circuits*; John Wiley & Sons, 2012.

Chapter 5: Long-Wavelength Semipolar (11-22) InGaN/GaN LEDs with Multi- Gb/s Data Transmission Rates for VLC

Monolithic integration of red, green and blue (RGB) light-emitting diodes (LEDs) is crucial for white light visible light communication (VLC), display technology and general illumination but is intrinsically limited by the fundamental differences between the InGaN and AlGaInP epitaxial material systems typically used for visible wavelength emission. Increasing the indium content in traditional *c-plane* InGaN/GaN to achieve longer wavelength LEDs enhances the piezoelectric induced polarization resulting in a low quantum efficiency and long radiative lifetimes. These issues can be resolved by growing along a nonpolar or semipolar orientation. This chapter demonstrates the feasibility of the $(11\bar{2}2)$ semipolar LEDs for long wavelength VLC with an additional capability of monolithic integration to produce a single white light RGB chip. Based on our high performance semipolar InGaN/GaN LEDs, we report record data transmission rates of 4.22 Gb/s, 3.72 Gb/s and 336 Mb/s under the forward error correction (FEC) threshold standard for reliable communication for our green (515 nm), yellow (550 nm) and amber (600 nm) semipolar LEDs using adaptively bit-loaded DC-biased optical orthogonal frequency division multiplexing (DCO-OFDM).

5.1   Introduction

VLC is an emerging wireless communication technology, providing a complementary technology to RF based Wi-Fi/5G. In principle, VLC can offer a very large bandwidth which is about three orders of magnitude higher than current Wi-Fi, as a frequency bandwidth is inversely proportional to the square of wavelength (RF emissions are limited to 3 kHz to 300 GHz, while the much shorter wavelength visible light covers a huge range from 430 to 750 THz[1,2]). In general, a data transmission rate is determined by the bandwidth of a transmitter and the sensitivity of the receiver. Therefore, a high data transmission rate can be obtained by using a high efficiency visible LED with a high modulation bandwidth as a transmitter. Of course, SSL also requires high efficiency visible LEDs.

There has been a significant progress in developing white LEDs for solid state lighting (SSL) and VLC recently, which are mainly fabricated by means of employing light down-conversion from *c-plane* III-nitride blue LEDs to yellow, green or red via emitting phosphors. It is worth highlighting that such a white LED involves a considerable amount of energy loss during the down-conversion process. Furthermore, the modulation bandwidth is also

fundamentally limited by the naturally slow recombination lifetime of current *c-plane* III-nitride LEDs (due to their intrinsic polarisation effect as a result of large lattice-mismatch induced piezoelectrical fields in InGaN/GaN multiple quantum wells as an emitting region) and an extremely long response time of emitting phosphors[2,3]. Therefore, such a white LED is clearly not ideal. The ultimate white LED for both SSL and VLC is a monolithic integration of either three individual LED chips containing red, green and blue (i.e., RGB) emissions or at least two LEDs each emitting blue and yellow. Blue LEDs with high efficiency have been widely commercialized but are limited to those grown on *c-plane* substrates, suffering from a long recombination lifetime and thus leading to a small modulation bandwidth[4,5]. Furthermore, the optical performance of green and yellow LEDs, the longer emission wavelength emissions, are even worse than blue LEDs in terms of optical efficiency and modulation bandwidth. Currently, red LEDs are dominantly manufactured by utilising the AlGaInP material system[6]. It then seems logical to combine these two kinds of compound semiconductors by using a blue or green or even yellow LED from the InGaN system with a red LED from the AlInGaP system to create a much superior white light chip for VLC, thereby removing the need for phosphor conversion layers with a slow response time. However, it is a great challenge to monolithically integrate these two kinds of fundamentally different compound semiconductors onto a single substrate without facing mismatch and thermal issues. Therefore, it is necessary to develop III-nitride based long emission wavelength LEDs, such as yellow or even red LEDs with both high efficiency and high modulation bandwidth. This means that it is crucial to effectively both suppress the intrinsic polarisation issue and enhance indium incorporation into GaN whilst maintaining the high performance of InGaN alloys as an active region.

Benefiting by reducing the size of a device to the micron-scale, microLEDs can be driven at a very high current density, allowing microLEDs to be modulated at a high modulation bandwidth for VLC applications with GHz capabilities, which is very promising for VLC applications[7–14]. Unfortunately, the optical efficiency of current micro-LEDs is too low compared with broad area LEDs and thus cannot meet the requirements for both VLC and general illumination simultaneously at least before a step-change in optical efficiency for microLEDs can be achieved. Moreover, in addition to the incompatibility issue in terms of integrating InGaN LED and AlGaInP LEDs for the fabrication of white LEDs, the miniaturisation of AlGaInP based red LEDs with high performance is very difficult due to their higher surface recombination velocity resulting in a much lower external quantum efficiency (EQE) and thermal management issues compared with InGaN LEDs[15]. The EQE is further reduced because AlGaInP LEDs are lattice matched to a light absorbing GaAs substrate, drastically reducing the light extraction efficiency for red wavelengths[16].

One of the most effective routes to meeting these requirements is to grow LEDs along a semipolar orientation, in particular, $(11\bar{2}2)$ orientation, as InGaN grown on the $(11\bar{2}2)$ plane is predicted to exhibit both a significant reduction in polarization and an enhancement in indium incorporation into GaN[17]. The reduced polarisation is expected to lead to a short carrier recombination lifetime and thus an enhancement in optical efficiency[18]. The enhanced indium incorporation rate will favour material growth (whilst maintaining high indium content in InGaN to obtain a longer wavelength emission such as yellow and red) at a high temperature, leading to an improvement in crystal quality. However, the prerequisite is that $(11\bar{2}2)$ GaN templates with high crystal quality must be available, where long wavelength semipolar LEDs with high performance can be grown. In order to meet the material challenges, our group has established a number of cost-effective approaches to achieve high quality semipolar $(11\bar{2}2)$ GaN grown on *m-plane* sapphire, demonstrating very bright semi-polar InGaN LEDs covering a wide wavelength range up to amber[19–21]. In the previous chapter, frequency response measurements on these high-performance semipolar LEDs were presented, exhibiting a record modulation bandwidth of 540 MHz, 350 MHz and 140 MHz all with a broad area (with a typical dimension of $330 \times 330\ \mu m^2$) on our semi-polar green, yellow and amber LEDs, respectively[22]. This is also the report on modulation bandwidth for the longest wavelength III-nitride LEDs.

Given the high performance of these semipolar LEDs with long emission wavelengths and the record modulation bandwidth which we have achieved on these semipolar LEDs, it is worth exploring the upper-limit on the data transmission rate achievable on these long wavelength semipolar LEDs, which is crucial for eventually achieving monolithically integrated white LEDs for both SSL and VLC. In this chapter, we have reported a data transmission rate of 4.22 Gb/s for our green semipolar LEDs, 3.72 Gb/s for our yellow semipolar LEDs and 336 Mb/s for our amber LEDs, which are all the records for InGaN/GaN LEDs at their respective wavelengths. We hope these results demonstrate the benefits of semi-polar LEDs for VLC, potentially paving a new avenue to employ semipolar LEDs for eventually fabricating monolithically integrated white LEDs for both SSL and VLC.

A number of modulation schemes can be used to characterize the data throughput of LEDs. For this study, we first use a simple non-return-to-zero on-off keying (NRZ-OOK) approach to monitor eye-diagram performance at different fixed data transmission rates for each LED. To further enhance the data rates, a DCO-OFDM method adapted for intensity modulated direct detection (IMDD) systems has been employed. DCO-OFDM is chosen due to its relatively simple implementation whilst also outperforming other schemes such as pulse amplitude modulation (PAM) and carrierless amplitude phase modulation (CAP) as a result

of its spectrally efficient format which thrives in a dynamic-range and bandwidth limited VLC system[23]. Another advantage is that DCO-OFDM can be further extended spatially in order to take advantage of the cascaded device arrangement in a multiple-input multiple-output (MIMO) approach using MIMO-OFDM[24], which is particularly useful for measuring multiple monolithically integrated LEDs on a single chip substrate in the future. Single LED devices are demonstrated here to show the feasibility of the long wavelength VLC performance of the (11$\bar{2}$2) semipolar LEDs.

5.2   VLC system results

5.2.1   Experimental setup conditions

Figure 5-1a schematically illustrates our VLC system, allowing us to carry out NRZ-OOK and adaptively bit-loaded DCO-OFDM measurements on our semipolar LEDs, along with a photograph of the light collection optics in Figure 5-1b. For NRZ-OOK modulation, a 2^7-1 pseudorandom bit sequence (PRBS-7) which is initially generated using MATLAB is used to modulate the LEDs using an arbitrary waveform generator (Tektronix AWG70002A). The semipolar LEDs are modulated with the signal through a 40 GHz high-frequency probe. To maximise the SNR, the emission of our semipolar LEDs is collected from the backside of our devices, where the sapphire substrates have been polished and then lapped to ensure they are completely transparent. A 0.75NA, infinity-corrected objective with 40 × magnification is used to collect the emitted light. The collimated light is reflected off a dielectric coated mirror with a reflectivity of > 98% and then focused onto a 1.4 GHz high-speed photoreceiver with an integrated transimpedance amplifier using a 2″ aspheric lens. A 6 GHz, real-time sampling oscilloscope (Tektronix DPO70604C) with a sample rate of 25GS/s and an 8-bit ADC with a maximum record length of 31.3M samples is used to capture the modulated signal from the photoreceiver.
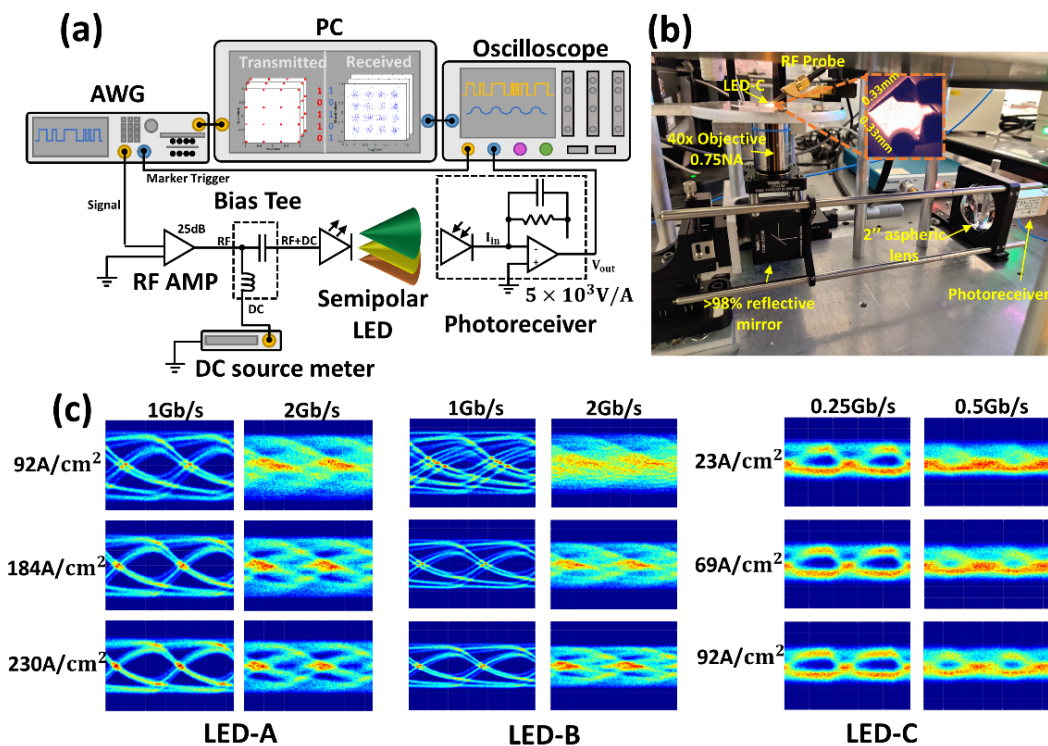
Figure 5-1 Schematic of our entire VLC system for demonstrating VLC with LEDs (a); photograph of our optical light collection system showing that emitted light is collected from the backside of a LEDs in order to enhance a signal to noise ratio (b); and (c) typical examples of the received eye-diagrams using our semipolar LEDs under various current densities for different data transmission rates measured under various current densities using NRZ-OOK with a modulation depth of 4.4 V for LED-A, LED-B and LED-C, respectively.

5.2.2   NRZ-OOK modulation

Figure 5-1c demonstrates a few typical examples of the received eye-diagrams using our semipolar LEDs under various current densities after NRZ-OOK modulation using a 0.25 V peak-to-peak PRBS signal amplified by 25 dB to ~4.4 V. For instance, for our semipolar green LEDs, a clear, open eye has been observed for LED-A at 1 Gb/s under 92, 184 and 230 A/cm^2, and clear, open eyes at 2Gb/s under 184 and 230 A/cm^2. Similarly, fully open eye diagrams for our semipolar yellow LED at 1 Gb/s under 92, 184 and 230 A/cm^2, and at 2 Gb/s under 230 A/cm^2. The eye diagram for our amber LED is fully open at 0.25 Gb/s under 23, 69 and 91 A/cm^2, while it shows a reduced eye at 0.5 Gb/s. In all cases, horizontal jitter is reduced with increasing a current density due to the reduction in recombination lifetime, resulting in a wider eye for LED-A and LED-B at 2 Gb/s and LED-C at 0.5 Gb/s. DCO-OFDM is performed after NRZ-OOK to further push the limits of the available bandwidth of the semipolar LEDs.

5.2.3   Channel estimation

Before any DCO-OFDM data transmission, the channel is first estimated using several pilot frames consisting of fixed rate 4 - quadrature amplitude modulation (QAM) symbols and measured through the channel on the oscilloscope. The estimate can then be used to apply a zero-forcing equaliser (ZF) on the data carrying frame transmitted afterwards. Since the additive white gaussian noise (AWGN) of the signal at the receiver is zero-mean, we can use a commonly implemented mean estimation technique[11] to characterise the effective gain on each subcarrier. Error-vector-magnitude (EVM) measurements were used to calculate the SNR on each subcarrier, SNR_k and then converted to decibel format. Each subcarrier is then adaptively loaded with $log_2 M_k$ bits where M_k is the M-ary QAM order on the kth subcarrier using the general probability of error equation for M-ary QAM[25]:

$$P_b \approx \frac{\sqrt{M_k}-1}{\sqrt{M_k}log_2\sqrt{M_k}} Q\left(\sqrt{\frac{3log_2 M_k \cdot SNR_k}{2(M_k-1)}}\right). \tag{5-1}$$

The total bit rate, R_b, can then be calculated using:

$$R_b = \frac{CB \times \sum_{k=1}^{N_{fft}} log_2 M_k}{(N_{fft} + N_{CP})} \tag{5-2}$$

where CB is the channel bandwidth, where N_{fft} is the total number of subcarriers and N_{CP} is the size of the prepended cyclic prefix (CP), which will be explained below.

Error-vector-magnitude (EVM) measurements and SNR

EVM measurements are used to characterise the signal impairments in a wireless channel by comparing the received signal to the transmitted signal on the constellation diagram. Specifically, an error vector is measured between the ideal, transmitted symbol and received symbol. The root-mean-square (rms) of all the magnitudes of the error vectors results in the EVM value for the signal. The relationship between the EVM and the SNR is calculated by

$$\text{SNR} = -\left[CF + 20log_{10}\left(\frac{EVM}{100\%}\right)\right],$$

(5-3)

where CF is the crest factor, which is an indicator of how large the peaks of a signal waveform are compared to the average value. For example, $CF = 1$ means there are no peaks in the signal i.e., a DC signal. For a 64-QAM signal, $CF = 3.7$.[25] The conversion arises from an EVM measurement being a ratio of voltages, whereas an SNR is a power ratio. Therefore, we can convert the two parameters by simply using the pre-factor $20log_{10}$. The minus sign is needed since EVM is a ratio of noise-to-signal and SNR is a ratio of signal-to-noise.

5.2.4   Adaptively loaded DC-biased optical OFDM modulation

The signal generation and processing method is shown in Figure 5-2 for DCO-OFDM measurements. Firstly, a PRBS is initially generated using MATLAB. The resulting vector is converted to parallel format and then arranged into blocks to be transmitted on $\frac{N_{fft}}{2} - 1$ data carrying subcarriers, where N_{fft} is the total number of subcarriers. The block of bits on the kth subcarrier is subsequently assigned to the kth QAM symbol, i.e., X_k. The measurements are based on an IMDD system, and thus the modulated signals must be real-valued (not the case in conventional OFDM). Leaving the first and π-shifted subcarriers unmodulated, i.e., $X_0 = X_{N/2} = 0$, allows us to impose Hermitian symmetry across the entire DCO-OFDM frame such that $X_{N_{fft}-k} = X_k^*$, achieving a real valued signal after the Inverse Fast Fourier Transform (IFFT)[26]. For simplicity, the average power of every QAM symbol in this study has been normalised to unity before transmission. After the IFFT, a few samples at the end of the real-valued time domain signal are prepended to the beginning of the waveform in the form of a CP to combat inter-symbol interference (ISI) and to convert the received waveform linear convolution with the channel into a circular convolution. This enables us to use a simple, single-tap ZF equaliser at the receiver since ISI is effectively eliminated due to the introduction of a CP[27]. A root-raised cosine (RRC) filter is then used for pulse shaping and oversampling of the waveform. Next, the signal is clipped at $[-3\sigma; 3\sigma]$, where σ denotes the standard deviation of the time domain waveform. The OFDM signal amplitude follows a gaussian probability distribution function with the majority of data

encoded to be within three standard deviations, therefore no significant loss of data is present at the transmitter. It can be achieved by choosing a suitable DC bias and then clipping the signal within the chosen range. By doing so, we will be in a comfortable position to ensure that the resulting clipped waveform remains undistorted, and any clipping noise can be ignored[26]. Finally, the clipped signal is converted to a compatible file for read-out through the AWG (Tektronix AWG70002A), where a digital-to-analogue conversion can be carried out using the AWG's 10-bit DAC.
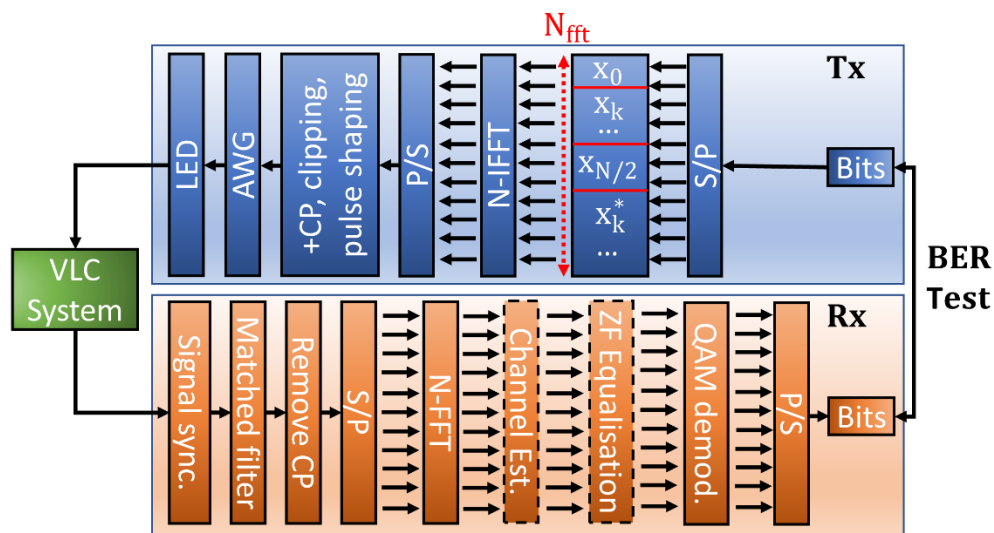
Figure 5-2 Detailed signal generation and data processing steps enabling DC-biased optical OFDM for our semipolar LEDs using MATLAB.

The analogue signal is further amplified using a 25 GHz broadband variable gain amplifier and then fed into a 12 GHz bias tee along with a DC bias from a source meter. The semipolar LEDs are then modulated with the signal through the 40 GHz high-frequency probe. The captured signal is synchronized with the transmitted signal by firstly decimating the oversampled oscilloscope signal to match the sample rate of the AWG, followed by using a cross-correlation method between the transmitted and measured signal. Matched filtering is applied to the aligned signal and the CP is removed. The signal is then buffered into a parallel format before performing the FFT. ZF equalisation is applied to the QAM symbols using the estimated channel prior to demodulation after which a bit-error ratio (BER) test is conducted.

Figure 5-3 below shows the I-V characteristics, voltage modulation and resulting current modulation when using the DCO-OFDM method for LED-A, LED-B and LED-C. LED-A and LED-B are modulated in their linear regimes where thermal roll-over occurs around 13.5 V for LED-A and 12 V for LED-B. LED-C shows no roll-over in the voltage range tested. Table 1 provides the test conditions and DCO-OFDM parameters used in this study for LED-A, LED-B and LED-C including peak wavelengths λ and 3dB bandwidths f_{3dB} at 100 mA.

The CB of the three channels with the corresponding AWG and oscilloscope (OSC) sample rates f_s are also included.
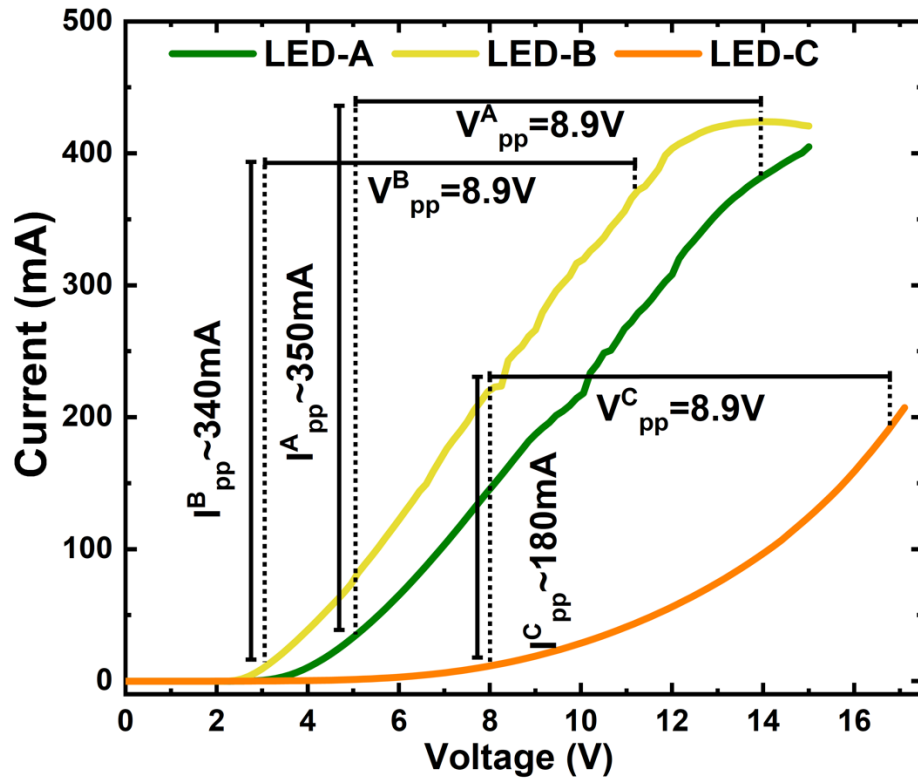
Figure 5-3 IV characteristics showing the regions of modulation voltage for DCO-OFDM modulation for LED-A, LED-B and LED-C.

Table 1. DCO-OFDM test conditions and characteristics for LED-A, LED-B and LED-C

Measurements Parameters	LED-A	LED-B	LED-C
Wavelength λ (nm)	515	550	596
f_{3dB} (MHz)	540	350	150
Channel bandwidth (MHz)	1000	1000	150
AWG f_s (GS/s)	8	8	1.2
Oversampling	4×	4×	4×
OSC f_s (GS/s)	25	25	6.25
N_{fft}	512	512	512
N_{CP}	16	16	16

Figure 5-4a, b and c show the strong EL spectra of our semipolar green, yellow and amber LEDs, for example, measured at 10 mA, where their EL emission images are also provided in their individual inset. The results demonstrate that a reduction in intrinsic piezoelectric

polarisation due to the growth along the $(11\bar{2}2)$ orientation compared with c- plane III-nitride LEDs allows these long wavelength LEDs (up to amber) to be still good enough to enable high data transmission rate performance. After channel estimation as described above, optical SNR profiles have been measured on our semipolar green, yellow and amber LEDs, which are shown in Figure 5-4d, e and f, respectively. Optical SNR profiles have been measured under different current densities, for example, 92 to 230 A/cm^2 for LED-A and LED-B, and 23 to 92 A/cm^2 for LED-C. In each case, the initial 0.5 V peak-to-peak waveform from the AWG is amplified by 25 dB to ~8.9V. The maximum voltage swing capable by the AWG is kept constant to ensure a full DAC dynamic range can be utilised. LED-A and LED-B use the maximum available bandwidth by the AWG when a 4 × oversampling factor is used. It is possible to further increase the channel bandwidth by lowering the oversampling factor or by using an AWG capable of a higher sample rate. The former is not ideal since this may reduce SNR and also introduce aliasing and phase distortion effects at a receiver. Therefore, a 4 × oversampling factor is chosen here at the expense of channel bandwidth. Due to the increased indium content in LED-C, the modulation bandwidth is lower than those of LED-A and LED-B[22] as well as the SNR per subcarrier.
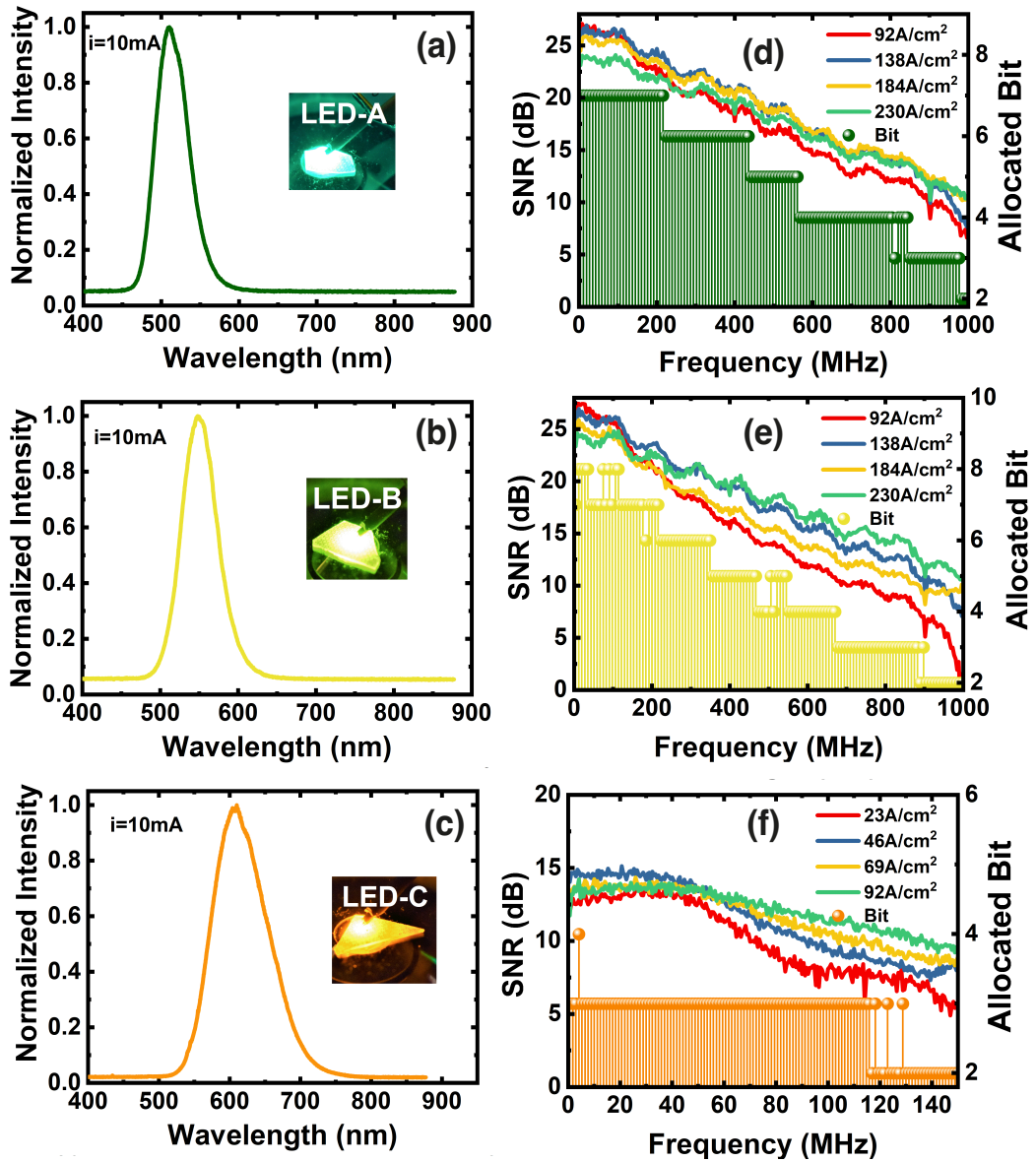
Figure 5-4 EL spectra of LED-A (a), LED-B (b), and LED-C (c) LEDs measured at 10 mA, where their EL emission images are also provided in their individual inset; optical SNR profiles demonstrating the SNR per subcarrier each adaptively loaded with a different number of bits at a target BER of $P_b = 3.8 \times 10^{-3}$ for LED-A (d), LED-B (e), and LED-C (f) LEDs, respectively.

To maximise BER performance, a reduced CB (which is reduced to 150 MHz) has been used for LED-C. With increasing current density, a similar effect to the eye diagrams as shown in Figure 5-1c has been observed. In general, for all the LEDs tested, the SNR per subcarrier profile becomes flatter at higher current densities due to an increase in the modulation bandwidth of the LEDs, resulting in better high-frequency performance. It is interesting to note that the lower current densities tested lead to slightly higher SNR closer to DC than at higher current densities. This is due to more of the available energy of the OFDM waveform being distributed among the lower frequencies than higher frequency subcarriers, resulting in a less flat profile. It is therefore important to choose a current density for adaptively loaded OFDM that has strong high-frequency performance but does not compromise in SNR at the low frequency subcarriers to maximise BER performance and data transmission rates. Therefore, 184 A/cm^2, 138 A/cm^2 and 92 A/cm^2 have been chosen as the DC bias points for LED-A, LED-B and LED-C for adaptively loaded DCO-OFDM, respectively. The SNR for each subcarrier has been measured for the whole channel. SNR is directly related to BER performance and data transmission rate as shown in Equation 5-1 and Equation 5-2. Therefore, we will be able to modulate each subcarrier with a different number of bits (corresponding to a different M-QAM order). By doing so, we can modulate the higher SNR subcarriers with a higher M-QAM order and conversely a lower M-QAM order for lower SNR subcarriers. This allows us to maximise the data transmission rate without compromising BER performance. Using a target BER of $P_b = 3.8 \times 10^{-3}$, i.e., the forward error correction (FEC) threshold standard for reliable communication, bits have been allocated to each subcarrier based on the SNR values at the chosen DC bias and have been provided in Figure 5-4d, e and f. The data transmission rate can be further improved with adaptive power loading in addition to bit loading which reduces crosstalk, this was attempted but no significant progress was achieved.

Figure 5-5 shows the BER performance as a function of data transmission rate for the three LEDs at different current densities, allowing us to identify a maximum data transmission rate which can be achieved for each LED. Based on the BER value standard for reliable communication (i.e., the FEC value) which has also been provided, Figure 5-5 demonstrates that maximum data transmission rates of 4.22Gb/s, 3.72Gb/s and 336Mb/s have been achieved against BER performance of 1.8×10^{-3}, 1.4×10^{-3}, and 3.6×10^{-3}, for LED-A, LED-B and LED-C, respectively. These results which have been achieved without the oscilloscope averaging function to represent a real-world VLC application. In general, either the lowest or highest of current density tested tends to lead to the worst results in terms of BER performance. This is likely due to the DC bias being either too high or too low for the modulation depth used in this study, resulting in modulating the nonlinear region of the LED

and thus distorting the modulated signal and increasing the BER. To the best of our knowledge, these results represent record data transmission rates for InGaN/GaN LEDs with a long emission wavelength, such as in the green and above green spectral range (>515 nm). Table 5-1 benchmarks our semipolar LEDs against the current state-of-the-art long wavelength (> 500 nm) InGaN LEDs reported for VLC applications and shows data transmission rate results where possible.
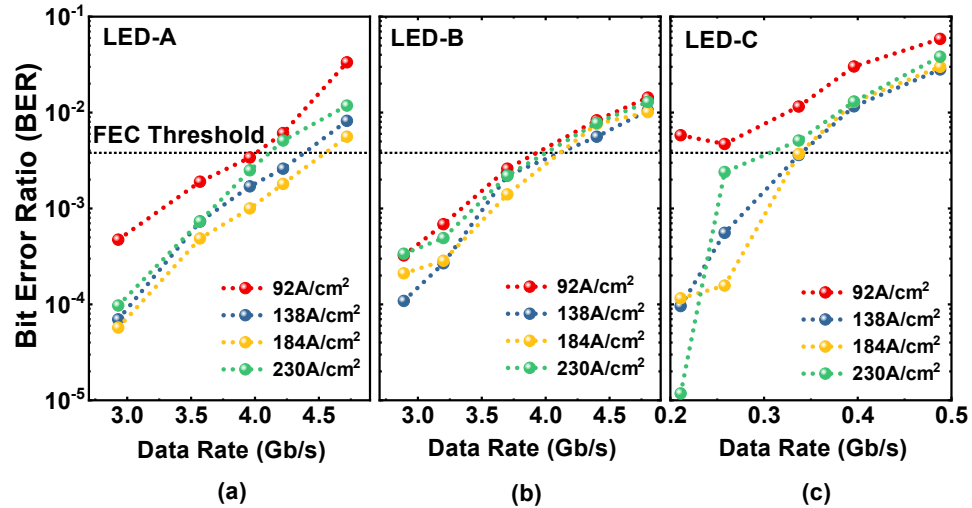
Figure 5-5 BER performance as a function of data transmission rate for LED-A (a), LED-B (b), and LED-C (c) obtained at different current densities, allowing us to identify a maximum data transmission rate, which can be achieved for each individual LED.

Table 5-1 Benchmarking Our Work against the Current State-of-the-Art Long-Wavelength InGaN LEDs Above 500 nm with Reported VLC Characteristics

Year	Ref.	LEDs	λ (nm)	Bandwidth (MHz)	Modulation Scheme	Data rate (Gbps)	BER
2008	Ref. 25	*c-plane*	500	330	-	-	-
2012	Ref. 26	*c-plane*	520	400	OOK-RZ	1.1	< FEC
2014	Ref. 27	*c-plane*	500	463	-	-	-
2016	Ref. 28	(11$\bar{2}$2)	500	100	-	-	-
2018	Ref. 29	*c-plane*	520	340	DCO-OFDM	2.16	<FEC
2019	Ref. 30	*c-plane*	515	144 (-6dB)	WDM, DCO-OFDM	0.62	<FEC
2020	Ref. 31	(20-21)	427 / 560	410	-	-	-
2020	Ref. 32	(20-21)	525	756	OOK-NRZ	1.5	<FEC
2021	**This work**	(11$\bar{2}$2)	515	540	DCO-OFDM, OOK-NRZ	4.22	1.8×10^{-3}
			550	350		3.72	1.4×10^{-3}
			596	150		0.34	3.6×10^{-3}

Figure 5-6a shows the received power spectra of the adaptively loaded OFDM waveforms, measured at their respective maximum data transmission rates of 4.42 Gb/s, 3.72 Gb/s and 336 Mb/s for LED-A, LED-B and LED-C respectively, as obtained using Equation 5-2. Comparing to the transmitted waveform before amplification (shown in black) a reduction in received power has been observed at higher frequency for each LED, following similarly to their respective SNR profiles.

Figure 5-6b displays the equalised QAM constellations (using the channel estimation method) of three out of the total of 255 subcarriers at various points in the channel for each LED with their corresponding M-QAM order labelled. Figure 5-6b clearly indicates that lower frequency subcarriers can be modulated with a higher order M-QAM due to their higher SNR compared with the lower order M-QAM, higher frequency subcarriers. The SNR change with frequency is clearly evident due to the noisier profiles on the lower order M-QAM constellations for all LEDs. However, due to the lower M-QAM order adaptively loaded on these subcarriers, we should still achieve similar BER performance to the higher SNR subcarriers. Figure 5-6b demonstrates that peak constellations of 128QAM, 128QAM and 8QAM have been achieved for LED-A, LED-B and LED-C, respectively.

5.3   Summary

In conclusion, record data transmission rates for VLC applications have been achieved by using our high-performance semipolar LEDs with a long emission wavelength of up to amber, which cannot be obtained using current *c-plane* III-nitride LEDs. The growth of III-nitride LEDs along the (11$\bar{2}$2) semipolar direction allows us to incorporate more indium into the InGaN quantum wells whilst also suppressing piezoelectric induced polarisation resulting in a higher bandwidth, SNR and therefore an enhanced data transmission rate. This allows multi-Gb/s speeds at longer emission wavelengths. Since all the LEDs utilise the same III-nitride material system without the need for any down-conversion phosphors, a monolithic LED chip integration of white light Gb/s VLC and SSL could be potentially possible. Further improvement could involve reducing the size of the LEDs to micro-LEDs to further enhance the modulation bandwidth; however, this would reduce the SNR of single LEDs due to their lower optical power output. Integrating multiple arrays of different wavelength semipolar microLEDs could address these challenging issues.
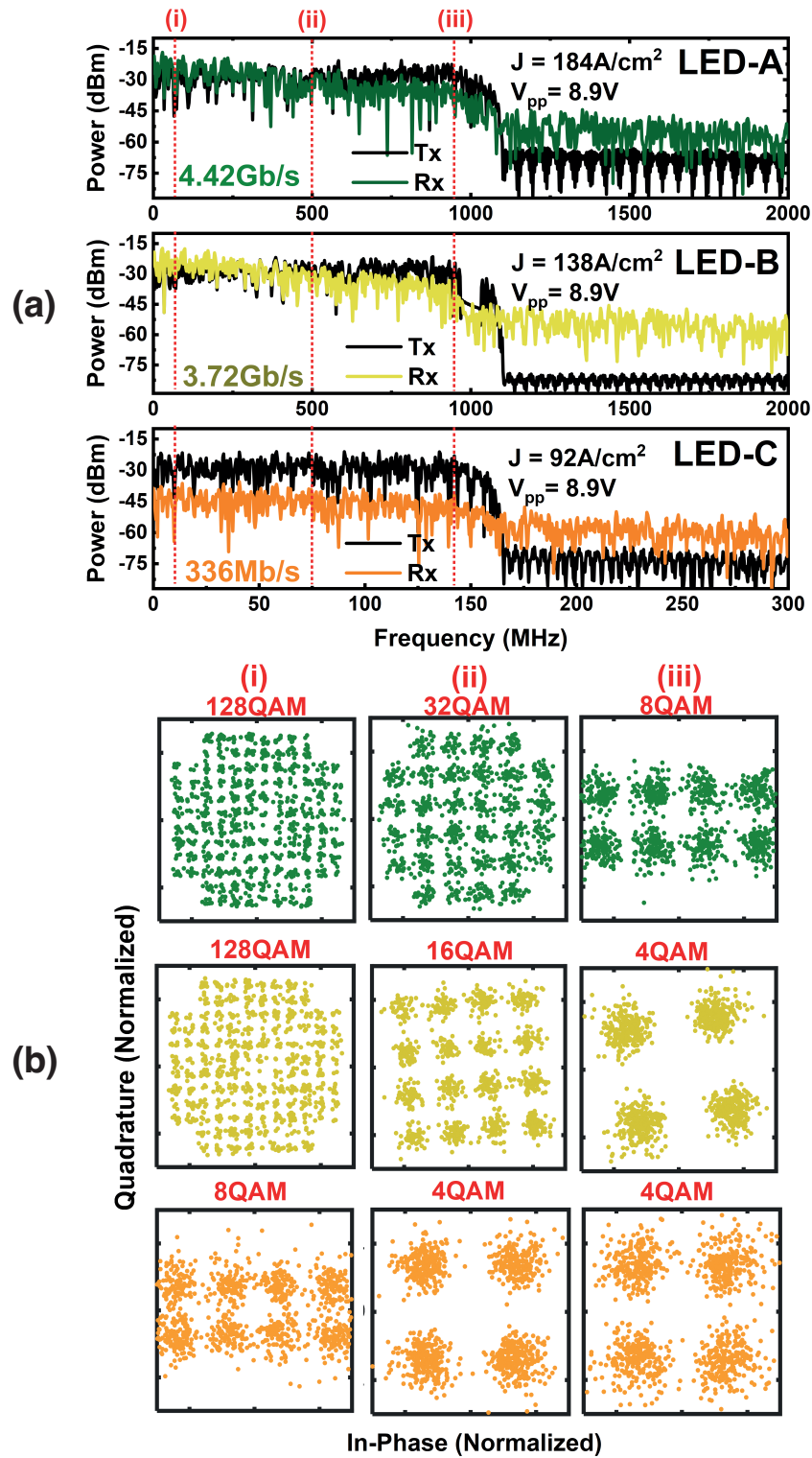
Figure 5-6 Received power spectra of adaptively loaded OFDM waveforms measured at their respective maximum data transmission rates of 4.42 Gb/s, 3.72 Gb/s, and 336 Mb/s for LED-A, LED-B, and LED-C, respectively, and (b) equalized QAM constellations (using a pilot sequence) of three out of the total of 255 subcarriers at various points in the channel for each LED with their corresponding M-QAM order labelled.

5.4   References

(1)   Haas, H. LiFi Is a Paradigm-Shifting 5G Technology. *Rev. Phys.* **2018**, *3*, 26–31.

(2)   Wang, S. W.; Chen, F.; Liang, L.; He, S.; Wang, Y.; Chen, X.; Lu, W. A High-Performance Blue Filter for a White-Led-Based Visible Light Communication System. *IEEE Wirel. Commun.* **2015**, *22* (2), 61–67. https://doi.org/10.1109/MWC.2015.7096286.

(3)   Chow, C. W.; Yeh, C. H.; Liu, Y. F.; Huang, P. Y.; Liu, Y. Adaptive Scheme for Maintaining the Performance of the In-Home White-LED Visible Light Wireless Communications Using OFDM. *Opt. Commun.* **2013**, *292*, 49–52. https://doi.org/10.1016/j.optcom.2012.11.081.

(4)   Bernardini, F.; Fiorentini, V.; Vanderbilt, D. *Spontaneous Polarization and Piezoelectric Constants of III-V Nitrides*; 1997.

(5)   Takeuchi, T.; Amano, H.; Akasaki, I. Theoretical Study of Orientation Dependence of Piezoelectric Effects in Wurtzite Strained GaInN/GaN Heterostructures and Quantum Wells. *Jpn. J. Appl. Phys.* **2000**, *39* (Part 1, No. 2A), 413–416. https://doi.org/10.1143/jjap.39.413.

(6)   Yadav, A.; Titkov, I. E.; Sokolovskii, G. S.; Karpov, S. Y.; Dudelev, V. V.; Soboleva, K. K.; Strassburg, M.; Pietzonka, I.; Lugauer, H.-J.; Rafailov, E. U. AlGaInP Red-Emitting Light Emitting Diode under Extremely High Pulsed Pumping. In *Light-Emitting Diodes: Materials, Devices, and Applications for Solid State Lighting XX*; SPIE, 2016; Vol. 9768, p 97681K. https://doi.org/10.1117/12.2213344.

(7)   Ji, R.; Wang, S.; Liu, Q.; Lu, W. High-Speed Visible Light Communications: Enabling Technologies and State of the Art. *Appl. Sci.* **2018**, *8* (4), 589.

(8)   Jukaria, M.; Singh, B. K.; Kumar, A. Review of Li Fi Technology: Scope of next Generation Communication System for Home Area Network. *Int. J. Eng. Sci. Math.* **2018**, *7* (3), 265–275.

(9)   Mei, S.; Liu, X.; Zhang, W.; Liu, R.; Zheng, L.; Guo, R.; Tian, P. High-Bandwidth White-Light System Combining a Micro-LED with Perovskite Quantum Dots for Visible Light Communication. *ACS Appl. Mater. Interfaces* **2018**, *10* (6), 5641–5648.

(10)   Liu, X.; Lin, R.; Chen, H.; Zhang, S.; Qian, Z.; Zhou, G.; Chen, X.; Zhou, X.; Zheng, L.; Liu, R.; Tian, P. High-Bandwidth InGaN Self-Powered Detector Arrays toward MIMO Visible Light Communication Based on Micro-LED Arrays. *ACS Photonics* **2019**, *6* (12), 3186–3195. https://doi.org/10.1021/acsphotonics.9b00799.

(11)   Tsonev, D.; Chun, H.; Rajbhandari, S.; McKendry, J. J. D.; Videv, S.; Gu, E.; Haji, M.; Watson, S.; Kelly, A. E.; Faulkner, G. A 3-Gb/s Single-LED OFDM-Based Wireless VLC Link Using a Gallium Nitride $\mu {\rm LED}$. *IEEE photonics Technol. Lett.* **2014**, *26* (7), 637–640.

(12)   Ferreira, R. X. G.; Xie, E.; McKendry, J. J. D.; Rajbhandari, S.; Chun, H.; Faulkner, G.; Watson, S.; Kelly, A. E.; Gu, E.; Penty, R. V. High Bandwidth GaN-Based Micro-LEDs for Multi-Gb/s Visible Light Communications. *IEEE Photonics Technol. Lett.* **2016**, *28* (19), 2023–2026.

(13)   Islim, M. S.; Ferreira, R. X.; He, X.; Xie, E.; Videv, S.; Viola, S.; Watson, S.; Bamiedakis, N.; Penty, R. V; White, I. H.; Kelly, A. E.; Gu, E.; Haas, H.; Dawson, M. D. Towards 10 Gb/s Orthogonal Frequency Division Multiplexing-Based Visible Light Communication Using a GaN Violet Micro-LED.

Photonics Res. **2017**, *5* (2), A35–A43. https://doi.org/10.1364/PRJ.5.000A35.

(14)   Xie, E.; Bian, R.; He, X.; Islim, M. S.; Chen, C.; McKendry, J. J. D.; Gu, E.; Haas, H.; Dawson, M. D. Over 10 Gbps VLC for Long-Distance Applications Using a GaN-Based Series-Biased Micro-LED Array. *IEEE Photonics Technol. Lett.* **2020**, *32* (9), 499–502.

(15)   Oh, J.-T.; Lee, S.-Y.; Moon, Y.-T.; Moon, J. H.; Park, S.; Hong, K. Y.; Song, K. Y.; Oh, C.; Shim, J.-I.; Jeong, H.-H. Light Output Performance of Red AlGaInP-Based Light Emitting Diodes with Different Chip Geometries and Structures. *Opt. Express* **2018**, *26* (9), 11194–11200.

(16)   Horng, R. H.; Sinha, S.; Lee, C. P.; Feng, H. A.; Chung, C. Y.; Tu, C. W. Composite Metal Substrate for Thin Film AlGaInP LED Applications. *Opt. Express* **2019**, *27* (8), A397. https://doi.org/10.1364/oe.27.00a397.

(17)   Northrup, J. E. GaN and InGaN (1122) Surfaces: Group-III Adlayers and Indium Incorporation. *Appl. Phys. Lett.* **2009**, *95* (13). https://doi.org/10.1063/1.3240401.

(18)   Wang, T. Topical Review: Development of Overgrown Semi-Polar GaN for High Efficiency Green/Yellow Emission. *Semicond. Sci. Technol.* **2016**, *31* (9), 93003.

(19)   Bai, J.; Xu, B.; Guzman, F. G.; Xing, K.; Gong, Y.; Hou, Y.; Wang, T. (11-22) Semipolar InGaN Emitters from Green to Amber on Overgrown GaN on Micro-Rod Templates. *Appl. Phys. Lett.* **2015**, *107* (26). https://doi.org/10.1063/1.4939132.

(20)   Zhang, Y.; Bai, J.; Hou, Y.; Yu, X.; Gong, Y.; Smith, R. M.; Wang, T. Microstructure Investigation of Semi-Polar (11-22) GaN Overgrown on Differently Designed Micro-Rod Array Templates. *Appl. Phys. Lett.* **2016**, *109* (24). https://doi.org/10.1063/1.4972403.

(21)   Gong, Y.; Xing, K.; Xu, B.; Yu, X.; Li, Z.; Bai, J.; Wang, T. (Invited) High Efficiency Green-Yellow Emission from InGaN/GaN Quantum Well Structures Grown on Overgrown Semi-Polar (11-22) GaN on Regularly Arrayed Micro-Rod Templates. *ECS Trans.* **2015**, *66* (1), 151–155. https://doi.org/10.1149/06601.0151ecst.

(22)   Haggar, J. I. H.; Cai, Y.; Ghataora, S. S.; Smith, R. M.; Bai, J.; Wang, T. High Modulation Bandwidth of Semipolar (11–22) InGaN/GaN LEDs with Long Wavelength Emission. *ACS Appl. Electron. Mater.* **2020**, *2* (8), 2363–2368.

(23)   Dimitrov, S.; Haas, H. Information Rate of OFDM-Based Optical Wireless Communication Systems with Nonlinear Distortion. *J. Light. Technol.* **2012**, *31* (6), 918–929.

(24)   Azhar, A. H.; Tran, T.-A.; O'Brien, D. A Gigabit/s Indoor Wireless Transmission Using MIMO-OFDM Visible-Light Communications. *IEEE photonics Technol. Lett.* **2012**, *25* (2), 171–174.

(25)   Yoon, D.; Cho, K.; Lee, J. Bit Error Probability of M-Ary Quadrature Amplitude Modulation. In *Vehicular Technology Conference Fall 2000. IEEE VTS Fall VTC2000. 52nd Vehicular Technology Conference (Cat. No. 00CH37152)*; IEEE, 2000; Vol. 5, pp 2422–2427.

(26)   Kazemi, H.; Haas, H. On the Performance of Single Side-Band OFDM for Band-Limited Visible Light Communication. In *2020 IEEE International Conference on Communications Workshops (ICC Workshops)*; IEEE, 2020; pp 1–6.

(27)   Dimitrov, S.; Haas, H. *Principles of LED Light Communications: Towards*

Networked Li-Fi; Cambridge University Press: Cambridge, 2015. https://doi.org/DOI: 10.1017/CBO9781107278929.

Chapter 6: A study of the luminescence decay of a semipolar green LED for visible light communications by time-resolved electroluminescence

Time resolved photoluminescence (TRPL) is often used to study the excitonic dynamics of semiconductor optoelectronics such as the carrier recombination lifetime of III-nitride LEDs. However, for any real-world application that requires light emitting diodes (LEDs) under electrical injection, TRPL suffers an intrinsic limitation due to the absence of taking carrier transport effects into account. This becomes a severe issue for III-nitride LEDs used for visible light communications (VLC) since the modulation bandwidth for VLC is determined by the overall carrier lifetime of a LED, not just its carrier recombination lifetime. Time resolved electroluminescence (TREL), which can characterize the luminescent decay of a LED under electrical injection to simulate real-world conditions when used in practical applications, is required. Both TRPL and TREL have been carried out on a semipolar LED and a standard *c-plane* LED (i.e., polar LED) both in the green spectral region for a comparison study. The $(11\bar{2}2)$ green semipolar LED exhibits much faster differential carrier lifetimes than the *c-plane* LED. In addition to a fast and a slow exponential component of 0.40 ns and 1.2 ns which are similar to those obtained by TRPL, a third lifetime of 8.3 ns due to transport related effects has obtained from TREL, which has been confirmed by capacitance measurements. It has been found that the overall carrier lifetime of a *c-plane* LED is mainly limited by resistance-capacitance (RC) effects due to a junction capacitance, while it is not the case for a semipolar LED due to intrinsically reduced polarization, demonstrating the major advantages of using a semipolar LED for VLC.

6.1   Introduction

There is an increasing demand for developing a VLC technology which is based on a visible emitter (either LED or laser diode) as a transmitter, an emerging wireless communication technology offering a complementary approach to RF based Wi-Fi and 5G. As a result of using visible light whose wavelength is much shorter than those of RF, the frequency bandwidth exhibits more than three orders of magnitude larger than those for RF. It has been predicted that VLC provides a long-term solution to the looming radio frequency (RF) 'spectrum crunch' due to a substantial increase in data demand.[1]

The data transmission rate is determined by the bandwidth of a transmitter and the signal-to-noise ratio (SNR) of the channel. A high data transmission rate requires a visible emitter with both high output power and a short carrier lifetime. TRPL is a powerful tool for characterizing a carrier recombination lifetime but is fundamentally confined to the active region of an emitter and does not contain information about carrier transport through the emitter structure, active region carrier density or performance when considering real-world LED applications under biasing conditions (i.e., electrical injection).[2-4] Therefore, it is crucial to explore a method which allows us to study the carrier dynamics of an emitter under biasing conditions for VLC applications.

In general, the modulation bandwidth of a LED (labelled as f_{3dB}) is inversely proportional to the overall carrier lifetime of a LED (labelled as τ), i.e., $f_{3dB} \propto 1/\tau$, which can be described in more detail by Equation 6-1 given below:

$$f_{3dB} \propto \frac{1}{\tau_{total}} = \frac{1}{\tau_{rad}} + \frac{1}{\tau_{non-rad}} + \frac{1}{\tau_{RC}} \qquad (6\text{-}1)$$

where τ_{rad} is the lifetime due to radiative recombination and $\tau_{non-rad}$ the lifetime due to non-radiative recombination. It is worth highlighting the 3rd component labelled as τ_{RC} is the lifetime due to the junction capacitance of an emitter, i.e., the so-called RC effects (i.e., resistance labelled as R and junction capacitance labelled as C). The junction capacitance of an emitter depends on its dimension. A standard III-nitride LED is > 300 μm × 300 μm. Generally speaking, an emitter with an area of < 100 μm² is not limited by τ_{RC} as the carrier lifetime dominates the modulation response rather than the geometrical capacitance.[5-8] However, broader area LEDs are desirable in terms of easier fabrication, higher optical power and cheaper integration solutions. It is essential to consider τ_{RC} if broad area LEDs are used for VLC applications.

τ_{rad} and $\tau_{non-rad}$ are normally studied and can be separated by means of using temperature dependent TRPL measurements with the assumption that $\tau_{non-rad}$ is negligible at a low temperature.[4] This method, while being sufficient for the optical investigation of an emitter under optical pumping conditions, does not tell the whole story for an emitter under biasing conditions since TRPL completely neglects carrier transport effects. Moreover, since TRPL is performed under optical pumping, it is challenging to quantify the carrier density in the active region of an emitter. Therefore, τ_{rad} only provides an approximate characterization since $\tau_{rad} = 1/BN$ where B is the recombination coefficient and N is the carrier density.[9] There is an alternative to TRPL, namely, time-resolved photocurrent (TRPC) which has been applied to the investigation of transport effects of GaInP solar cells.[10] For VLC applications,

electroluminescence measurements are essential. TRPL has also been studied on LEDs whilst simultaneously under electrical bias, which gives insight on the suppression of QCSE fields in semipolar devices.[10]

In an ideal case, the luminescent decay of a LED should be characterised under electrical injection to simulate real-world conditions when used in practical applications. Therefore, TREL measurements as a function of bias allows us to accurately investigate the decay dynamics of a LED for practical applications, which is particularly important for VLC applications. TREL demonstrates two major benefits. The excitation signal (electrically injected square wave with an ultrafast falling edge) used for TREL can be described as a small perturbation compared to the DC bias used to electrically drive a LED, i.e., *dR/dN*. The resulting lifetimes measured are therefore *differential lifetimes* instead of carrier recombination lifetimes measured from TRPL, the latter being around 2-3 times smaller than the former.[11,12] The carrier density in the active region can be then calculated by simply integrating the differential lifetime across the thickness of the active region.

Differential carrier lifetime has been studied extensively using various methods for optoelectronics with most reports based on network analysers (VNAs), where both the impedance and the optical modulation response of a LED can be measured and both responses can be fit simultaneously to a physical model.[12-16] The optical receivers are usually silicon-based photodetectors with either integrated transimpedance amplifiers or separate operational amplifiers which intrinsically suffer from low responsivity in the visible spectral range (for example, 0.1 A/W at 450 nm). As III-nitride emitters used as transmitters for VLC applications are approaching the limit of these detectors,[17-19] recent efforts are focused on finding new alternatives for the receivers in VLC characterization systems. By means of using a combination of time-correlated single photon counting (TCSPC) electronics and hybrid photomultiplier tubes (PMTs) which are similar to what are used in TRPL, we can establish an electrically injected time resolved system that exhibits high sensitivity with impulse responses < 50 ps compared with conventional photodetectors used in frequency domain systems.

There are also key issues associated with commercially available LEDs used for VLC. Commercially available white LEDs are typically fabricated by using polar orientated III-nitride blue LEDs grown on *c-plane* substrates coupled with yellow phosphors as conversion layers, where such a LED suffers greatly from strain induced piezoelectric fields across the InGaN/GaN multiple quantum well (MQW) emitting region.[20,21] The blue LEDs experience a reduced overlap between the electron-hole wavefunctions, leading to a long radiative

recombination time and thus low quantum efficiency, i.e., the quantum confined stark effect (QCSE). The colour conversion process is also very slow, resulting in increased response lifetimes.[22] Replacing the phosphor layers by longer wavelength emitters such as yellow or red LEDs results in an even larger strain across the InGaN MQWs and therefore an enhanced QCSE, which further increases the carrier recombination lifetime. Growing III-nitride LEDs along a semipolar or nonpolar orientation, such as the LEDs grown on (11$\bar{2}$2) semi-polar substrates, have been proposed to naturally minimise or even eliminate the QCSE, effectively increasing the recombination rate.[23] The (11$\bar{2}$2) orientation also facilitates the enhancement of indium incorporation into InGaN enabling longer wavelength emitters along with a reduction in polarisation.[24]

Recently, we have demonstrated record breaking modulation bandwidths and multi-Gb/s data transmission rates for our large area semipolar LEDs up to the amber spectral region.[12, 26] In this chapter, we explore further into the nature of semipolar LEDs due to reduced polarisation and their benefits for VLC. Both TREL and TRPL measurements have been performed on two different kinds of green LEDs, one grown on *c-plane* sapphire, whilst the other grown on our high-quality semipolar (11-22) GaN overgrown on *m-plane* sapphire substrates.[25] Interestingly, we have found that even though RC measurements suggest that both the *c-plane* LED and the semi-polar LED should be limited by τ_{RC}, only the *c-plane* LED suggests τ_{RC} is a limiting factor while the TREL data from the semipolar LED are comparable to their TRPL results. Our results have shown that the semipolar LED demonstrates an increased recombination rate compared with the *c-plane* LED. More importantly, it has been found out that RC effects exhibit less contribution to the overall carrier lifetime for the semipolar LED than that for the *c-plane* LED, demonstrating the major advantage of using semipolar LEDs for VLC applications compared with *c-plane* LEDs.

6.2   Experimental setup conditions

6.2.1   LED fabrication

Two different kinds of green LEDs have been used in the present study: one standard LED on *c-plane* sapphire and one (11$\bar{2}$2) semipolar LED on our high-quality semipolar (11$\bar{2}$2) GaN overgrown on *m-plane* sapphire.[25,27,35] The *c-plane* LED consists of 7 periods of $In_{0.25}Ga_{0.75}N$/GaN MQW structures (well: 2.5 nm and barrier:13.5 nm). For the semipolar LED, please refer to our previously published papers. [25, 27, 35] A 3 nm single quantum well sandwiched between two 9 nm thick quantum barriers was used as an emitting region for the semipolar LED, and the nominal indium content is 29 %. LEDs with a typical dimension of 330 × 330 μm^2 have been fabricated using a standard photolithography and dry-etching method. A 100 nm thick ITO film was deposited on top of the device to form a transparent

p-contact and then annealed using rapid thermal annealing (RTA). A Ti/Al/Ti/Au stack was thermally evaporated onto the n-GaN to form the n-contact. Finally, Ti/Au was deposited on both contacts to form the p- and n- electrodes.

6.2.2   Time resolved photoluminescence

A pulsed 375 nm laser diode with a 50 ps pulse width and a repetition rate of 16 MHz is used as an excitation source. The laser spot size is focussed to 2 μm diameter using a NUV 0.43NA infinity corrected objective lens. The emission is collected through the same lens and coupled into a multimode fibre. The light is then dispersed through a monochromator before focusing onto a hybrid PMT. The overall system has an approximate timing resolution of 15 ps and an instrument response time of 150 ps which is deconvolved from each measurement.

6.2.3   Time resolved electroluminescence

An excitation signal consisting of a 10 MHz (1MHz for the *c-plane* LED) square wave with amplitude 500 mV (peak-to-peak) is created using an arbitrary waveform generator (AWG). An identical waveform is created on the adjacent AWG channel and used as a trigger for a TCSPC timing electronics system. The excitation signal is combined with a DC bias from a power supply through a 12 GHz bias tee. A 40 GHz RF probe is then used to deliver the resulting RF + DC signal to the LED under test. To monitor the input electrical pulse that includes the effect from the cables, bias tee etc., the signal is first connected to a 6 GHz oscilloscope before the LED. After initial checks, the resulting modulated LED emission is collected through a 50 x magnification, 0.42 NA infinity corrected objective. A 50:50 beam splitter is used to split half the collimated light onto a charge coupled device (CCD) camera (for aligning, probing etc.) using a lens tube while the other half is coupled into a multimode fibre using a parabolic collimator. The light is then dispersed through a diffraction grating in a monochromator and then focussed onto a hybrid PMT for TCSPC measurements. A flip mirror is used to switch between the PMT and a CCD for spectral measurements. Timing synchronisation is achieved by combining TCSPC electronics with the falling edge of the trigger signal from the AWG and hybrid PMT measurements.

6.3   Results and discussion

Figure 6-1a shows the current-voltage (I-V) characteristics of both the semipolar LED and the *c-plane* LED, indicating turn-on voltages (measured at 20mA) of 4.3 V and 2.5 V with corresponding series resistances of 36 Ω and 22 Ω for the semipolar LED and the *c-plane* LEDs, respectively. Figure 6-1b exhibits the capacitance and resistance of these two LEDs measured using a precision LCR meter at 1 MHz in a parallel circuit mode, where the capacitance of a LED is given by its depletion capacitance below 0 V.[26] Therefore, the RC time constant of each LED can be obtained using the series resistance and the depletion

capacitance under negative bias. In this case, capacitance values of 194 pF and 173 pF have been measured at -2 V, corresponding to RC time constants of 7.0 ns and 3.8 ns for the semipolar LED and the *c-plane* LEDs, respectively. It is worth highlighting that these values are an approximate for the real RC lifetime and only serve as a lower limit due to the nonlinearity of the devices. Based purely on these measurements, however, if the carrier lifetime is in fact found to be dominated by the RC lifetime (as the typical size of a standard LED is > 300×300 μm^2) when electrically injected, we would expect the *c-plane* LED to exhibit a faster decay time when measured on the time-resolved system. Figure 6-1c and d show the EL spectra of the two LEDs measured as a function of injection current for the semipolar LED and the *c-plane* LEDs, respectively. At 100 mA, both LEDs exhibit similar peak wavelengths of 507 nm and 514 nm for the semipolar LED and the *c-plane* LEDs, respectively. Due to the reduced QCSE, the emission wavelength shift of the semipolar LED is only 7 nm, compared with 40 nm from the *c-plane* LED when measured between 1 and 100 mA as shown in Figure 6-1e. Similarly, Figure 6-1f displays that the full width at half maximum (FWHM) of the semipolar LED experiences a 3 nm narrowing at injection current up to around 60 mA due to the naturally reduced polarisation and then broadens slightly at higher injection currents mainly due to band filling effects. In contrast, the *c-plane* LED experiences a 11 nm broadening between 1 and 100 mA due to QCSE and band filling effects. This has been often observed in III-nitride *c-plane* LEDs.
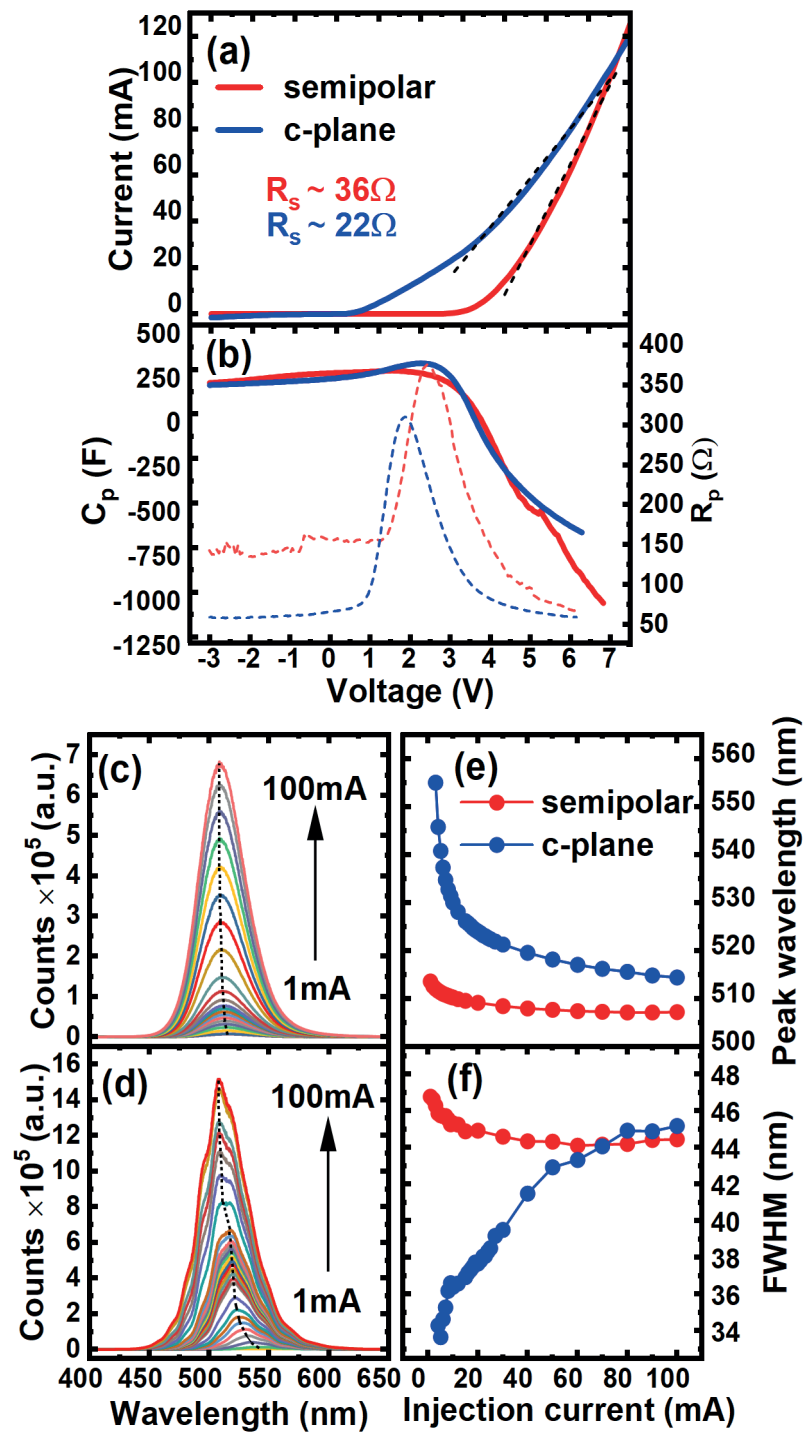
Figure 6-1 (a) Electrical and optical characteristics of the semipolar LED and the *c-plane* LED: I-V curves and series resistance; (b) capacitance (solid) and resistance (dashed) measured using an LCR meter in a parallel circuit mode at 1 MHz; (c) EL spectra of the semipolar LED as a function of injection current ; (d) EL spectra of the *c-plane* LED as a function of injection currents; (e) peak wavelength shift of both LEDs as a function of injection current, (f) FWHM of the EL spectra of the both LEDs as a function of injection current.

Figure 6-2a shows the results of TRPL measurements performed on both samples measured at room temperature. A bi-exponential model is typically employed to fit the decay trace of InGaN, namely, a fast and slow exponential component to fit the decay traces.[2-4,29,30] This behaviour is usually due to two radiative recombination channels contributing the decay. The exciton binding energy of GaN is large (> 26 meV), meaning that room temperature excitons and carrier localisation effects are the main factors contributing towards the bi-exponential nature of the decay.[31-33] The extracted lifetimes from the TRPL data are 0.44 ns and 1.3 ns for τ_1 and 1.2 ns and 6.3 ns for τ_2 corresponding to the semipolar and *c-plane* LEDs, respectively. It is clear that the semipolar LED exhibits much faster lifetimes for both fast and slow components which are attributed to a reduction in QCSE, allowing an enhanced recombination rate. However, for VLC applications which require fast LED switching speeds under electrical injection, TRPL results are not enough to confirm high performance, as TRPL neglects carrier transport effects through the LED structure. We therefore extend this measurement further by electrically injecting the device and observing the electroluminescence decay dynamics over time. Figure 6-2b and Figure 6-2c show the results of TREL decay traces of the two LEDs both measured at room temperature, which will be discussed later on.
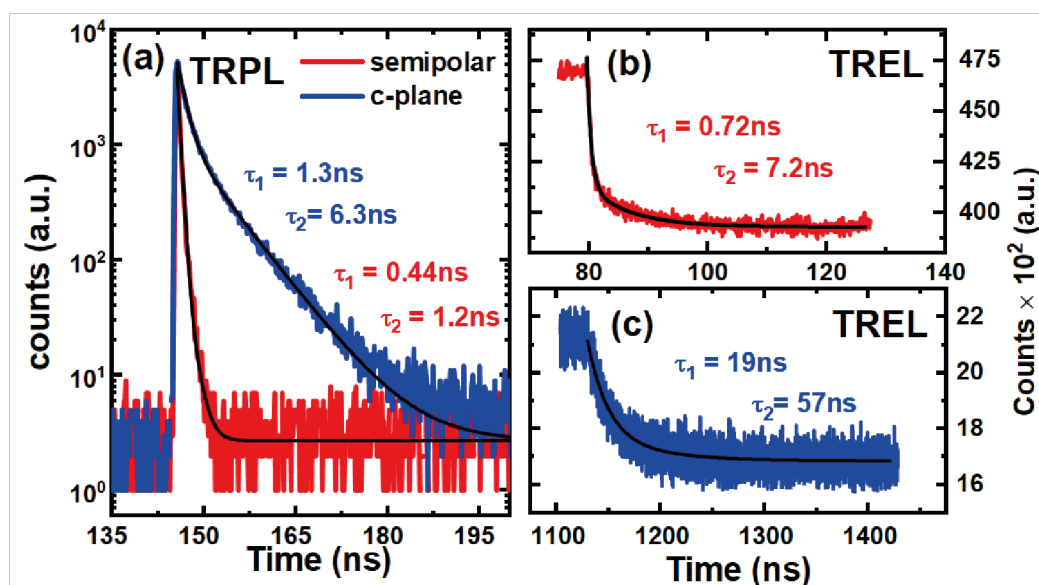
Figure 6-2 TRPL decay traces and fitting with a bi-exponential model showing extracted lifetimes for both the semipolar LED and the *c-plane* LED. (a); TREL decay traces for the semipolar LED (b) and c-plane (c) LED with the same bi-exponential model applied with associated extracted lifetimes. The corresponding amplitude coefficients are (a) $A_1 = 3954$, $A_2 = 1175$ and $A_1 = 4467$, $A_2 = 159$ for the c-plane and semipolar LED respectively. (b) $A_1 = 5454$, $A_2 = 950$ and (c) $A_1 = 341$, $A_2 = 99$.

Figure 6-3a shows the experimental setup for our TREL system. Figure 6-3b shows a typical example for an electrical input waveform generated by an AWG as an excitation source and the resulting histogram waveform acquired over time from a PMT detector displaying the LED recombination dynamics. For the semipolar LED, a 500 mV (peak-to-peak) waveform with a repetition rate of 10 MHz (100 ns) is used as an excitation source while an identical but less frequent 1MHz (1000 ns) source is used for the *c-plane* LED. The modulation voltage drop across the device is slightly lower due to the series resistance of both LEDs being less than the system impedance of 50 Ω. The lower frequency for the *c-plane* LED is necessary for the device to reach a steady state before measuring decay dynamics. In any time-resolved system, the instrument response function (IRF) needs to be taken into consideration. Since it is very difficult to directly measure the IRF of a system such as this which takes both the electrical and optical side into account simultaneously (this would require a probe-able, electrically injected emitter operating at > 500 nm with picosecond response times), we outline the response times of each major component in the system in Table 6-1 which should serve as a good approximation of the IRF. The IRF is approximated to be ~67 ps calculated using the sum of the squares of each of the component's response time.

Figure 6-3 Schematic of our TREL system (a); and typical electrical input signal (red) from an AWG measured on an RF oscilloscope and measured output (blue) from A PMT (b).

Table 6-1 Response time of each component of our TREL system to estimate the instrument response function (IRF). Data taken from equipment datasheets.

Component	Response time (ps)
AWG	22
Bias Tee	30
TCSPC electronics	6.5
RF probe	25
PMT	<50
RF cables	38

Figure 6-2b and Figure 6-2c show the TREL traces of the two LEDs and their corresponding fitting results for a typical waveform biased at 50 mA for both LEDs. Initially, a bi-exponential model as we used for TRPL was employed to fit the decay curves of both LEDs, aiming to approximately compare the two types of measurements. In this case, the extracted lifetimes from the TREL data are 0.72 ns and 19 ns for τ_1 and 7.2 ns and 57 ns for τ_2 corresponding to the semipolar LED and the *c-plane* LEDs, respectively. This direct comparison shows that there are much larger differences between the two LEDs compared to TRPL, with the semipolar LED experiencing similar but slightly higher lifetimes than on TRPL and the *c-plane* LED showing much higher lifetimes. In addition to the bi-exponential behaviour commonly observed in InGaN photoluminescence decay stemming from different radiative recombination channels such as excitonic contributions and carrier localization, a slower third term encompassing various carrier transport related recombination in the cladding and barrier layers, defects and junction capacitance-related effects is added. These mechanisms governing the third term are conceptualised in Figure 6-4.
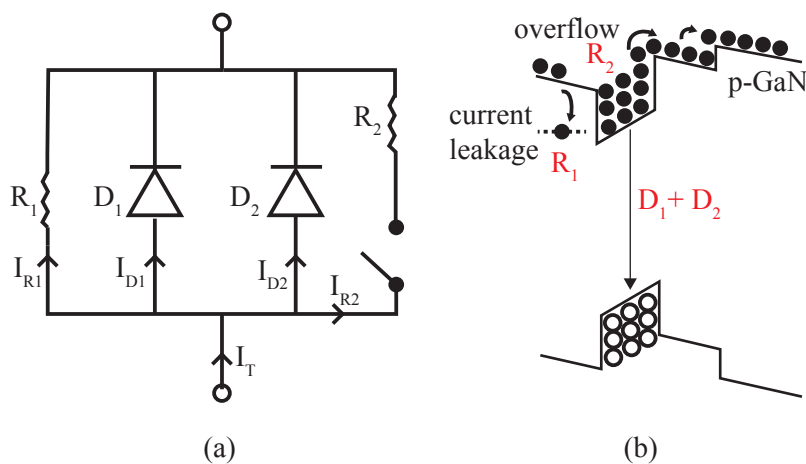
Figure 6-4 Transport effect concept. (a) Equivalent circuit showing four possible current paths and (b) band diagram with carrier dynamic mechanisms.

The circuit is based on a report by Masui et al which aims to model the differences between EL and PL results for InGaN/GaN LEDs[34]. The model assumes four main current paths for the LED: current leakage, radiative, non-radiative and carrier overflow. Resistor 1 (R_1) represents current leakage due to crystal defects, surface defects, traps etc… and is expected to be relatively large as the leakage current in the semipolar LEDs is low. Diode 1 (D_1) considers current flow due to radiative recombination only, and conversely Diode 2 (D_2) represents current flow due to non-radiative recombination such as SRH and Auger recombination. Finally, Resistor 2 (R_2) represents carrier overflow. A switch is introduced for this branch as a specific voltage is needed for carrier overflow to take place i.e., to overcome the QW barrier potential. These carrier transport mechanisms into and out of the active region could be potential reasons for the third term in the EL decay of the semipolar LED compared with the PL decay.

Figure 6-5a and b show the TREL traces of the semipolar LED measured under high and low injection current at room temperature, respectively, where a tri-exponential fitting given as below is used for each dataset.

$$y = A_1 e^{\frac{-t}{\tau_1}} + A_2 e^{\frac{-t}{\tau_2}} + A_3 e^{\frac{-t}{\tau_3}}, \tag{6-2}$$

where τ_1, τ_2 and τ_3 refer to the fastest, fast and slow components along with their corresponding amplitude coefficients A_1, A_2 and A_3, respectively. Each dataset comprises of different DC biases ranging from 50 µA to 100 mA, the effect of this DC bias is apparent when observing the baseline counts for each curve. A 500 mV excitation source is added on top of each DC bias using a bias tee so that we can measure recombination dynamics from a steady state as a function of injection current. Between 50 and 200 µA the LED does not reach a steady state and exhibits extremely fast fall times after the excitation source from the AWG is switched off. This may be due to the excitation source being comparatively much larger than the DC bias level resulting in the excitation source negatively biasing the device and briefly creating an artificial current shaping circuit that introduces other dominant recombination mechanisms such as carrier sweep out, exceeding the response time of the system. Therefore, under very low injection current these mechanisms are out of the scope of this study.
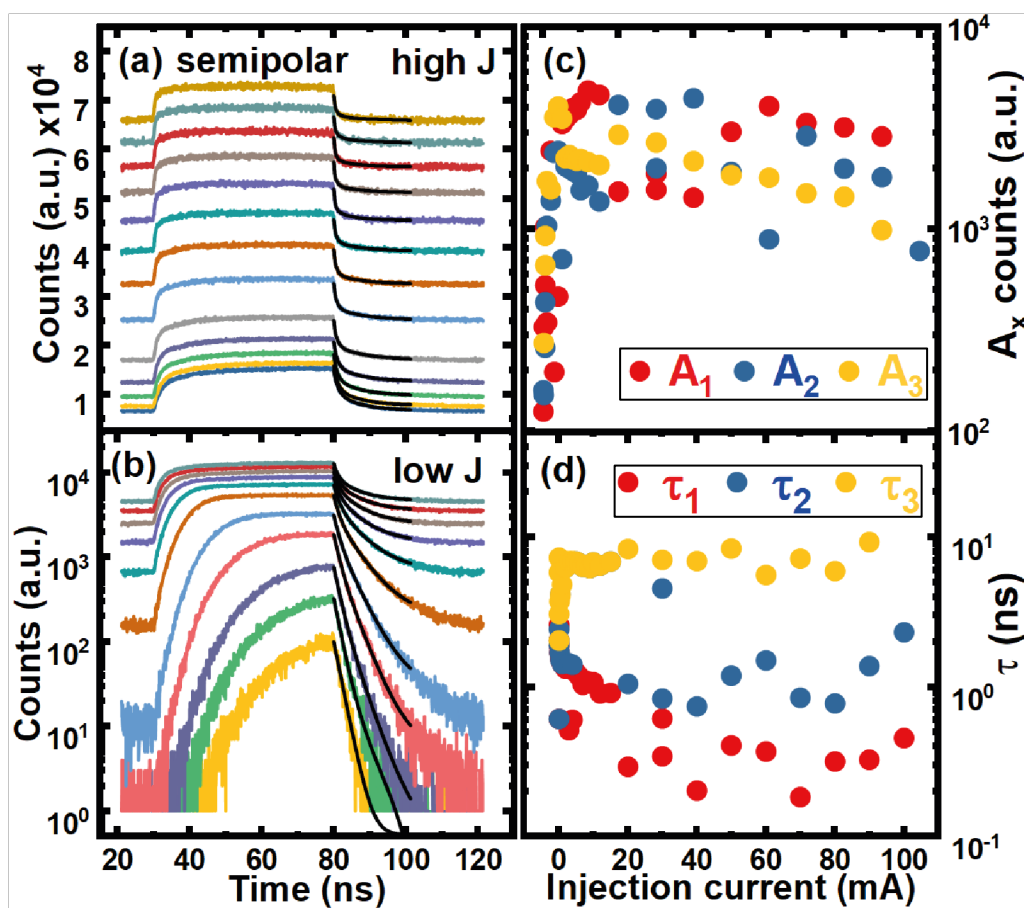
Figure 6-5 TREL decay traces as a function of injection current for the semipolar LED at high injection (a) and low injection (b). Tri-exponential model fitted to the decay profiles with corresponding amplitudes (c) and extracted time constants (d) as a function of injection current.

Figure 6-5c and d show the extracted lifetimes of the semipolar LED obtained using the tri-exponential model. Above 3 mA, there are three clear lifetimes associated with the EL decay of the semipolar LED. In general, τ_1, τ_2 and τ_3 decrease with increasing injection current as expected since increasing current density increases the recombination rate and thus the decreases the carrier lifetime. τ_3, the slowest component, seems to be the most dominant lifetime at lower injection current but then slowly decreases in its contribution with increasing current as indicated by Figure 6-5d. At higher injection, τ_1 becomes the most dominant component followed closely by τ_2 and then τ_3. For example, at 50 mA the extracted lifetimes are 0.40 ns, 1.2 ns and 8.3 ns for τ_1, τ_2 and τ_3 respectively. The extracted lifetimes for τ_1 and τ_2 are of the same magnitude as those obtained from the TRPL measurements and comparable to other published data on semipolar LEDs.[12,36]. This suggests that this device is not limited by RC effects. The extracted lifetime τ_3 is responsible for carrier transport effects as it is comparable with the LCR meter measurement, i.e., the approximation for the RC lifetime.
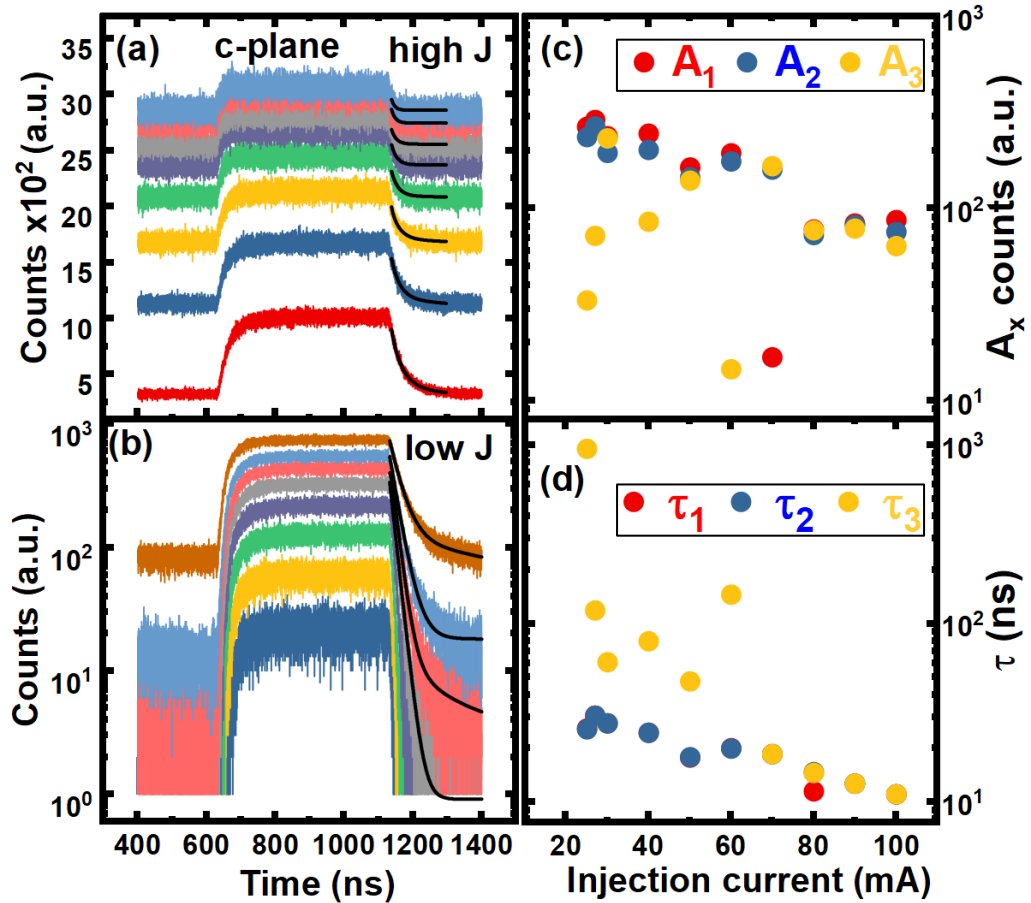
Figure 6-6 : TREL decay traces as a function of injection current for the *c-plane* LED at
high injection (a) and low injection (b). Tri-exponential model fitted to the decay profiles
with corresponding amplitudes (c) and extracted time constants (d) as a function of
injection current.

Figure 6-6a and b show results obtained by applying the same tri-exponential model to the *c-plane* LED in under high and low injection, respectively. τ_1 and τ_2 converge towards a single lifetime to around 12 ns below 60mA, while τ_3 is a much slower component, exhibiting between 0.1 and 1 µs as shown in Figure 6-6d. At higher injection, all three lifetimes converge towards a single lifetime i.e., a mono-exponential decay, slowly decreasing to 10 ns at 100 mA. LEDs which typically experience a mono-exponential decay are essentially like an RC circuit, since the fall time is limited by transport effects. Interestingly, the RC characteristics measured on this device would suggest that the *c-plane* LED should perform better than the semipolar LED when measuring dynamics. This clearly is not the case, and the reduction in QCSE present on the semipolar LED has a much more dominant effect on the recombination lifetime and resulting decay dynamics than the RC measurements which are expected to be the dominant lifetime with LEDs of this size.

6.4   Summary

We have demonstrated the importance of using TREL measurements over TRPL measurements for VLC applications, as it is impossible to use TRPL to study transport effects

through a LED structure. A detailed comparison study has been conducted by performing TREL and TRPL on a semipolar LED and a *c-plane* LED both with an emission wavelength in the green spectral region. By performing TREL measurements under bias conditions, the transport effect on carrier lifetime has been studied. The semipolar LED was found to follow closely to a tri-exponential decay, with differential carrier lifetimes τ_1, τ_2 contributing towards radiative and non-radiative recombination and τ_3 encapsulating transport effects while the *c-plane* LED was reduced to a mono-exponential decay, indicating τ_{RC} being a limiting factor.

6.5   References

(1)   Haas, H. LiFi Is a Paradigm-Shifting 5G Technology. *Rev. Phys.* **2018**, 3, 26–31.

(2)   Minsky, M. S.; Fleischer, S. B.; Abare, A. C.; Bowers, J. E.; Hu, E. L.; Keller, S.; Denbaars, S. P. Characterization of High-Quality InGaN/GaN Multiquantum Wells with Time-Resolved Photoluminescence. *Appl. Phys. Lett.* **1998**, 72, 1066–1068.

(3)   Okur, S.; Nami, M.; Rishinaramangalam, A. K.; Oh, S. H.; DenBaars, S. P.; Liu, S.; Brener, I.; Feezell, D. F. Internal Quantum Efficiency and Carrier Dynamics in Semipolar (20 21) InGaN/GaN Light-Emitting Diodes. *Opt. Express* **2017**, *25* (3), 2178–2186.

(4)   Kur, S. E. O.; Ami, M. O. N.; Ishinaramangalam, A. S. K. R.; Ang, S. H. O. H.; Aars, S. T. P. D. E. N. B.; Iu, S. H. L.; Rener, I. G. A. L. B.; Eezell, D. A. F. F. Internal quantum efficiency and carrier dynamics in semipolar (20-2-1) InGaN/GaN light-emitting diodes. *Opt. Express*, **2017**, 25, 2178–2186.

(5)   Kim, H.; Shin, D.-S.; Ryu, H.-Y.; Shim, J.-I. Analysis of Time-Resolved Photoluminescence of InGaN Quantum Wells Using the Carrier Rate Equation. *Jpn. J. Appl. Phys.* **2010**, 49, 112402.

(6)   Sufyan Islim, M.; Ferreira, R. X.; He, X.; Xie, E.; Videv, S.; Viola, S.; Watson, S.; Bamiedakis, N.; Penty, R. V; White, I. H.; Kelly, A. E.; Gu, E.; Haas, H.; Dawson, M. D. Towards 10 Gb/s Orthogonal Frequency Division Multiplexing-Based Visible Light Communication Using a GaN Violet Micro-LED. *Photonics Res.* **2017**, 5, A35-A43

(7)   Tsonev, D.; Chun, H.; Rajbhandari, S.; Mckendry, J. J. D.; Videv, S.; Gu, E.; Haji, M.; Watson, S.; Kelly, A. E.; Faulkner, G.; Dawson, M. D.; Haas, H.; O'brien, D. A 3-Gb/s Single-LED OFDM-Based Wireless VLC Link Using a Gallium Nitride µLED. *IEEE Photon. Technol. Lett.* **2014**, 26, 637-640

(8)   Xie, E.; Bian, R.; He, X.; Islim, M. S.; Chen, C.; Mckendry, J. J. D.; Gu, E.; Haas, H.; Dawson, M. D. Over 10 Gbps VLC for Long-Distance Applications Using a GaN-Based Series-Biased Micro-LED Array. *IEEE Photonics Technol. Lett.* **2020**, 32, 499–502.

(9)   Gong, Z.; Jin, S.; Chen, Y.; McKendry, J.; Massoubre, D.; Watson, I. M.; Gu, E.; Dawson, M. D. Size-Dependent Light Output, Spectral Shift, and Self-Heating of 400 Nm InGaN Light-Emitting Diodes. *J. Appl. Phys.* **2010**, 107, 013103

(10)   Ji, Y.; Liu, W.; Erdem, T.; Chen, R.; Tiam Tan, S.; Zhang, Z. H.; Ju, Z.; Zhang, X.; Sun, H.; Sun, X. W.; Zhao, Y.; Denbaars, S. P.; Nakamura, S.; Volkan Demir, H. Comparative Study of Field-Dependent Carrier Dynamics and Emission Kinetics of InGaN/GaN Light-Emitting Diodes Grown on (11 2¯ 2) Semipolar versus (0001) Polar Planes. *Appl. Phys. Lett.* **2014**, *104* (14).

(11)   Su, Z. C.; Xu, S. J. Effective Lifetimes of Minority Carriers in Time-Resolved Photocurrent and Photoluminescence of a Doped Semiconductor: Modelling of a GaInP Solar Cell. *Sol. Energy Mater. Sol. Cells* **2019**, 193, 292–297

(12)   Haggar, J. I.; Cai, Y.; Ghataora, S. S.; Smith, R. M.; Bai, J.; Wang, T. High Modulation Bandwidth of Semipolar (11–22) InGaN/GaN LEDs with Long Wavelength Emission. *ACS Appl. Electron. Mater.* **2020**, 2, 2363–2368

(13)   Rashidi, A.; Nami, M.; Monavarian, M.; Aragon, A.; DaVico, K.; Ayoub, F.; Mishkat-Ul-Masabih, S.; Rishinaramangalam, A.; Feezell, D. Differential Carrier Lifetime and Transport Effects in Electrically Injected III-Nitride Light-Emitting Diodes. *J. Appl. Phys.* **2017**, 122, 035706.

(14)   David, A.; Hurni, C. A.; Young, N. G.; Craven, M. D. Carrier Dynamics and

Coulomb-Enhanced Capture in III-Nitride Quantum Heterostructures. *Appl. Phys. Lett.* **2016**, 109, 33504.

(15) Esquivias, I.; Weisser, S.; Romero, B.; Ralston, J. D.; Rosenzweig, J. Carrier Dynamics and Microwave Characteristics of GaAs-Based Quantum-Well Lasers. *IEEE J. Quantum Electron.* **1999**, 35, 635–646.

(16) Weisser, S.; Esquivias, I.; Tasker, P. J.; Ralston, J. D.; Romero, B.; Rosenzweig, J. Impedance Characteristics of Quantum-Well Lasers. *IEEE Photonics Technol. Lett.* **1994**, 6, 1421–1423.

(17) Rashidi, A.; Monavarian, M.; Aragon, A.; Feezell, D. Exclusion of Injection Efficiency as the Primary Cause of Efficiency Droop in Semipolar (20-2-1) InGaN/GaN Light-Emitting Diodes. *Appl. Phys. Lett.* **2018**, 113, 031101.

(18) Viola, S.; Islim, M. S.; Watson, S.; Videv, S.; Haas, H.; Kelly, A. E. 15 Gb/s OFDM-Based VLC Using Direct Modulation of 450 GaN Laser Diode. Proceedings 10437, *Advanced Free-Space Optical Communication Techniques and Applications III*, **2017**, 104370E.

(19) Lee, C.; Zhang, C.; Cantore, M.; Farrell, R.; Oh, S. H.; Margalith, T.; Speck, J. S.; Nakamura, S.; Bowers, J. E.; DenBaars, S. P. 2.6 GHz High-Speed Visible Light Communication of 450 Nm GaN Laser Diode by Direct Modulation. *IEEE Summer Topicals Meeting Series*, **2015**, 112–113.

(20) Chi, Y.-C.; Hsieh, D.-H.; Tsai, C.-T.; Chen, H.-Y.; Kuo, H.-C.; Lin, G.-R. 450-Nm GaN Laser Diode Enables High-Speed Visible Light Communication with 9-Gbps QAM-OFDM. *Opt. Express* **2015**, 23, 13051–13059.

(21) Bernardini, F.; Fiorentini, V.; Vanderbilt, D. Spontaneous Polarization and Piezoelectric Constants of III-V Nitrides. *Phys. Rev. B*, **1997**, 56, R10024.

(22) Takeuchi, T.; Amano, H.; Akasaki, I. Theoretical Study of Orientation Dependence of Piezoelectric Effects in Wurtzite Strained GaInN/GaN Heterostructures and Quantum Wells. *Jpn. J. Appl. Phys.* **2000**, 39, 413–416.

(23) Wang, S. W.; Chen, F.; Liang, L.; He, S.; Wang, Y.; Chen, X.; Lu, W. A High-Performance Blue Filter for a White-Led-Based Visible Light Communication System. *IEEE Wirel. Commun.* **2015**, 22, 61–67.

(24) Northrup, J. E. GaN and InGaN (11-22) Surfaces: Group-III Adlayers and Indium Incorporation. *Appl. Phys. Lett.* **2009**, 95, 133107.

(25) Wang, T. Topical Review: Development of Overgrown Semi-Polar GaN for High Efficiency Green/Yellow Emission. *Semicond. Sci. Technol.* **2016**, 31, 093003

(26) Haggar, J. I. H.; Cai, Y.; Bai, J.; Ghataora, S.; Wang, T. "Long-Wavelength Semipolar (11–22) InGaN/GaN LEDs with Multi-Gb/s Data Transmission Rates for VLC". *ACS Appl. Electron. Mater.* **2021**, 3, 4236–4242.

(27) Bai, J.; Xu, B.; Guzman, F. G.; Xing, K.; Gong, Y.; Hou, Y.; Wang, T. (11-22) semipolar InGaN emitters from green to amber on overgrown GaN on micro-rod templates. *Appl. Phys. Lett.* **2015**, 107, 261103.

(28) Schubert, E. F. Light-Emitting Diodes. Cambridge University Press (3rd edition), **2018**

(29) Kawakami, Y.; Suzuki, S.; Kaneta, A.; Funato, M.; Kikuchi, A.; Kishino, K. Origin of High Oscillator Strength in Green-Emitting InGaN⁄GaN Nanocolumns. *Appl. Phys. Lett.* **2006**, 89, 163124.

(30) Liu, B.; Smith, R.; Athanasiou, M.; Yu, X.; Bai, J.; Wang, T. Temporally and Spatially Resolved Photoluminescence Investigation of (1122) Semi-Polar

InGaN/GaN Multiple Quantum Wells Grown on Nanorod Templates. *Appl. Phys. Lett.* **2014**, 105, 261103.

(31)   Chen, S.-W. H.; Huang, Y.-M.; Chang, Y.-H.; Lin, Y.; Liou, F.-J.; Hsu, Y.-C.; Song, J.; Choi, J.; Chow, C.-W.; Lin, C.-C.; Horng, R.-H.; Chen, Z.; Han, J.; Wu, T.; Kuo, H.-C. High-Bandwidth Green Semipolar (20–21) InGaN/GaN Micro Light-Emitting Diodes for Visible Light Communication. *ACS Photonics* **2020**, 7, 2228–2235

(32)   Bhattacharya, P.; Frost, T.; Deshpande, S.; Baten, M. Z.; Hazari, A.; Das, A. Room Temperature Electrically Injected Polariton Laser. *Phys. Rev. Lett.* **2014**, 112, 29–31

(33)   Feng, S. W.; Cheng, Y. C.; Liao, C. C.; Chung, Y. Y.; Liu, C. W.; Yang, C. C.; Lin, Y. S.; Ma, K. J.; Chyi, J. I. Two-Component Photoluminescence Decay in InGaN/GaN Multiple Quantum Well Structures. *Phys. Status Solidi (A)*, **2001**, 228, 121–124.

(34)   Masui, H.; Ive, T.; Schmidt, M. C.; Fellows, N. N.; Sato, H.; Asamizu, H.; Nakamura, S.; DenBaars, S. P. Equivalent-Circuit Analysis for the Electroluminescence-Efficiency Problem of InGaN/GaN Light-Emitting Diodes. *Jpn. J. Appl. Phys.* **2008**, *47* (4 PART 1), 2112–2118.

(35)   Monavarian, M.; Rashidi, A.; Aragon, A. A.; Oh, S. H.; Rishinaramangalam, A. K.; DenBaars, S. P.; Feezell, D. Impact of Crystal Orientation on the Modulation Bandwidth of InGaN/GaN Light-Emitting Diodes. *Appl. Phys. Lett.* **2018**, 112, 041104

(36)   Zhang, Y.; Smith, R. M.; Hou, Y.; Xu, B.; Gong, Y.; Bai, J.; Wang, T. Stokes Shift in Semi-polar (11-22) InGaN/GaN Multiple Quantum Wells, *Appl. Phys. Lett.* **2016**, 108, 031108

Chapter 7: HEMT driven microLEDs and semipolar based microLEDs for visible light communications

In previous chapters, research was focussed on the viability of semipolar light emitting diodes (LEDs) with a broad area for visible light communications (VLC). In parallel to this, microLEDs offer high modulation bandwidths when driven at high current densities. As explained in previous chapters however, microLEDs suffer from low efficiencies partly due to etching induced sidewall damage, which deteriorates further with decreasing LED diameter. In addition, since the microLEDs need to be injected with a high current density for high-frequency performance, conventional biasing methods through the pn-junction may not be sufficient or stable enough for long usage. In this chapter, we demonstrate an alternative method for the fabrication of microLEDs using a direct epitaxial approach which eliminates the need for dry etching and therefore any sidewall damage contributing to device performance degradation. We also directly grow the microLEDs on top of a AlGaN/GaN high-electron mobility transistor (HEMT) template, whereby LED emission is achieved by directly tuning its HEMT's gate voltage. As a result, we have demonstrated an epitaxial integration of monolithic on-chip 20 μm microLED-HEMT with a record modulation bandwidth of 1.2 GHz when measured on our high-frequency setup.

7.1 Introduction

VLC is expected to be a complementary technology to the upcoming 5G infrastructure where current lower frequency radio frequency (RF) technology does not work such as in hospitals, schools, underwater communications etc[1]. The modulation bandwidth of current solid state lighting (SSL) technology is the crucial barrier which restricts the implementation of VLC today. In general, the LED modulation bandwidth is determined by the larger of the resistance-capacitance (RC) time constant (derived from device geometry and parasitics) and the carrier recombination lifetime. If we consider a typical blue InGaN/GaN multiple quantum well (MQW) LED with a 100 nm active region, the RC time constant can be estimated using Equation 7-1:

$$RC = R(\frac{\varepsilon\varepsilon_0 A}{L})$$

(7-1)

where R is the electrical impedance, A is the LED area, L can be estimated as the active region thickness, ε is the GaN dielectric constant (i.e., around 9) and ε_0 is the vacuum permittivity. Equation 7-1 suggests that the RC time constant reduces with a smaller LED

area. Assuming an impedance of 50 Ω, reducing the LED area from a standard sized 330 × 330 μm^2 to π10^2 μm^2 (for a 20 μm diameter circular LED) corresponds to an RC time constant of 10ns and 0.05ns for the larger and smaller sizes, respectively. As a result, the modulation bandwidth (~1/2πRC) increases to > 10 GHz for a 20 μm microLED.

This calculation however assumes the carrier recombination lifetime of the LED is less than 0.05 ns, which is not the case for commercially available blue LEDs which are on the order of 10 ns under normal operating conditions. For microLEDs, efforts are therefore targeted towards improving the carrier lifetime of the LEDs which currently dominates the overall modulation bandwidth over the RC time constant. Driving the LED at a very high current density on the order of kA/cm^2 is a simple solution to improving the carrier lifetime. In order to do this for extended periods of time however, the microLED quality is essential. Conventional methods of III-nitride microLED device fabrication involve dry-etching techniques[2–6] which unavoidably introduce significant etching induced sidewall damage. These damages dramatically reduce device performance and introduce many problems when driving the microLEDs at higher current densities which is a requirement for VLC[7,8]. Even worse so, this effect is significantly enhanced when reducing the LED dimension below 20 μm[9–11]. In recent work, evidence suggests microLEDs typically exhibit a lower EQE than broader area LEDs with diameters exceeding 100 μm[12,13]. Advanced atomic layer deposition (ALD) techniques have been recently used for surface passivation to reduce sidewall damages but the improvements however are minimal[14,15]. Using traditional dry-etching methods therefore will make fabrication of micro-LEDs with high performance extremely difficult to produce. Etching induced sidewall damages may be one of the fundamental reasons the modulation bandwidth of microLEDs on industry compatible c-plane substrates is currently limited to 1 GHz.

In addition to sidewall issues, another problem arises when driving the LEDs at high current densities which is needed for VLC. For general SSL applications, LEDs need not be driven beyond 10 A/cm^2 and as a result stable operation is possible across the p and n layers. For *c-plane* LEDs suited for VLC applications however, current densities on the order of kA/cm^2 is needed for high frequency performance[5,16] and in this case, conventionally biasing the devices across their PN junction may not be good enough. To address these issues, we propose to integrate an AlGaN/GaN HEMT and a microLED together. The biasing methods for a standard LED is shown in Figure 7-1a and for our proposed HEMT-LED in Figure 7-1b. For a conventional LED, when driven at high current densities a small change in forward voltage results in a significant change in injection current density which is very difficult to

control. Conversely, for a HEMT-LED the injection current into the LED can be easily controlled by simply tuning the gate voltage of its HEMT. As the HEMT epi structure is grown before the LED structure, the integration is known as LED-on-HEMT. Another configuration is HEMT-on-LED, whereby a HEMT epi structure is grown on top of the LED p-i-n structure and is subsequently etched down to n-GaN to separate the two devices as reported in other work[17]. Each configuration has its pros and cons, for example the LED-on-HEMT structure demonstrated here has the advantage of easily creating a connection between the cathode of the LED and the source/drain of the HEMT. However, in this configuration the LED device quality may suffer when grown on a HEMT epi rather than conventional sapphire substrates and buffer layers. The HEMT-on-LED configuration would have the advantage of not affecting the LED performance, but the metal connection tracks have to span the entire thickness of the LED and HEMT, possibly resulting in packaging and scaling issues when considered for high resolution display and VLC applications.
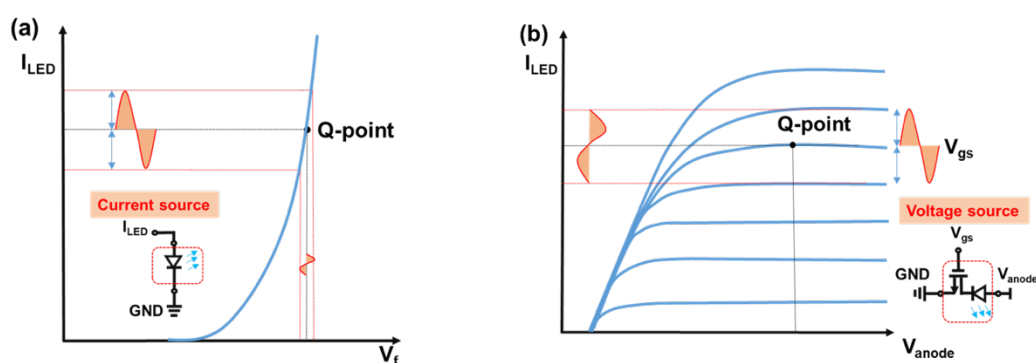
Figure 7-1 Conventional biasing method across the LED PN junction (a) and our proposed method of biasing the LED by tuning its HEMT's gate voltage (b).

7.2   Growth

Recently, our group has demonstrated a direct epitaxial approach to achieving ultra-small microLEDs with a record external quantum efficiency (EQE)[18,19]. Using SiO_2 masks on n-GaN to form micro-hole array templates, microLEDs form naturally inside the micro-hole arrays without the need of any dry-etching processes and therefore eliminate any sidewall damage. Here we extend this growth method further by forming the SiO_2 masks on an AlGaN/GaN HEMT template with the purpose of achieving monolithically integrated single HEMT-microLED devices on industry compatible *c-plane* sapphire substrates.

The process of preparing our micro-hole arrays on our AlGaN/GaN HEMT template is shown in Figure 7-2. Firstly, a 500 nm layer of SiO_2 is deposited using plasma-enhanced chemical vapour deposition (PECVD). Photolithography processes are then used to develop the circular array on the SiO_2 before inductive-coupled plasma (ICP) on the SiO_2 to etch the micro-hole arrays. The diameter of each micro-hole is 20 µm with an edge-to-edge spacing

of adjacent micro-holes of 25 µm. Then, using the newly developed micro-holes as masks, ICP is used again to etch into the HEMT template within the micro-hole regions by ≥ 50 nm. As a result, the microLEDs will only grow in the selected micro-hole regions. The microLED structure is shown schematically in Figure 7-2c and is described as follows: a layer of n-GaN, 30 periods of $In_{0.05}Ga_{0.95}N$/GaN superlattices (SLS) as a pre-layer, 5 periods of $In_{0.25}Ga_{0.75}N$/GaN MQWs (well: 2.5 nm; barrier: 13 nm) as an active region, a 20 nm p-$Al_{0.20}Ga_{0.80}N$ electron blocking layer and finally a 150 nm p-GaN layer. Making sure the overgrown n-GaN of microLEDs contacts the AlGaN barrier and GaN buffer ensures that each single microLED is electrically connected to the HEMT through the two-dimensional electron gas (2DEG) formed between the barrier and buffer layers. Finally, 40% Hydrofluoric acid (HF) is used after LED overgrowth to remove the SiO_2 masks as shown in Figure 7-2d.
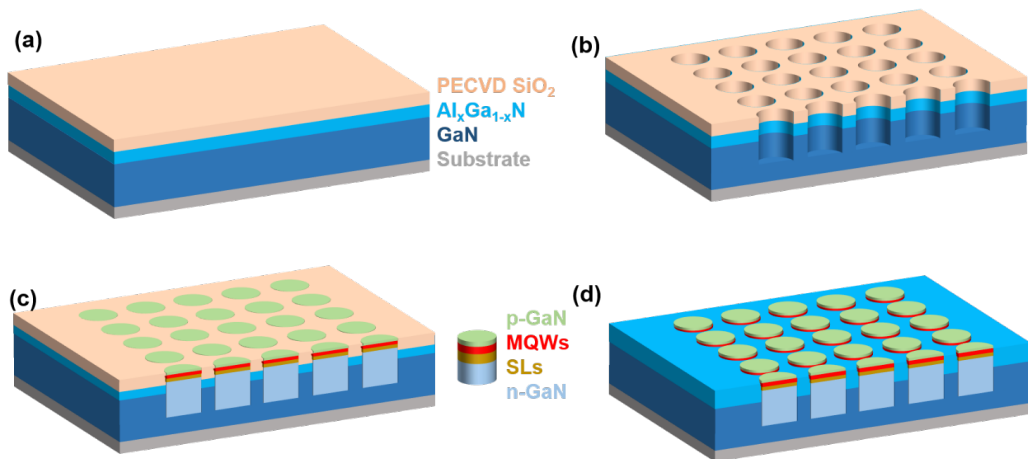
Figure 7-2 Process steps of micro-hole arrays on AlGaN/GaN template: layer of SiO_2 (a) after PECVD (b) after selective overgrowth of microLED arrays (c) removal of SiO_2 using HF.

A cross sectional scanning electron microscope (SEM) image of an overgrown 20 µm LED on our HEMT template is shown in Figure 7-3; clearly demonstrating the monolithic integration between the LED and HEMT. The LED protrudes slightly due to the removal of the SiO_2 layer.

Figure 7-3 SEM image of a 20 µm LED on our HEMT template.

7.3   Fabrication

The detailed fabrication process for the HEMT-microLEDs is shown in Figure 7-4 and is performed directly after using HF to remove the SiO_2 masks. Firstly, a photoresist mask is used to protect each individual microLED before using ICP to define the HEMT mesas (Figure 7-4a). Ti/Al/Ni/Au is then used as source contacts for the HEMT and is then annealed at 850°C in N_2 ambient for 30 seconds (Figure 7-4b). A Ni/Au transparent current spreading layer (CSL) is then deposited as the p-contact on top of each microLED mesa and subsequently annealed at 570°C in air ambient for 2 minutes (Figure 7-4c). The p-contact metal is formed using Ti/Ai/Ti/Au (Figure 7-4d), and Ni/Au deposited for the gate contact of the HEMT (Figure 7-4e). A 800nm layer of SU8-2 polymer is spin-coated onto the sample, patterned and then hard-baked to serve as a passivation layer (Figure 7-4f). Finally, connection metal tracks are deposited consisting of Ti/Al/Ti/Au for probing (Figure 7-4g).

(a) HEMT Mesa definition   (b) Source contact formation   (c) CSL formation

(d) Anode metal deposition   (e) Gate formation   (f) Passivation

(g) Bonding pad formation   (h) Top view of fabricated HEMT-microLED
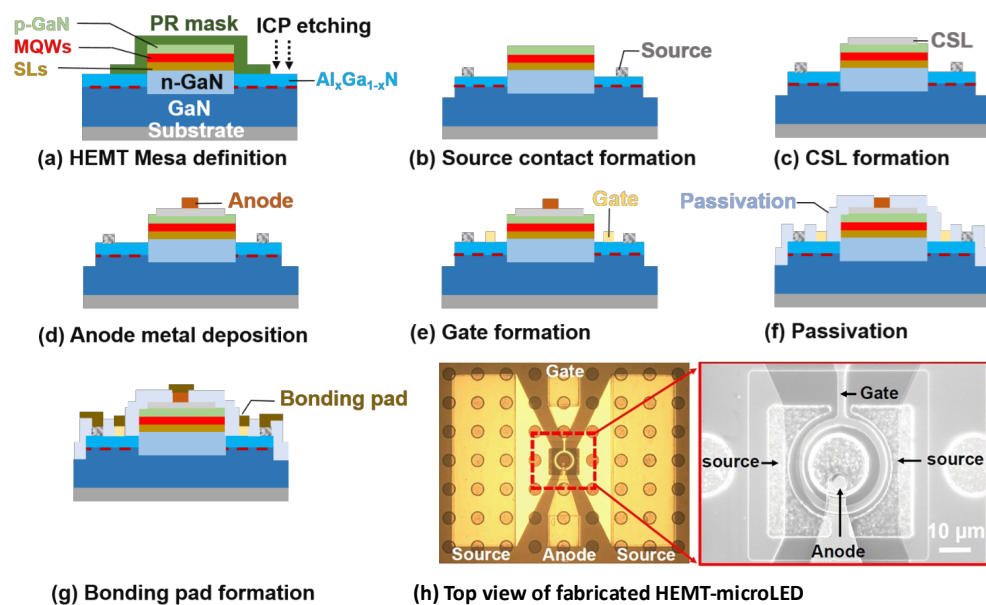
Figure 7-4 Fabrication process for attaching electrodes to microLED and HEMT.

A top-down view from an optical microscope of the fabricated HEMT-microLED is shown in Figure 7-4h with a zoomed in scanning electron microscopy (SEM) image displaying the circular gate of the HEMT surrounding the LED with length 2 µm, gate-to-source distance 2 µm and gate width 88 µm. The anode pad is shown more clearly in the SEM image, situated on top of the current spreading layer (CSL) of the microLED. A square shaped mesa is defined for the whole HEMT-microLED device with two semi-circular shaped pads placed on top acting as the source for the HEMT. Metal connection tracks travel to probing pads from the gate, anode, and source suitable for our high frequency ground-signal-ground (GSG) air coplanar probes with a centre-to-centre pitch of 100 µm.

7.4   HEMT-microLED characterisation setup

Our high-frequency setup described in Chapter 3 was modified in order for us to test a three terminal device such as our HEMT-microLEDs. Figure 7-5 shows our experimental setup capable of measuring HEMT-microLEDs up to a frequency of 1.4GHz which is limited by our fibre coupled photoreceiver. A two-channel source meter, with channel 1 connected to the gate of the HEMT-microLED via the DC port of a bias tee. Channel 2 is then used to supply a voltage to the anode on top of the HEMT-microLED mesa. The small signal from the VNA is connected to the gate voltage via the RF port on the same bias tee. The resulting modulated and/or unmodulated electroluminescence is collected through the microscope objective and delivered to either a spectrometer or a photodiode with an integrated transimpedance amplifier which rejects DC photocurrent. All measurements are then recorded onto a computer. As a result, the IV and transconductance characteristics, electroluminescence spectra and frequency response of the HEMT-microLED can be easily and accurately measured.
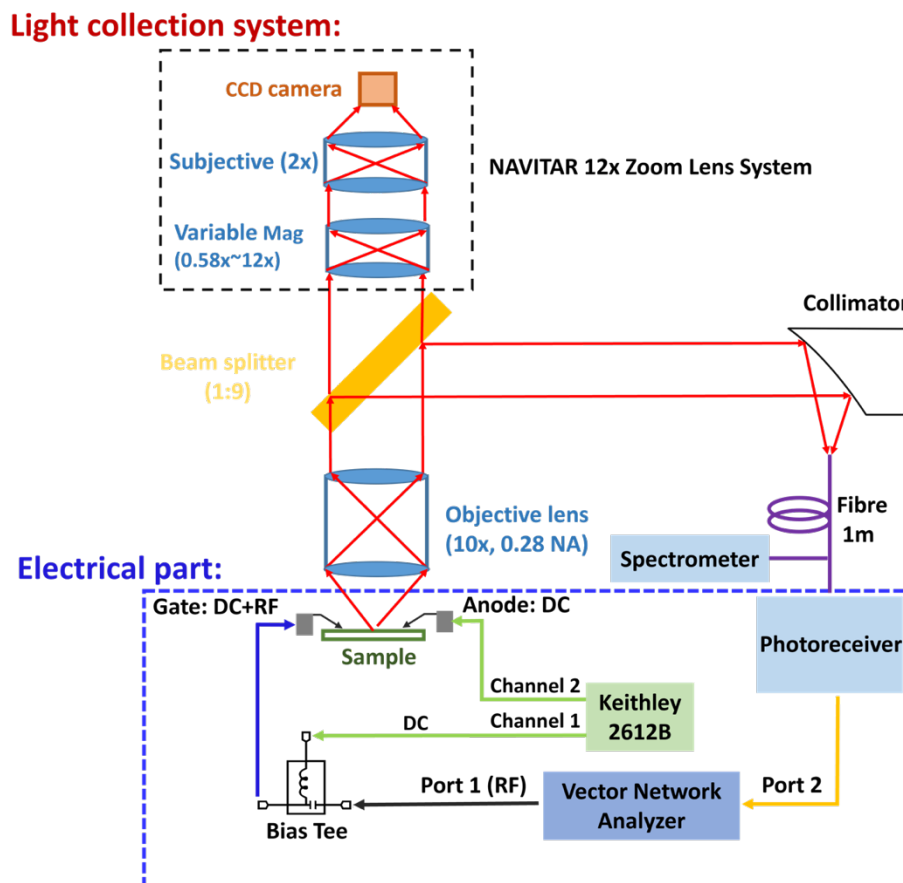
Figure 7-5 High-frequency characterisation system for HEMT-microLED showing electrical injection method and electroluminescence collection system.

7.5 Results and discussion

7.5.1 Electrical

A two-channel Keithley 2612B source meter was used for electrical measurements. Figure 7-6 shows the typical IV and transfer characteristics of the integrated HEMT-microLED where the injection current into the LED is carefully controlled by the HEMT device. Figure 7-6a shows the injection current into a single microLED as a function of anode voltage measured at different gate bias voltages from -1 to 7 volts which demonstrates typical HEMT characteristics. The mechanism of LED current supply is more clearly shown in the inset of Figure 7-6a, which shows the equivalent electrical circuit between the HEMT and microLED. The maximum current which the HEMT can provide to a single microLED is 45 mA, or ~ 14.3 kA/cm^2, indicating that our HEMT-microLED can sustain very high injection current densities whilst also confirming that the microLED is of high quality due to our novel overgrowth method.
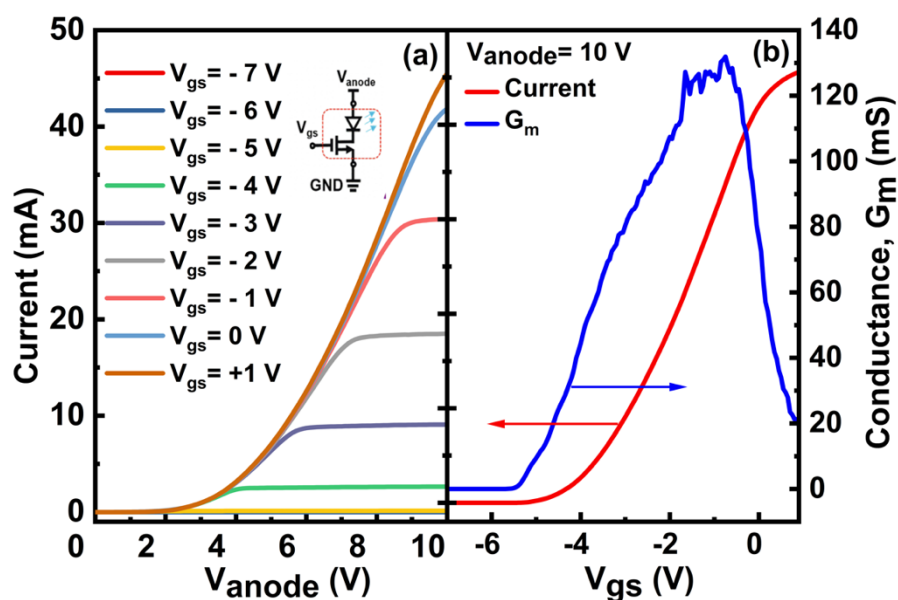
Figure 7-6 Typical IV characteristics of the HEMT-microLED with the electronic circuit as the inset (a) and the corresponding transfer characteristics (b).

Figure 7-6b shows typical transfer characteristics of our HEMT-microLED. The transconductance (G_m) is an electrical characteristic related to the change in input voltage across the gate of the microLED and the output current through the microLED. No current flows through the device with a gate voltage less than -5.4 V, after which the conductance increases rapidly. Our HEMT-microLED reaches a maximum transconductance of 132 mS at a gate voltage of -0.75 V and a fixed anode voltage of 10 V. The conductance sharply reduces after -0.75 V to around 20 mS at 1V gate bias; where a maximum output current of 45 mA is measured. Due to these characteristics, our monolithically integrated HEMT with

a microLED allows us to carefully control the LED injection current through small variations to gate voltages.

7.5.2   Optical

Figure 7-7a shows the electroluminescence spectra from a single HEMT-microLED as a function of gate bias. The peak shifts from 510 nm to 480 nm with increasing gate voltage and clearly demonstrates that the microLED injection current (and therefore intensity) can be easily tuned using the gate voltage. Figure 7-7b demonstrates the possible advantages of integrating a HEMT as a driving mechanism for an LED for VLC applications. Firstly, the HEMT-microLED is biased with a fixed anode voltage of 15V and then the gate bias is varied. The output power is measured using a Thorlabs PM100D power meter at each gate bias level. The gate electrode is then left unbiased, and the anode voltage is varied so that the injection current is determined by the voltage across the PN junction and not from the gate bias as is the case in conventional LED driving systems. Once again, the output power is measured at each anode voltage step, since there are no changes in the system when changing the biasing method then the measured output powers can be directly comparable. Comparing the normalised output powers in the linear regime i.e, 20-80% of max intensity (annotated boxes in Figure 7-7b) needs a voltage swing of 4.5 V for the conventional biasing method (without a gate bias) and only 2V when the injection current is determined by the gate bias. Therefore, in this case, a smaller modulation swing is needed for such devices to reach similar signal-to-noise ratio (SNR) levels for complex modulation schemes such as DC-biased optical orthogonal frequency division multiplexing (DCO-OFDM).
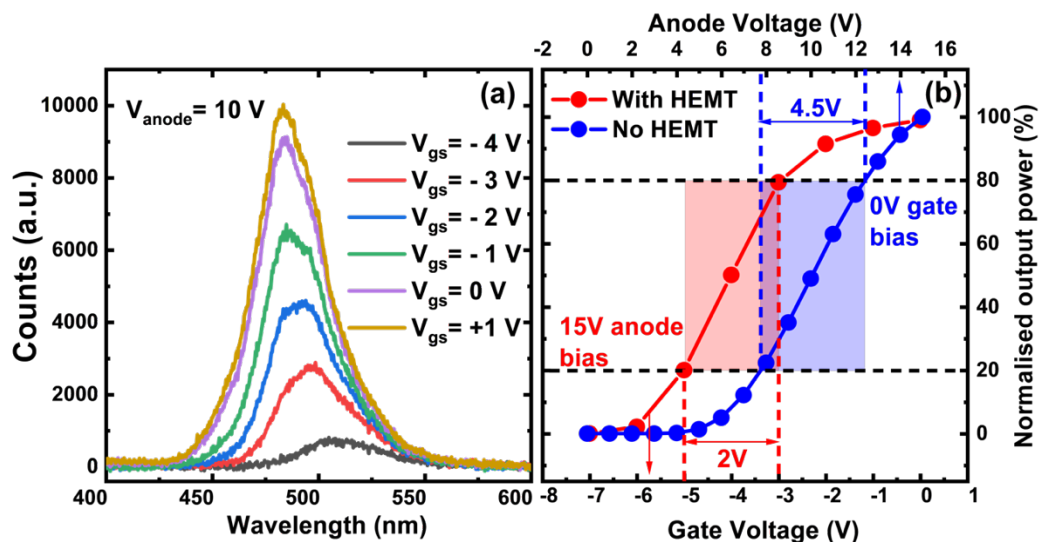
Figure 7-7 Electroluminescence (EL) spectra characteristics of HEMT-microLED measured at different gate voltages between -4 V and +1 V and a fixed anode voltage of 10 V (a). Measured light output power when biasing the LED with a HEMT (varying gate voltage) and without a HEMT (0 V gate bias) (b).

7.5.3   Frequency response

The frequency response of our single HEMT-microLED is shown in Figure 7-8a, i.e., the normalised output power as a function of frequency measured under different gate bias conditions. The resulting current densities at different gate bias levels are also shown. At 0 V gate bias, the HEMT-microLED exhibits a record breaking 1.2 GHz at 13.3kA/cm^2 which is close to the maximum bandwidth achievable with this system. In addition, the small variations in gate bias from -4 to 0 volts, results in a 12.5 kA/cm^2 and 954 MHz difference in current density and modulation bandwidth, respectively suggesting that small RF powers are needed to modulate the LED sufficiently for VLC applications such as DCO-OFDM where large modulations in light intensity are necessary to maximise the SNR at the receiver. Figure 7-8b shows a CCD view of our HEMT-microLED emitting strong cyan electroluminescence with annotations showing gate/anode injection methods to measure the frequency response. Table 7-1 compares this work to other state-of-the-art devices for VLC applications which clearly demonstrates the benefits of monolithic integration[4,5,20-24].
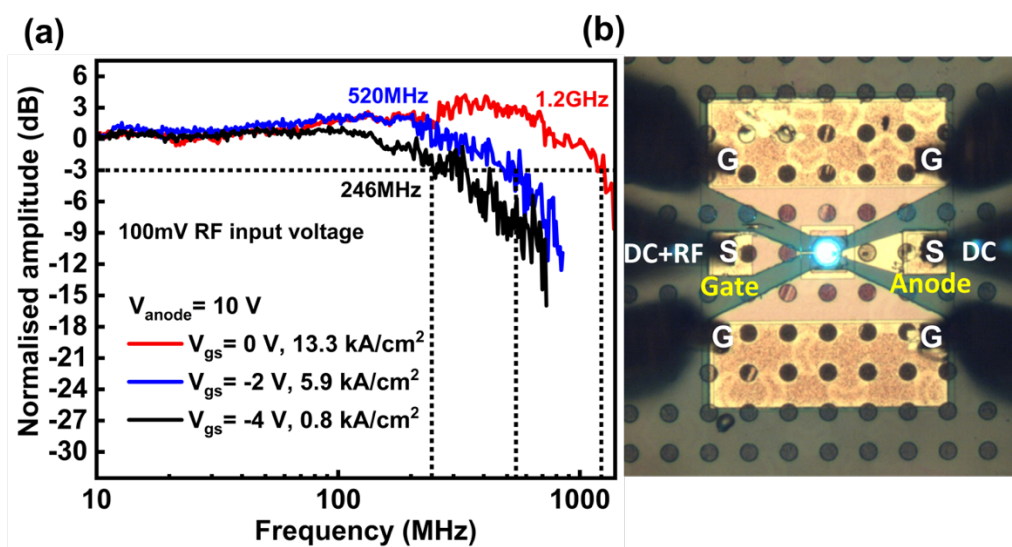
Figure 7-8 Frequency response of our HEMT-microLED measured at different gate voltages with a constant anode voltage of 10V (a). Optical microscope image of HEMT-microLED when turned on (b).

Table 7-1 Benchmarking our monolithically integrated HEMT-microLED against other works.

University	Device Size (µm)	Wavelength (nm)	Current Density (kA/cm^2)	3 dB bandwidth (MHz)
This work	20	480	13.3	1200
Strathclyde[5]	24	450	16	830
Xiamen[19]	30	448	14	160
Strathclyde[4]	44	450	4.6	440
NCU[20]	50	480	4.58	960
Strathclyde[21]	72	450	1.24	245
Tsing Hua[22]	75	500	1.13	463
TSBI[23]	75	460	0.18	1060

7.5.4   Semipolar microLEDs

The logical step forward for the semipolar LEDs in this thesis is to shrink their diameters to the sub 100 µm scale to evaluate VLC performance. As discussed previously, these semipolar microLEDs should have superior performance when compared to their c-plane microLED counterparts. Initial results have been performed on semipolar green microLEDs ranging from 40 to 100 µm in diameter. The detailed fabrication process is shown in Figure 7-9. We firstly defined the mesa using photolithography and an inductively coupled plasma (ICP) etch down to the n-GaN layer. We deposited a transparent current spreading layer (CSL) on top of the mesa to ensure even current spreading and good light extraction. After annealing the CSL we deposited Ti/Al/Au layers for the p and n electrodes. To eliminate short circuiting of the p and n electrodes together we deposited a SiO2 passivation layer using PECVD. We then used ICP to create contact windows on the mesa and n-contact ring. Finally, we deposited metal for the probing pads and connection tracks to the electrodes. We chose a GSG electrode pad configuration to ensure RF isolation at higher frequencies (exceeding 1GHz).
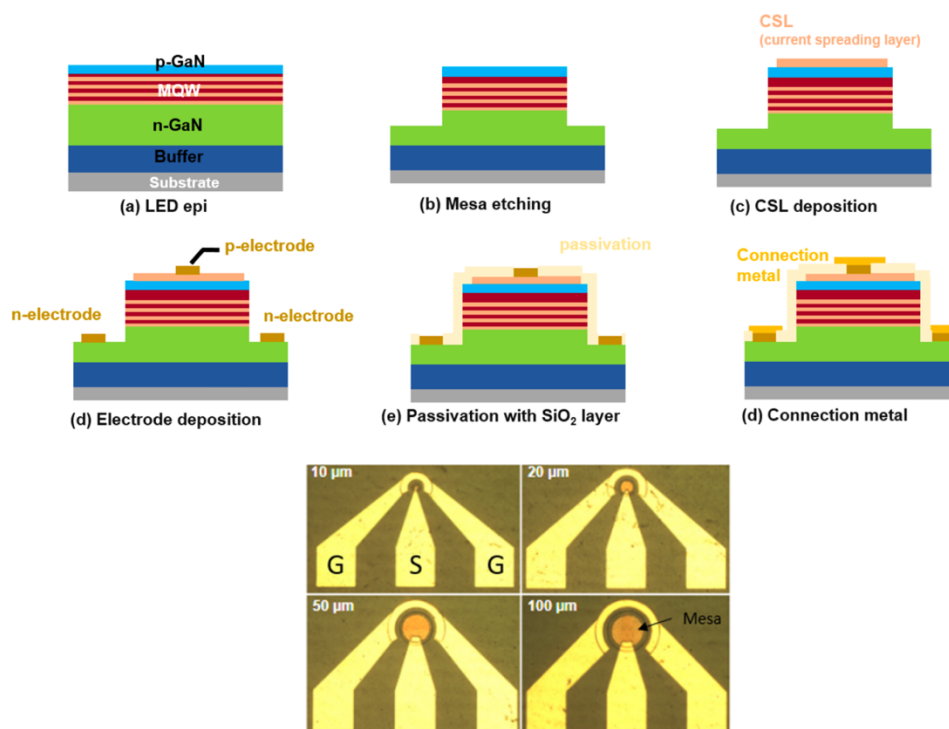
Figure 7-9 Fabrication process of our semipolar microLED.

The initial electrical and frequency response characteristics are shown in Figure 7-10a and b, respectively. Clearly from the IV characteristics, the turn on voltage is very high, indicating a very high series resistance. We think this is possibly due to poor p-GaN activation and will need further investigation. However, for the smaller device, a high modulation bandwidth of 671 MHz was achieved at a current density of 5.97 kA/cm^2 as shown in Figure 7-10b. Optimising the fabrication process is crucial for better performance with these devices.
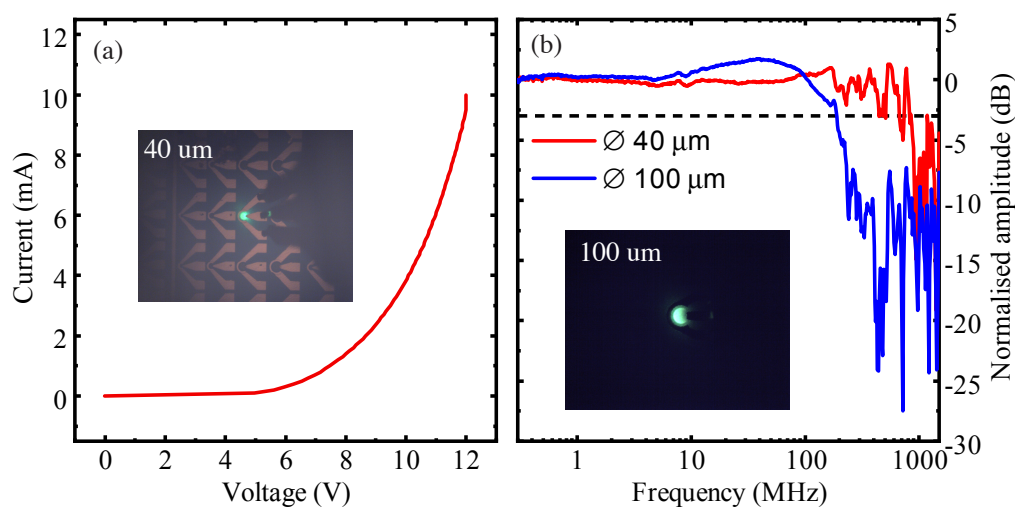
Figure 7-10 Initial results of our semipolar microLEDs showing (a) IV characteristics and (b) frequency response. Inset shows pictures of a 40 μm and 100 μm when biased.

7.6   Summary

In conclusion, we have employed our direct epitaxial approach to achieve small microLEDs on pre-defined micro-hole arrays formed by SiO_2 masks on an AlGaN/GaN HEMT template, demonstrating an epitaxially monolithic on-chip integration of HEMT-µLED, where a single µLED with 20 µm diameter is modulated simply and stably by the gate bias of its HEMT instead of conventional biasing methods for LEDs. Furthermore, our approach has eliminated any dry-etching induced damages which current approaches cannot avoid. All these features have led to the demonstration of a single µLED with a record modulation bandwidth of 1.2 GHz on industry-compatible *c-plane* substrates. Initial results reported on a green semipolar microLED show high bandwidth capabilities and demonstrates the potential of microLED semipolar emitters.

7.7   References

(1)   Ndjiongue, A. R.; Ngatched, T. M. N.; Dobre, O. A.; Armada, A. G. VLC-Based Networking: Feasibility and Challenges. *IEEE Netw.* **2020**, *34* (4), 158–165.

(2)   Jiang, H. X.; Jin, S. X.; Li, J.; Shakya, J.; Lin, J. Y. III-Nitride Blue Microdisplays. *Appl. Phys. Lett.* **2001**, *78* (9), 1303–1305.

(3)   Jeon, C.; Choi, H. W.; Dawson, M. D. A Novel Fabrication Method for a 64× 64 Matrix-addressable GaN-based Micro-LED Array. *Phys. status solidi* **2003**, *200* (1), 79–82.

(4)   McKendry, J. J. D.; Massoubre, D.; Zhang, S.; Rae, B. R.; Green, R. P.; Gu, E.; Henderson, R. K.; Kelly, A. E.; Dawson, M. D. Visible-Light Communications Using a CMOS-Controlled Micro-Light-Emitting-Diode Array. *J. Light. Technol.* **2011**, *30* (1), 61–67.

(5)   Ferreira, R. X. G.; Xie, E.; McKendry, J. J. D.; Rajbhandari, S.; Chun, H.; Faulkner, G.; Watson, S.; Kelly, A. E.; Gu, E.; Penty, R. V. High Bandwidth GaN-Based Micro-LEDs for Multi-Gb/s Visible Light Communications. *IEEE Photonics Technol. Lett.* **2016**, *28* (19), 2023–2026.

(6)   Lin, J. Y.; Jiang, H. X. Development of MicroLED. *Appl. Phys. Lett.* **2020**, *116* (10), 100502.

(7)   Hahn, Y. B.; Choi, R. J.; Hong, J. H.; Park, H. J.; Choi, C. S.; Lee, H. J. High-Density Plasma-Induced Etch Damage of InGaN/GaN Multiple Quantum Well Light-Emitting Diodes. *J. Appl. Phys.* **2002**, *92* (3), 1189–1194.

(8)   Yang, H. S.; Han, S. Y.; Baik, K. H.; Pearton, S. J.; Ren, F. Effect of Inductively Coupled Plasma Damage on Performance of GaN–InGaN Multiquantum-Well Light-Emitting Diodes. *Appl. Phys. Lett.* **2005**, *86* (10), 102104.

(9)   Tian, P.; McKendry, J. J. D.; Gong, Z.; Guilhabert, B.; Watson, I. M.; Gu, E.; Chen, Z.; Zhang, G.; Dawson, M. D. Size-Dependent Efficiency and Efficiency Droop of Blue InGaN Micro-Light Emitting Diodes. *Appl. Phys. Lett.* **2012**, *101* (23), 231110.

(10)   Olivier, F.; Tirano, S.; Dupré, L.; Aventurier, B.; Largeron, C.; Templier, F. Influence of Size-Reduction on the Performances of GaN-Based Micro-LEDs for Display Application. *J. Lumin.* **2017**, *191*, 112–116. https://doi.org/10.1016/j.jlumin.2016.09.052.

(11)   Olivier, F.; Daami, A.; Licitra, C.; Templier, F. Shockley-Read-Hall and Auger Non-Radiative Recombination in GaN Based LEDs: A Size Effect Study. *Appl. Phys. Lett.* **2017**, *111* (2), 22104.

(12)   Huang, Y.; Hsiang, E.-L.; Deng, M.-Y.; Wu, S.-T. Mini-LED, Micro-LED and OLED Displays: Present Status and Future Perspectives. *Light Sci. Appl.* **2020**, *9* (1), 1–16.

(13)   Konoplev, S. S.; Bulashevich, K. A.; Karpov, S. Y. From Large-size to Micro-LEDs: Scaling Trends Revealed by Modeling. *Phys. status solidi* **2018**, *215* (10), 1700508.

(14)   Wong, M. S.; Hwang, D.; Alhassan, A. I.; Lee, C.; Ley, R.; Nakamura, S.; DenBaars, S. P. High Efficiency of III-Nitride Micro-Light-Emitting Diodes by Sidewall Passivation Using Atomic Layer Deposition. *Opt. Express* **2018**, *26* (16),

21324–21331.

(15)   Smith, J. M.; Ley, R.; Wong, M. S.; Baek, Y. H.; Kang, J. H.; Kim, C. H.; Gordon, M. J.; Nakamura, S.; Speck, J. S.; DenBaars, S. P. Comparison of Size-Dependent Characteristics of Blue and Green InGaN MicroLEDs down to 1 μ m in Diameter. *Appl. Phys. Lett.* **2020**, *116* (7), 71102.

(16)   Islim, M. S.; Ferreira, R. X.; He, X.; Xie, E.; Videv, S.; Viola, S.; Watson, S.; Bamiedakis, N.; Penty, R. V; White, I. H.; Kelly, A. E.; Gu, E.; Haas, H.; Dawson, M. D. Towards 10 Gb/s Orthogonal Frequency Division Multiplexing-Based Visible Light Communication Using a GaN Violet Micro-LED. *Photonics Res.* **2017**, *5* (2), A35–A43.

(17)   Liu, Z.; Ma, J.; Huang, T.; Liu, C.; Kei May, L. Selective Epitaxial Growth of Monolithically Integrated GaN-Based Light Emitting Diodes with AlGaN/GaN Driving Transistors. *Appl. Phys. Lett.* **2014**, *104* (9), 1–6.

(18)   Bai, J.; Cai, Y.; Feng, P.; Fletcher, P.; Zhao, X.; Zhu, C.; Wang, T. A Direct Epitaxial Approach to Achieving Ultrasmall and Ultrabright InGaN Micro Light-Emitting Diodes (MLEDs). *ACS photonics* **2020**, *7* (2), 411–415.

(19)   Bai, J.; Cai, Y.; Feng, P.; Fletcher, P.; Zhu, C.; Tian, Y.; Wang, T. Ultrasmall, Ultracompact and Ultrahigh Efficient InGaN Micro Light Emitting Diodes (MLEDs) with Narrow Spectral Line Width. *ACS Nano* **2020**, *14* (6), 6906–6911.

(20)   Zheng, Z. W.; Yu, H.; Ren, B. C.; Zhou, L. M.; Fu, H. Y.; Cheng, X.; Ying, L. Y.; Long, H.; Zhang, B. P. Modulation Characteristics of GaN-Based Light-Emitting-Diodes for Visible Light Communication. *ECS J. Solid State Sci. Technol.* **2017**, *6* (9), R135.

(21)   Shi, J.-W.; Chi, K.-L.; Wun, J.-M.; Bowers, J. E.; Shih, Y.-H.; Sheu, J.-K. III-Nitride-Based Cyan Light-Emitting Diodes with GHz Bandwidth for High-Speed Visible Light Communication. *IEEE Electron Device Lett.* **2016**, *37* (7), 894–897.

(22)   McKendry, J. J. D.; Green, R. P.; Kelly, A. E.; Gong, Z.; Guilhabert, B.; Massoubre, D.; Gu, E.; Dawson, M. D. High-Speed Visible Light Communications Using Individual Pixels in a Micro Light-Emitting Diode Array. *IEEE Photonics Technol. Lett.* **2010**, *22* (18), 1346–1348.

(23)   Liao, C.-L.; Ho, C.-L.; Chang, Y.-F.; Wu, C.-H.; Wu, M.-C. High-Speed Light-Emitting Diodes Emitting at 500 Nm with 463-MHz Modulation Bandwidth. *IEEE electron device Lett.* **2014**, *35* (5), 563–565.

(24)   Wei, Z.; Zhang, L.; Wang, L.; Chen, C.-J.; Wang, Z.; Chen, K.-C.; Wu, M.-C.; Dong, Y.; Wang, L.; Luo, Y. Multi-User High-Speed QAM-OFDMA Visible Light Communication System Using a 75-Mm Single Layer Quantum Dot Micro-LED. *Opt. Express* **2020**, *28* (12), 18332–18342.

Chapter 8: Conclusion

8.1   Conclusion

The work presented in this thesis involved utilising and studying semipolar InGaN/GaN light emitting diodes (LEDs) unique advantages over conventional *c-plane* structures such as increased indium incorporation, reduced QCSE and shorter recombination lifetime to demonstrate viable, long wavelength visible light communications (VLC). In addition, monolithic on-chip integration of a *c-plane* microLED and HEMT was achieved using our novel direct epitaxy approach, which allows for stable, high current density operation due to the elimination of etching induced sidewall damage, which lead to the highest modulation bandwidth achieved with *c-plane* GaN LEDs at the time of publishing.

8.1.1   Overview

High Modulation Bandwidth of Semipolar (11$\bar{2}$2) InGaN/GaN LEDs with Long Wavelength Emission

Frequency response measurements presented the highest yet reported modulation bandwidths for respective wavelengths on our semipolar (11$\bar{2}$2) LEDs. Modulation bandwidths of 540 MHz, 350 MHz, and 140 MHz for our green, yellow, and amber LEDs were demonstrated, only possible due to our novel overgrowth technique allowing for crystal quality similar to conventional *c-plane* structures. This study confirms that the modulation bandwidth is significantly enhanced due to the intrinsically low polarisation present on the (11$\bar{2}$2) semipolar plane and unlocks possibilities for VLC applications.

Long-Wavelength Semipolar (11$\bar{2}$2) nGaN/GaN LEDs with Multi- Gb/s Data Transmission Rates for VLC

Following on from the previous chapter, record data transmission rates of 4.22 Gb/s, 3.72 Gb/s and 336 Mb/s for our green, yellow, and amber LEDs have been demonstrated, respectively. The exceptionally high data rates were achieved using adaptive bit loading DC-biased optical orthogonal frequency division multiplexing (DCO-OFDM), a modulation scheme which exploits the limited bandwidth of our semipolar LEDs and maximises the data throughput. Data transmission rates as high as this cannot be achieved using commercial *c-plane* GaN emitters at these wavelengths due to poor optical performance with increased indium compositions. The enhanced indium incorporation in (11$\bar{2}$2) GaN means longer wavelength emitters can be achieved without sacrificing crystal quality and optical performance when lowering metal organic chemical vapour deposition (MOCVD) growth temperatures. As a result, in VLC applications, higher signal-to-noise ratio (SNR) values can be achieved which consequently lead to record breaking data transmission rates.

A study of the luminescence decay of a semipolar green LED for visible light communications by time-resolved electroluminescence

Time resolved photoluminescence (TRPL) is a technique to study carrier dynamics in an LED structure but is fundamentally limited for VLC applications due to the absence of consideration for carrier transport effects. We demonstrated the significance of electrically injected temporal luminescence where transport effects are clearly shown in LED decay profiles when an appropriate model is used. A semipolar green LED was found to follow closely to a tri-exponential decay, with two lifetimes associated with radiative and non-radiative lifetimes comparable to TRPL and a third lifetime attributed to transport effects as confirmed by inductance, capacitance, and resistance (LCR) measurements. A similar wavelength green *c-plane* LED was found to demonstrate a monoexponential decay with a single lifetime, indicating resistance-capacitance (RC) effects are a limiting factor.

Direct Epitaxial Approach to Achieve a Monolithic On-Chip Integration of a HEMT and a Single Micro-LED with a High- Modulation Bandwidth

Dry etching sidewall damages have been eliminated using our novel direct epitaxially approach when fabricating a 20 μm LED monolithically grown on a AlGaN/GaN high electron mobility transistor (HEMT) template. The LED can be modulated using the gate of the HEMT, allowing for sable, high current density operation. As a result, our integrated HEMT-microLED achieved a record modulation bandwidth of 1.2 GHz at 13.3 kA/cm^2.

8.1.2 Future work

Replacing solid state lighting with monolithic RGB semipolar LEDs

The most promising result from this thesis is that semipolar LEDs can cover most of the required visible light spectrum for adobe sRGB, offer very high bandwidth whilst also being relatively efficient. An interesting avenue to explore would be to try and integrate multi-coloured semipolar LEDs on a common, silicon substrate in the hopes to achieve a monolithic RGB chip capable of replacing solid state lighting (SSL) for general illumination and serving as a data transmitter/receiver. The next step forward would be to try to grow the same templates on Si substrates rather than sapphire. After the recipe is optimised on Si, a fusion bonding process between three wafers each containing red, green, and blue epi structures could be implemented in order to achieve monolithic integration of the three colours. Similar packaging techniques used in SSL infrastructure today could then be adopted relatively easily since the RGB pixel pitch density should be much lower than standard, hybrid RGB LED packages. Modulation techniques which then take advantage of the different colours i.e., colour shift keying (CSK) as well as spectrally efficient techniques such as the schemes used in this thesis can be implemented at low cost. In parallel, similar processes can be used to

create microLED RGB displays suitable for small form factor displays such as watches, phones and heads-up-displays (HUD).

HEMT-LED display for VLC

Recently, using our novel direct epitaxy method, our group has developed a 8 × 8 HEMT-microLED display fabricated monolithically on a single chip[1]. As each HEMT-microLED can be individually addressed, then in theory each LED could be modulated using the technique demonstrated in Chapter 5. Assuming each LED offers similar bandwidth to that of the device in Chapter 7, then an array of these devices will not only increase the SNR due to the increased output power but will also have a significantly increased modulation bandwidth as a result of the 64 devices. Efforts will therefore be focused on the designing a high-bandwidth CMOS driver for the display, as this is the only roadblock in realising VLC with this device.

8.2   References

(1)   Cai, Y.; Zhu, C.; Zhong, W.; Feng, P.; Jiang, S.; Wang, T. Monolithically Integrated MLEDs/HEMTs Microdisplay on a Single Chip by a Direct Epitaxial Approach. *Adv. Mater. Technol.* **2021**, *6* (6), 2100214.

Appendix

This section gives the raw code for both DCO-OFDM and OOK modulation using MATLAB. DCO-OFDM is achieved using four main scripts: Program 1 generates fixed QAM modulation for channel estimation or simple fixed rate data transmission testing. Program 2 uses the data from Program 1 as well as the measured OFDM waveform measured from the LED on the oscilloscope and aligns them sample by sample using cross-correlation. Program 1 is then run again in full with the aligned waveform to calculate SNR and BER characteristics. Program 3 takes these measurements and adaptively loads bits to each subcarrier specified by its SNR and target BER value. Program 4 creates the adaptively bit loaded waveform for LED data transmission testing, and then Program 2 is used again to align the transmitted and received waveforms. Finally, Program 4 is run again in full with the aligned waveform to generate the adaptively bit loaded BER characteristics. The waveform is equalised using the channel response calculated in Program 1.

8.3   MATLAB code for DCO-OFDM modulation

8.3.1   Program 1: Fixed rate QAM and/or channel estimation

```
1   %%------------------------------------------------------------
2   ------------------------------%
3
4   % ---PROGRAM 1 - RUN THIS SCRIPT FIRST FOR CHANNEL ESTIMATION (or
5   simple fixed rate modulation)---%
6
7   %------------------------------------------------------------
8   ------------------------------%
9
10  % A MATLAB program that simulates DC biased optical OFDM (DCO-OFDM)
11  for LEDs and creates waveforms
12  % of suitable file format to experimentally demonstrate using a
13  Tektronix AWG70k series AWG
14  % Jack Haggar 2020 ¨©
15  %------------------------------------------------------------
16  ------------------------------%
17  close all
18  %% First define simulation parameters
19  M = 4;                      % Modulation order (alphabet size or
20  number of points in signal constellation)
21  k = log2(M);                % Number of bits per symbol
22  n = k*(64^2) ;              % Number of bits to process
23  subs = 64;                  % Number of subcarriers
24  cp = 16;                    % cyclic prefix length
25  sps = 4;                    % Number of samples per symbol
26  (oversampling factor)
27  rolloff = 0.1;              % RRC filter rolloff
28  filtlen = subs;             % Filter span in symbols
29  n_pilot_frames = 2;         % number of OFDM pilot frames for
30  channel estimation
31  LED_SSB = 10;               % LED single sided bandwidth (in MHz,
32  rough estimate for channel BW)
33  amplifier_gain = 29;        % typical amplifier gain (dB)
```

```matlab
34    voltage_pp = 14;             % desired peak-peak voltage swing after
35    pre-amplification (V)
36    DC_bias = 5;                 % desired DC-bias used after pre-
37    amplification (V)
38    %% System throughput
39    %Data rate for the system is D = 2*B*spectral_Efficiency where B is
40    the
41    %single sided bandwidth of the system i.e. the LED + channel
42    %The spectral efficiency is:
43    spectral_efficiency = (k*(subs-2))/((2*(subs+cp)*(1+rolloff)));
44    %and the data rate of transmission is:
45    data_rate_Mbps = 2*LED_SSB*spectral_efficiency
46    %% Generate data
47    rng 'default';
48    %rng (1,'philox');
49    dataIn = randi([0 1],n,1); % Generate vector of binary data
50    dataInMatrix = reshape(dataIn,length(dataIn)/k,k);
51    dataSymbolsIn = bi2de(dataInMatrix);
52    %% Take N/2-1 subcarriers, modulate using QAM, then perform
53    hermitian symmetry
54    %serial to parallel conversion
55    subs_2= subs/2;
56    dataSymbolsIn_new=reshape(dataSymbolsIn,[length(dataSymbolsIn)/subs
57    _2,subs_2]);
58    dataSymbolsIn_new(:,subs_2)=[];
59    dataMod =
60    qammod(dataSymbolsIn_new,M,'bin','UnitAveragePower',true);
61    conj_dataMod=conj(dataMod);
62    %Ensure hermitian symmetry in IFFT by setting x_0 and x_n/2 to 0
63    a=zeros(length(dataSymbolsIn)/subs_2,1);
64    b=zeros(length(dataSymbolsIn)/subs_2,1);
65    X = [a dataMod b fliplr(conj_dataMod)];
66    figure;
67    for i=subs/8:subs/8:subs % plot Tx symbols per subcarrier
68    subplot(2,4,i/(subs/8))
69    plot(X(:,i),'.');
70    title(['SC#: ',num2str(i), '    f: ', num2str((LED_SSB/subs_2)*i),
71    ' MHz']);
72    xlabel('In-phase');
73    ylabel('Quadrature');
74    end
75    %% Perform IFFT, covert to serial signal then add cyclic prefix
76    ifft_X=ifft(X,[],2);
77    ifft_X_2=reshape(ifft_X,[],1);
78    cp_vector=ifft_X_2(end-cp+1:end);
79    cp_ifft_X=[cp_vector;ifft_X_2];
80
81    %% Perform oversampling using a SRRC filter to satisfy Nyquist
82    limit
83    rrcFilter = rcosdesign(rolloff,filtlen,sps);
84    txFiltSignal = upfirdn(cp_ifft_X,rrcFilter,sps,1);
85
86    %% Clipping the time domain signal in the range [-3?…,3?…] in order
87    to not exceed LED dynamic range
88    %Calculate scaling factor (0-500mV) on the AWG for a desired
89    voltage swing
90    %after a 29dB amplification from SHF S126 A (This does add clipping
91    noise
92    %but should reduce BER)
93    voltage_initial = voltage_pp*10^(-amplifier_gain/20);
```

```matlab
94   txFiltSignal = normalize(txFiltSignal,'range',[-
95   voltage_initial,voltage_initial]);
96   standard_deviation = std(txFiltSignal); % time domain standard
97   deviation (for clipping);
98   txFiltSignal(txFiltSignal>3*standard_deviation)=3*standard_deviatio
99   n; % clipping of the signal positive
100  txFiltSignal(txFiltSignal<-3*standard_deviation)=-
101  3*standard_deviation; % clipping of the signal negative
102  pilot_signal = repmat(txFiltSignal,n_pilot_frames,1); % Creating
103  pilot signal for channel estimation
104  amplified_signal =  txFiltSignal.*(10^(amplifier_gain/20))+DC_bias;
105  % for analysis purposes
106  awg_samplerate_MSps = LED_SSB*sps*2
107  %% Convert to AWG70002A compatible file - change sample rate on AWG
108  % Retrieve IQ Data
109  iData = real(txFiltSignal);
110  qData = imag(txFiltSignal);
111  % Create I Waveform
112  Waveform_Name_1 = 'MyI_Waveform';
113  Waveform_Data_1 = iData;
114  Waveform_Sampling_Rate_1 = LED_SSB*sps*2*1e6;
115  %LEDbandwdith*sps*2(Nyquist)
116  Waveform_Signal_Format_1 = 'I';
117  % Create Q Waveform
118  Waveform_Name_2 = 'MyQ_Waveform';
119  Waveform_Data_2 = qData;
120  Waveform_Sampling_Rate_2 = LED_SSB*sps*2*1e6;
121  Waveform_Signal_Format_2 = 'Q';
122  % Save Files
123  save('OFDM_signal_yellow_64qam.mat', '*_1', '*_2', '-v7.3');
124  % Convert pilot waveform
125  iData_p = real(pilot_signal);
126  qData_p = imag(pilot_signal);
127  % Create I Waveform
128  Waveform_Name_3 = 'MyI_Pilot';
129  Waveform_Data_3 = iData_p;
130  Waveform_Sampling_Rate_3 = LED_SSB*sps*2*1e6;
131  Waveform_Signal_Format_3 = 'I';
132  % Create Q Waveform
133  Waveform_Name_4 = 'MyQ_Pilot';
134  Waveform_Data_4 = qData_p;
135  Waveform_Sampling_Rate_4 = LED_SSB*sps*2*1e6;
136  Waveform_Signal_Format_4 = 'Q';
137  % Save Files
138  save('OFDM_pilot_yellow_64qam.mat', '*_3', '*_4', '-v7.3');
139  %% Creating the channel (for simulation purposes only)
140  EbNo = 13;%*g;
141  snr = EbNo + 10*log10(k) - 10*log10(sps);
142  rxSignal = awgn(txFiltSignal,snr,'measured');
143  rxSignal_pilot = awgn(pilot_signal,snr,'measured');
144  %% Taking data from Sampling_conversion .m file (i.e. oscilloscope)
145  comment out as desired
146  % rxSignal_pilot = T3;
147  % rxSignal = T1;
148  %% Receiving the signal, downsampling and filtering
149  rxFiltSignal = upfirdn(rxSignal,rrcFilter,1,sps);   % Downsample and
150  filter
151  rxFiltSignal = rxFiltSignal(filtlen + 1:end - filtlen); % Account
152  for delay
```

```matlab
153    rxFiltSignal_pilot =
154    reshape(rxSignal_pilot,[length(pilot_signal)/n_pilot_frames,
155    n_pilot_frames]);
156    rxFiltSignal_pilot = upfirdn(rxFiltSignal_pilot,rrcFilter,1,sps); %
157    Downsample and filter
158    rxFiltSignal_pilot = rxFiltSignal_pilot(filtlen + 1:end - filtlen,
159    :); % Account for delay
160    %% removing cyclic prefix, convert to parallel then applying fft
161    %Signal
162    rxFiltsignal_nocp=rxFiltSignal(cp+1:end);
163    rxFiltsignal_nocp1=reshape(rxFiltsignal_nocp,[length(rxFiltsignal_n
164    ocp)/subs,subs]);%S->P
165    fft_X=fft(rxFiltsignal_nocp1,[],2);
166    fft_X=normalize(fft_X);
167    figure;
168    for i=subs/64:subs/64:subs_2 % plot Rx symbols per subcarrier
169    subplot(4,8,i/(subs/64))
170    plot(fft_X(:,i),'.');
171    title(['SC#: ',num2str(i), '     f: ', num2str((LED_SSB/subs_2)*i),
172    ' MHz']);
173    xlabel('In-phase');
174    ylabel('Quadrature');
175    xlim([-1.2 1.2])
176    ylim([-1.2 1.2])
177    hold on
178    plot(X(:,i),'r x','MarkerSize', 5,'linewidth', 3);
179    end
180    fft_X(:,(subs/2+1))=[];
181    fft_X(:,1)=[];
182
183    %Pilot
184    rxFiltSignal_pilot_nocp = rxFiltSignal_pilot(cp+1:end,:);
185    rxFiltSignal_pilot_nocp1 =
186    reshape(rxFiltSignal_pilot_nocp,[length(rxFiltSignal_pilot_nocp)/su
187    bs,subs,n_pilot_frames]);
188    fft_X_pilot=fft(rxFiltSignal_pilot_nocp1,[],2);
189    fft_X_pilot(:,(subs/2+1),:) = [];
190    fft_X_pilot(:,1,:) = [];
191    fft_X_pilot=normalize(fft_X_pilot);
192    %% Channel estimation and equalisation
193    % Retrieve Pilot frame and split into single OFDM frames
194    % Channel can then be estimated using a conventional mean estimator
195    used in
196    % Tsonev 2015 IEEE. Noise energy i.e. noise variance can also be
197    estimated
198    % from this technique and as a result the SNR per frequency
199    subcarrier of
200    % the channel can be calculated.
201    X(:,(subs/2+1))=[];
202    X(:,1)=[];
203    sum_pilot = sum(fft_X_pilot,3);
204    H_channel = sum_pilot./((n_pilot_frames).*X);
205    channel_gain = (abs(H_channel).^2);
206    equalised_signal = fft_X./H_channel;
207
208    for i=subs/64:subs/64:subs_2 % plot Rx symbols per subcarrier
209    subplot(4,8,i/(subs/64))
210    plot(equalised_signal(:,i),'.');
211    title(['SC#: ',num2str(i), '     f: ', num2str((LED_SSB/subs_2)*i),
212    ' MHz']);
213    xlabel('In-phase');
```

```matlab
214    ylabel('Quadrature');
215    xlim([-1.2 1.2])
216    ylim([-1.2 1.2])
217    hold on
218    plot(X(:,i),'r x','MarkerSize', 5,'linewidth', 3);
219    end
220    %% SNR calculation
221    evm = comm.EVM;
222    CF = 2.6; %crest factor (calculate from constellation M-QAM)
223    rmsEVM1 = evm(X,fft_X);
224    SNR = -(CF+20*log(rmsEVM1/100));
225    SNR_data_for_P3=SNR(:,1:subs_2-1);
226    %% Demodulate the equalised QAM constellation and calculate the BER
227    dataSymbolsOut2 = qamdemod(fft_X,M,'bin','UnitAveragePower',true);
228    dataSymbolsOut2 = dataSymbolsOut2(:,1:(subs/2)-1);
229    dataSymbolsOut2 = dataSymbolsOut2(:);
230    dataSymbolsIn_new = dataSymbolsIn_new(:);
231    dataSymbolsOut3 =
232    qamdemod(equalised_signal,M,'bin','UnitAveragePower',true);
233    dataSymbolsOut3 = dataSymbolsOut3(:,1:(subs/2)-1);
234    dataSymbolsOut3 = dataSymbolsOut3(:);
235    dataSymbolsIn_new = dataSymbolsIn_new(:);
236    % compare bits out to bits in to calculate bit error ratio (BER)
237    [no_errors_before_eq,BER_before_eq] =
238    biterr(dataSymbolsOut2,dataSymbolsIn_new);
239    [no_errors_after_eq,BER_after_eq] =
240    biterr(dataSymbolsOut3,dataSymbolsIn_new);
241
242    fft_X_dataSC=fft_X(:,1:subs_2-1);
243    fft_X_dataSC_EQ=equalised_signal(:,1:subs_2-1);
244    fft_X_pilot_dataSC=fft_X_pilot(:,1:subs_2-1);
245
246    fft_X_dataSC =fft_X_dataSC(:);
247    fft_X_dataSC_EQ = fft_X_dataSC_EQ(:);
248    fft_X_pilot_dataSC = fft_X_pilot_dataSC(:);
249    %% Plotting final graphs
250    scatterplot(fft_X_dataSC);
251    xlabel('In-phase');
252    ylabel('Quadrature');
253    title([num2str(round(data_rate_Mbps)), ' Mbps with BER = '
254    ,num2str(BER_before_eq)]);
255    hold on
256    plot(dataMod(:,2),'r x','MarkerSize', 5,'linewidth', 3);
257    scatterplot(fft_X_dataSC_EQ);
258    xlabel('In-phase');
259    ylabel('Quadrature');
260    title([num2str(round(data_rate_Mbps)), ' Mbps with BER = '
261    ,num2str(BER_after_eq)]);
262    hold on
263    plot(dataMod(:,2),'r x','MarkerSize', 5,'linewidth', 3);
264    figure;
265    plot(SNR_data_for_P3);
266    title('SNR per subcarrier');
267    xlabel('Subcarrier Index');
268    ylabel('SNR (dB)');
269
```

8.3.2 Program 2: Aligning Tx and Rx signals from AWG/oscilloscope

```matlab
%%---------------------------------------------------------------
-----------------------------%

% --------------PROGRAM 2 - RUN THIS SCRIPT AFTER AQUIRING DATA
FROM OSCILLOSCOPE-----------------%

%---------------------------------------------------------------
-----------------------------%
% A MATLAB program that simulates DC biased optical OFDM (DCO-OFDM)
for LEDs and creates waveforms
% of suitable file format to experimentally demonstrate using a
Tektronix AWG70k series AWG
% Jack Haggar 2020 ¬¨¬©
%---------------------------------------------------------------
-----------------------------%
close all
%% First define syncronisation parameters
AWG_Fs = 8e9;                      % AWG sampling rate
OSC_Fs = 25e9;                     % oscilloscope sampling rate
signal = -signal;
pilot = -pilot;
abl = -abl;
abl_pilot = -abl_pilot;

[P1,Q1] = rat(AWG_Fs/OSC_Fs);     % Rational fraction approximation
T1 = resample(signal,P1,Q1);      % Change sampling rate by rational
factor
T2 = txFiltSignal;                % Input signal from PROGRAM 1
T3 = resample(pilot,P1,Q1);       % Change sampling rate by rational
factor
T4 = pilot_signal;                % Input signal from PROGRAM 1
%% Cross correlation function to compare input signal to scope
signal SIGNAL
[C1,lag1] = xcorr(T2,T1);
figure                            % Plotting xcorr funtion
plot(lag1/AWG_Fs,C1)
ylabel('Amplitude')
grid on
title('Cross-correlation between Input and Output SIGNAL')
%% Cross correlation function to compare input signal to scope
signal PILOT
[C2,lag2] = xcorr(T4,T3);
figure                            % Plotting xcorr funtion
plot(lag2/AWG_Fs,C2)
ylabel('Amplitude')
grid on
title('Cross-correlation between Input and Output PILOT')
%% Calculating time/sample difference between signals and
syncronisation SIGNAL
[~,I1] = max(abs(C1));
SampleDiff1 = lag1(I1)
timeDiff1 = SampleDiff1/AWG_Fs
T1 = T1(abs(SampleDiff1-1):end);
diff1 = length(T1)-length(T2);
T1 = T1(1:end-diff1);
Aligned_delay1 = finddelay(T1,T2)
%% Calculating time/sample difference between signals and
syncronisation PILOT
[~,I2] = max(abs(C2));
```

```matlab
60    SampleDiff2 = lag2(I2)
61    timeDiff2 = SampleDiff2/AWG_Fs
62    T3 = T3(abs(SampleDiff2-1):end);
63    diff2 = length(T3)-length(T4);
64    T3 = T3(1:end-diff2);
65    Aligned_delay2 = finddelay(T3,T4)
66    %% Aligned signal plotting for confirmation of correct
67    syncronisation SIGNAL
68    figure;
69    subplot(2,1,1)
70    plot(T1);
71    title('Received signal SIGNAL');
72    xlabel('Samples');
73    ylabel('Voltage (V)');
74    xlim([2100 2150])
75    grid on
76    subplot(2,1,2)
77    plot(T2);
78    title('Transmitted signal SIGNAL');
79    xlabel('Samples');
80    ylabel('Voltage (V)');
81    xlim([2100 2150])
82    grid on
83    figure;
84    subplot(2,1,1)
85    plot(T1);
86    title('Received signal SIGNAL');
87    xlabel('Samples');
88    ylabel('Voltage (V)');
89    grid on
90    subplot(2,1,2)
91    plot(T2);
92    title('Transmitted signal SIGNAL');
93    xlabel('Samples');
94    ylabel('Voltage (V)');
95    grid on
96    %% Aligned signal plotting for confirmation of correct
97    syncronisation PILOT
98    figure;
99    subplot(2,1,1)
100   plot(T3);
101   title('Received signal PILOT');
102   xlabel('Samples');
103   ylabel('Voltage (V)');
104   xlim([2100 2150])
105   grid on
106   subplot(2,1,2)
107   plot(T4);
108   title('Transmitted signal PILOT');
109   xlabel('Samples');
110   ylabel('Voltage (V)');
111   xlim([2100 2150])
112   grid on
113   figure;
114   subplot(2,1,1)
115   plot(T3);
116   title('Received signal PILOT');
117   xlabel('Samples');
118   ylabel('Voltage (V)');
119   grid on
120   subplot(2,1,2)
```

```
121   plot(T4);
122   title('Transmitted signal PILOT');
123   xlabel('Samples');
124   ylabel('Voltage (V)')
```

8.3.3 Program 3: Adaptive bit loading algorithm

```matlab
%%-------------------------------------------------------------
------------------------------%

% --------------PROGRAM 3 - RUN THIS SCRIPT AFTER CALCULATING SNR
PER SUBCARRIER------------------%

%-------------------------------------------------------------
------------------------------%
% A MATLAB program that simulates DC biased optical OFDM (DCO-OFDM)
for LEDs and creates waveforms
% of suitable file format to experimentally demonstrate using a
Tektronix AWG70k series AWG
% Jack Haggar 2020 ¬¨¬©
%-------------------------------------------------------------
------------------------------%
close all
%% Import SNR per subcarrier data measured from channel estimation
SNR_k= SNR_data_for_P3;
Eb_No = 10.^(SNR_k/10);              % energy per bit/ noise
M_k = zeros(1,length(SNR_k));     % initialise adaptive bit vector
channel_bandwidth = 1000    % used bandwidth (MHz)
%% Bit maximisation algorithm below a target BER using SNR profile
(equation from Yoon et al. 2000)
for n=1:length(SNR_k)
    for m=1:30
        k=2^m;
        qfunction(m,n) = qfunc(sqrt(3*log2(k)*(Eb_No(n)/m)/(2*(k-
1))));
        BER(m,n) = ((sqrt(k)-
1)/(sqrt(k)*log2(sqrt(k))))*qfunction(m,n);
        if BER(m,n)>=3.8e-3
            M_k(n)=m;
            if M_k(n)<2
                M_k(n)=0;
            end
            break
        elseif BER(m,n)<3.8e-3
            continue
        end
    end
end
%% Adaptive Data throughput (R) and plotting
R = channel_bandwidth*sum(M_k)/((length(SNR_k)+16))
yyaxis left
plot(SNR_k)
ylim([0 25])
xlabel('Subcarrier number');
ylabel('SNR (dB)');
hold on
yyaxis right
stem(M_k)
```

8.3.4 Program 4: Data transfer using adaptive bit loading

```
1   %%------------------------------------------------------------
2   ----------------------------%
3
4   % --------PROGRAM 4 - DATA TRANSFER USING ADAPTIVE BIT LOADING
5   CALCULATED FROM PROGRAM 3----------%
6
7   %------------------------------------------------------------
8   ----------------------------%
9   % A MATLAB program that simulates DC biased optical OFDM (DCO-OFDM)
10  for LEDs and creates waveforms
11  % of suitable file format to experimentally demonstrate using a
12  Tektronix AWG70k series AWG
13  % Jack Haggar 2020 ¬¨¬©
14  %------------------------------------------------------------
15  ----------------------------%
16  close all
17  %% First define simulation parameters
18  M = 2.^M_k;                    % Modulation order (alphabet size or
19  number of points in signal constellation)
20  k = log2(M);                   % Number of bits per symbol
21  n = 1000*k;                    % Total number of bits to process
22  subs = 512;                    % Number of subcarriers
23  cp = 16;                       % cyclic prefix length
24  sps = 4;                       % Number of samples per symbol
25  (oversampling factor)
26  rolloff = 0.1;                 % RRC filter rolloff
27  n_pilot_frames = 1;
28  filtlen = subs;                % Filter span in symbols
29  amplifier_gain = 29;           % typical amplifier gain (dB)
30  voltage_pp = 6.5;              % desired peak-peak voltage swing after
31  pre-amplification (V)
32  DC_bias = 5;                   % desired DC-bias used after pre-
33  amplification (V)
34  LED_SSB = 1000;
35  rng 'default';
36  awg_samplerate_MSps = channel_bandwidth*sps*2;
37  %% System throughput
38  %Data rate for the system is D = 2*B*spectral_Efficiency where B is
39  the
40  %single sided bandwidth of the system i.e. the LED + channel
41  %The spectral efficiency is:
42  spectral_efficiency = sum(M_k)/((2*(subs+cp)*(1+rolloff)));
43  %and the data rate of transmission is:
44  data_rate_Mbps = channel_bandwidth*sum(M_k)/((length(SNR_k)+cp))
45  %% Generate data for each subcarrier with different modulation
46  formats
47  subs_2 = subs/2;
48  dataIn = zeros(max(n),length(M));
49  dataMod = zeros(max(n)/max(k),length(M));
50  A = zeros(length(dataMod),1);
51  B = zeros(length(dataMod),1);
52  for i=1:length(M)
53
54      if n(i) == 0
55          break
56      end
57  dataIn(1:max(n(i)),i) = randi([0 1],n(i),1); % Generate vectors of
58  binary data
59  P = dataIn(1:max(n(i)),i);
```

```matlab
60    dataMod(1:max(n(i))/k(i),i) =
61    qammod(P,M(i),'InputType','bit','UnitAveragePower',true);
62    conj_dataMod = conj(dataMod);
63    end
64    X = transpose([A dataMod B fliplr(conj_dataMod)]);
65     Y = X(:);
66    scatterplot(Y);
67    figure('Name','Transmitted QAM subcarriers','NumberTitle','off')
68    for i=subs/64:subs/64:subs_2 % plot Tx symbols per subcarrier
69    subplot(4,8,i/(subs/64))
70    plot(X(i,:),'.');
71    title(['SC#: ',num2str(i), '    f: ', num2str((channel_bandwidth
72    /subs_2)*i), ' MHz']);
73    xlabel('In-phase');
74    ylabel('Quadrature');
75    xlim([-1.2 1.2])
76    ylim([-1.2 1.2])
77    hold on
78    plot(X(i,:),'r x','MarkerSize', 5,'linewidth', 3);
79    end
80    %% Perform IFFT, covert to serial signal then add cyclic prefix
81    ifft_X=ifft(X);
82    ifft_X_2=reshape(ifft_X,[],1);
83    cp_vector=ifft_X_2(end-cp+1:end);
84    cp_ifft_X=[cp_vector;ifft_X_2];
85
86    %% Perform oversampling using a SRRC filter to satisfy Nyquist
87    limit
88    rrcFilter = rcosdesign(rolloff,filtlen,sps);
89    txFiltSignal_abl = upfirdn(cp_ifft_X,rrcFilter,sps,1);
90
91    %% Clipping the time domain signal in the range [-3≈ì√â,3≈ì√â] in
92    order to not exceed LED dynamic range
93    % Calculate scaling factor (0-500mV) on the AWG for a desired
94    voltage swing
95    % after a 29dB amplification from SHF S126 A (This does add
96    clipping noise
97    % but should reduce BER)
98      voltage_initial = voltage_pp*10^(-amplifier_gain/20)
99      txFiltSignal = normalize(txFiltSignal,'range',[-
100   voltage_initial,voltage_initial]);
101     standard_deviation = std(txFiltSignal_abl) % time domain standard
102   deviation (for clipping)
103
104   txFiltSignal_abl(txFiltSignal_abl>3*standard_deviation)=3*standard_
105   deviation; % clipping of the signal positive
106     txFiltSignal_abl(txFiltSignal_abl<-3*standard_deviation)=-
107   3*standard_deviation; % clipping of the signal negative
108     pilot_signal_abl = repmat(txFiltSignal_abl,n_pilot_frames,1); %
109   Creating pilot signal for channel estimation
110     amplified_signal =
111   txFiltSignal.*(10^(amplifier_gain/20))+DC_bias; % for analysis
112   purposes
113   %% Convert to AWG70002A compatible file - change sample rate on AWG
114   % Retrieve IQ Data
115   iData = real(txFiltSignal_abl);
116   qData = imag(txFiltSignal_abl);
117   % Create I Waveform
118   Waveform_Name_1 = 'MyI_Waveform';
119   Waveform_Data_1 = iData;
```

```matlab
120   Waveform_Sampling_Rate_1 = channel_bandwidth*sps*2*1e6;
121   %LEDbandwdith*sps*2(Nyquist)
122   Waveform_Signal_Format_1 = 'I';
123   % Create Q Waveform
124   Waveform_Name_2 = 'MyQ_Waveform';
125   Waveform_Data_2 = qData;
126   Waveform_Sampling_Rate_2 = channel_bandwidth*sps*2*1e6;
127   Waveform_Signal_Format_2 = 'Q';
128   % Save Files
129   save('OFDM_ABL_waveform_3686Mbps_AMBER.mat', '*_1', '*_2', '-
130   v7.3');
131   %% Taking data from Sampling_conversion .m file (i.e. oscilloscope)
132       rxSignal =T1;
133       rxSignal_pilot = T3;
134     specScope = dsp.SpectrumAnalyzer('NumInputPorts',2, ...
135       'SampleRate',awg_samplerate_MSps*1e6, ...
136       'PlotAsTwoSidedSpectrum',false, ...
137       'ShowLegend',true, ...
138       'ChannelNames',{'Tx','Rx'}, ...
139       'AxesScaling','Auto');
140   specScope(txFiltSignal_abl,rxSignal);
141   specTable = getSpectrumData(specScope);
142   writetable(specTable,'specScope.csv');
143   %% Receiving the signal, downsampling and filtering
144   rxFiltSignal = upfirdn(rxSignal,rrcFilter,1,sps);  % Downsample and
145   filter
146    rxFiltSignal = rxFiltSignal(filtlen + 1:end - filtlen); % Account
147   for delay
148    rxFiltSignal_pilot =
149   reshape(rxSignal_pilot,[length(pilot_signal_abl)/n_pilot_frames,
150   n_pilot_frames]);
151   rxFiltSignal_pilot = upfirdn(rxFiltSignal_pilot,rrcFilter,1,sps); %
152   Downsample and filter
153   rxFiltSignal_pilot = rxFiltSignal_pilot(filtlen + 1:end - filtlen,
154   :); % Account for delay
155   %% Removing cyclic prefix, convert to parallel then applying fft
156   rxFiltsignal_nocp=rxFiltSignal(cp+1:end);
157   rxFiltsignal_nocp1=reshape(rxFiltsignal_nocp,[subs,length(rxFiltsig
158   nal_nocp)/subs]);%S->P
159   fft_X=fft(rxFiltsignal_nocp1);
160   fft_X((subs/2+1),:)=[];
161   fft_X(1,:)=[];
162   fft_X=normalize(fft_X,2);
163   %pilot
164   rxFiltSignal_pilot_nocp = rxFiltSignal_pilot(cp+1:end,:);
165   rxFiltSignal_pilot_nocp1 =
166   reshape(rxFiltSignal_pilot_nocp,[subs,length(rxFiltSignal_pilot_noc
167   p)/subs,n_pilot_frames]);
168   fft_X_pilot=fft(rxFiltSignal_pilot_nocp1);
169   fft_X_pilot((subs/2+1),:,:) = [];
170   fft_X_pilot(1,:,:) = [];
171   fft_X_pilot=normalize(fft_X_pilot,2);
172   %% Channel Equalisation
173   X((subs/2+1),:)=[];
174   X(1,:)=[];
175   sum_pilot = sum(fft_X_pilot,3);
176   sum_transmitted = n_pilot_frames.*X;
177   H_channel_pilotest = sum_pilot./sum_transmitted;
178   equalised_signal_abl = fft_X./H_channel_pilotest;
179   fft_X_ber_pilot = transpose(equalised_signal_abl);
180   %% Demodulate the equalised QAM constellation and calculate the BER
```

```matlab
181    dataSymbolsOut4 = zeros(max(n),length(M));
182    for i=1:length(M)
183         if n(i) == 0
184             break
185         end
186    dataSymbolsOut4(1:max(n(i)),i) =
187    qamdemod(fft_X_ber_pilot(:,i),M(i),'OutputType','bit','UnitAverageP
188    ower',true);
189    end
190    % compare bits out to bits in to calculate bit error ratio (BER)
191    [no_errors,BER_after_eq_pilot_est] = biterr(dataSymbolsOut4,dataIn)
192     figure('Name','Unequalised Data','NumberTitle','off')
193    for i=subs/64:subs/64:subs_2 % plot Rx symbols per subcarrier
194    subplot(4,8,i/(subs/64))
195    plot(fft_X(i,:),'.');
196    title(['SC#: ',num2str(i), '    f: ', num2str((LED_SSB/subs_2)*i),
197    ' MHz']);
198    xlabel('In-phase');
199    ylabel('Quadrature');
200    xlim([-1.5 1.5])
201    ylim([-1.5 1.5])
202     hold on
203     plot(X(i,:),'r x','MarkerSize', 5,'linewidth', 3);
204    end
205    figure('Name','Pilot EQ method','NumberTitle','off')
206    for i=subs/64:subs/64:subs_2 % plot Rx symbols per subcarrier
207    subplot(4,8,i/(subs/64))
208    plot(equalised_signal_abl(i,:),'.', 'Color', '#e8cb0c');
209    title(['SC#: ',num2str(i), '    f: ', num2str((LED_SSB/subs_2)*i),
210    ' MHz']);
211    xlabel('In-phase');
212    ylabel('Quadrature');
213    xlim([-1.5 1.5])
214    ylim([-1.5 1.5])
215    % hold on
216    % plot(X(i,:),'r x','MarkerSize', 5,'linewidth', 3);
217    end
218    clear abl
219    clear abl_pilot
```

8.4 MATLAB code for OOK modulation

8.4.1 Program 1: PRBS sequence generation

```matlab
% -----------------------------------------------------------------
--------
% N = length of the PRBS sequence, N=2^k - 1, PBRS-k sequence
% M = number of samples per bit
% For a 8GS/s awg divide through by M for bit rate
% -----------------------------------------------------------------
--------
close all;
clear all;
% -----------------------------------------------------------------
--------
% DEFINE PRBS SEQUENCE AND PARAMETERS
% -----------------------------------------------------------------
--------
N = 1023; % lenght of the PRBS sequence (PBRS-7)
M = 8; % number of samples per bit (calculate bit rate for 8GS/s
awg)
Bit_rate_Mbps = 8000/M
Fs = 1;
uk = idinput(N,'prbs',[0 1],[-1 1]);

oversample = 4;   % Number of samples per symbol (oversampling
factor)
rolloff = 0.9;    % RRC filter rolloff
filtlen = 100;
EbNo = 15;
% ------------------------------------------------------------------
--------

% ------------------------------------------------------------------
--------
% GENERATE WAVEFORM
% ------------------------------------------------------------------
--------
for k=1:N
    if (uk(k) == -1)
        for i=1:M
        waveformTemp(k,i) = [-1];
        end
        waveform{k} = waveformTemp(k,:);
    elseif (uk(k) == 1)
        for i=1:M
        waveformTemp(k,i) = [1];
        end
        waveform{k} = waveformTemp(k,:);
    end
end
% -------------------------------------------------------------------
--------

% % -------------------------------------------------------------------
----------
% % CONVERT TO AWG COMPATIBLE FILE
% % -------------------------------------------------------------------
----------
PRBSwave = cell2mat(waveform);
baseWfm = PRBSwave;
baseMarkers = uint8(square(PRBSwave));
```

```matlab
59   Waveform_Name_1 = 'PBRS_1000Mbps';
60   Waveform_Data_1 = baseWfm; %already a double array
61   Waveform_M1_1 = baseMarkers; %already uint8 array
62   Waveform_M2_1 = baseMarkers;
63   save('PRBS_ 1000Mbps', '*_1', '-v7.3'); % MAT 7.3 Can save > 2GB
64   % ----------------------------------------------------------------
65   --------
66   % ----------------------------------------------------------------
67   --------
68   % PLOT WAVEFORM
69   % ----------------------------------------------------------------
70   --------
71   figure(1);
72   h = plot(PRBSwave,'k');
73   set (h, 'LineWidth', 2); % for a width of n
74   axis([0,length(PRBSwave),-1.5,1.5]);
75   title('Input waveform');
76   xlabel('Samples')
77   ylabel('Amplitude (a.u)')
78   %----------------------------------------------------------------
79   -------
```

8.4.2   Program 2: Eye diagram generation

```matlab
1    AWG_Fs = 8e9;                        % AWG sampling rate
2    OSC_Fs = 25e9;                       % oscilloscope sampling rate
3       x1000mbps = -x1000mbps;
4       x=turbo;
5    [P1,Q1] = rat(AWG_Fs/OSC_Fs);    % Rational fraction approximation
6    s1 = resample(x1000mbps,P1,Q1);        % Change sampling rate by
7    rational factor
8    M=8;
9    eyeObj2 = comm.EyeDiagram(...
10       'SampleRate', OSC_Fs, ...
11       'SamplesPerSymbol', M, ...
12       'YLimits',[-0.05 0.05], ...
13       'OversamplingMethod', 'Input Interpolation', ...
14       'DisplayMode', '2D color histogram');
15   eyeObj2(s1);
```